Critical Dynamics in Classical Antiferromagnets

Von der Fakultät Mathematik und Physik der Universität Stuttgart
zur Erlangung der Würde eines Doktors der Naturwissenschaften
(Dr. rer. nat.) genehmigte Abhandlung

vorgelegt von

Kuo Feng Tseng

aus Taiwan

Hauptberichter:	Prof. Dr. Bernhard Keimer
Mitberichter:	Prof. Dr. Gert Denninger
Tag der mündlichen Prüfung:	02. November 2016

Max-Planck-Institut für Festkörperforschung
Stuttgart 2016

Contents

Abbreviations

AFM	... Antiferromagnetic
ESR	... Electron spin resonance
HAFM	... Heisenberg antiferromagnet
HFM	... Heisenberg ferromagnet
HWHM	... Half-width-half-maximum
IAFM	... Ising antiferromagnet
NS	... Neutron scattering
NSE	... Neutron spin-echo scattering
NRSE	... Neutron resonance spin-echo scattering
NRSE-TAS	... Neutron resonance spin-echo triple-axis spectroscopy
NMR	... Nuclear magnetic resonance
PAC	... Perturbed angular correlations of γ – ray spectroscopy
TAS	... Triple-axis spectroscopy
μSR	... Muon spin relaxation

Zusammenfassung in deutscher Sprache

Kritische Dynamik in klassischen Antiferromagneten

Diese Arbeit beschreibt eine Studie der kritischen Dynamik der Antiferromagneten MnF_2 und Rb_2MnF_4 mit zwei- bzw. dreidimensionaler (2D, 3D) Kopplung der $S = 5/2$ Spins. Die Untersuchungen wurden mittels Neutronen-Spinecho-Spektroskopie mit hoher Energieauflösung ohne externes Magnetfeld durchgeführt. Beide Materialien sind Heisenberg-Antiferromagneten mit einer kleinen uniaxialen Anisotropie, die von der dipolaren Wechselwirkung verursacht wird und zu einem Übergang in der kritischen Dynamik nahe der Néel-Temperatur T_N führt. Die hohe Energieauflösung der Spin-Echo Technik ermöglichte die Bestimmung der kritischen Exponenten z für die longitudinalen und transversalen Komponenten der kritischen Fluktuationen. Für MnF_2 sind sowohl die Übergangstemperatur der Fluktuationen von 3D-Heisenberg- nach 3D Ising-Dynamik und die Exponenten z konsistent mit der Skalentheorie. Das Verhältnis der Amplituden der longitudinalen und transversalen Fluktuationen stimmt mit den theoretischen Vorhersagen überein. Rb_2MnF_4 zeigt bei hohen Temperaturen $T \gg T_N$ die erwartete Heisenberg-Dynamik, doch der kritische Exponent $z = 1.387(4)$ nahe bei T_N findet keine einfache theoretische Erklärung und resultiert wahrscheinlich von dipolaren Wechselwirkungen mit langer Reichweite.

Kritische Fluktuationen treten an kontinuierlichen Phasenübergängen auf. Sie wurden zuerst im frühen 19. Jahrhundert beim Verdampfen von flüssigem CO_2 beobachtet. Dichtefluktuationen bewirken verstärkte Lichtstreuung und trüben die ansonsten durchsichtige Flüssigkeit. Thomas Andrews beschrieb schon im Jahr 1869 den Zusammenhang der kritischen Trübung mit Phasenübergängen [1]. Die Untersuchung kritischer Fluktuationen ist auch heute noch ein ergiebiges Thema, wobei sich 20. Jahrhundert das Interesse auf magnetische Phasenübergänge verlagerte. Diese haben den Vorteil, dass die Parameter in weiten Bereich variabel sind: von ein- bis dreidimensionaler Wechselwirkung des Spins, mit Quantencharakter ($S = 1/2$) oder fast klassisch ($S = 5/2$).

Die Neutronenstreuung spielt eine zentrale Rolle bei der Untersuchung kritischer magnetischer Fluktuationen, da der Neutronenspin an die fluktuierenden magnetischen Momente koppelt. Dynamische Fluktuationen führen zu inelastischer Streuung der

Neutronen, die mit modernen Spektrometern analysiert wird. Die intensive Forschung wurde in mehreren Publikationen zusammengefasst: Ergebnisse der inelastischen Neutronenstreuung an kritischen magnetischen Fluktuationen in den Büchern von Als-Nielsen [2] und Collins [3], kritische Fluktuationen in Flüssigkeiten im Buch von Levelt-Sengers [4] und Ergebnisse von magnetischen Systemen mittels NMR im Übersichtsartikel von Hohenemser [5].

Die statischen (zeitlich gemittelten) Eigenschaften magnetischer Phasenübergange hängen nur von der Dimension der Kopplung des Spinsystems ab. In der Nähe des Phasenübergangs folgen die statischen Eigenschaften wie Magnetisierung, Suszeptibilität, spezifische Wärme und Korrelationslänge Potenzgesetzen der reduzierten Temperatur $t = T/T_{c,N} - 1$, mit kritischen Exponenten β, γ, α, und ν. Skalen-Gesetzte definieren die Relationen zwischen den kritischen Exponenten.

Die dynamischen Eigenschaften magnetischer Phasenübergänge wurden erstmals in der dynamischen Skalentheorie von Halperin und Hohenberg [6, 7] quantitativ beschrieben. Ein wesentliches Ergebnis besagt, dass die charakteristische Energiebreite Γ der Spinfluktuationen mit der magnetischen Korrelationslänge ξ skaliert, z ist der dynamische kritische Exponent:

$$\Gamma \sim \xi^{-z} \sim t^{z\nu}$$

Bei Annäherung an die kritische Temperatur ($t = 0$) divergiert die Korrelationslänge und Γ geht gegen Null, was als *kritische Abbremsung* der Spinfluktuationen bezeichnet wird. Für 3D Heisenberg-Ferromagneten (3D HFMs) wird $z = 2.5$ vohergesagt, für 3D Heisenberg-Antiferromagneten (3D HAFMs) $z = 1.5$. Zusätzliche langreichweitige Spin-Wechselwirkungen können die kritische Dynamik drastisch beeinflussen.

In MnF_2, einem der besten Modelle für 3D Ising-Antiferromagnetismus (3D IAFM), induzieren dipolare Spin-Spin Wechselwirkungen mit langer Reichweite eine kleine uniaxiale Anisotropie. Die gemessenen statischen kritischen Exponenten β, ν und γ folgen nahe der Néel Temperatur T_N wie erwartet 3D Ising Verhalten, aber der dynamische Exponent z liegt nahe bei 1.5, was der für 3D Heisenberg AFM vorhergesagten Skalierung entspricht. Eine überzeugende Erklärung für diese Diskrepanz wurde bisher nicht gefunden, wahrscheinlich spielt die begrenzte Energieauflösung der Dreiachsen-Spektrometer (TAS) eine wesentliche Rolle, da die sehr kleinen Energiebreiten Γ nahe T_N nicht gut aufgelöst werden. Im Fall des zweidimensionalen Heisenberg-Antiferromagneten (2D HAFM) Rb_2MnF_4 mit $S = 5/2$ sollte die uniaxiale Spin-Raum Asymmetrie bei Abkühlung Richtung T_N einen Übergang von Heisenberg nach Ising Verhalten bewirken. Hier sind Tests der dynamischen Skalentheorie mittels TAS wie bei MnF_2 schwierig bis unmöglich. Mit einem geeigneten Magnetfeld H an der Probe nahe am bikritischen Punkt im H-T Phasendiagramm sollte die Anisotropie nicht relevant sein. Neutronenstreuung zeigt an diesem Punkt $z = 1.35(2)$, das klar vom theoretisch

vorhergesagten $z = 1$ verschieden ist [8]. Eine Erklärung für diese Diskrepanz wurde bisher ebenfalls nicht gefunden.

Diese offenen Fragen und experimentellen Schwierigkeiten sollen in dieser Dissertation neu beleuchtet werden. Ziel waren neue Experimente an den Modellsystemen MnF_2 und Rb_2MnF_4 mittels Spin-Echo-Dreiachsen Spektroskopie (NRSE-TAS) mit Energieauflösung im Bereich $1\,\mu$eV. Die von der magnetischen Streuung induzierten Spinflip Prozesse der Neutronenspins führen zu komplizierten Oszillationen der Spin-Echo Signale. Um diese instrumentellen Effekte unabhängig von Näherungen zu beschreiben, führen wir eine neue Analysemethode basierend auf einer Ray-Tracing Simulation des Spektrometers ein. Diese Methode erlaubt die Trennung von longitudinalen und transversalen Komponenten der Spinfluktuationen auch dann, wenn beide Komponenten zum Strukturfaktor beitragen. Dies ist ein weiterer Vorteil der NRSE-TAS Methode.

Wir fassen nun zuerst die Ergebnisse für MnF_2 kurz zusammen. Fig. 0.1 zeigt die Temperaturabhängigkeit der longitudinalen Linienbreite ($\Gamma_\parallel$), der transversalen Linienbreite ($\Gamma_\perp$) und der relativen integrierten Intensität an $\boldsymbol{Q} = (300)$. Die Analyse der Spin-Echo Daten wurde mit der oben genannten neuen Technik durchgeführt. Wegen der Spin-Anisotropie zeigen nur die longitudinalen Fluktuationen kritisches Verhalten für $T \to T_N$, während die transversalen Linienbreiten kontinuierlich verlaufen. $T_N = 67.29\,$K wurde aus der maximalen Steigung der Intensität des magnetischen $\boldsymbol{Q} = (300)$ Bragg-Reflexes bestimmt. Die Daten für $\Gamma_\parallel(T)$ in Fig. 0.1 (a) weichen im grau schattierten Bereich bei $T = 69\,$K deutlich von einfachen Potenzgesetzen ab. Die blaue gepunktete Linie ist an die Daten im Bereich $T_N < T < 1.01\,T_N$ angepasst mit $z\nu = 1.25(2)$. Mit dem für 3D Ising Antiferromagneten (3D IAFM) vorhergesagten Exponenten $\nu_{\mathrm{3DIAFM}} = 0.6301$ erhalten wir $z = 1.98(3)$, das innerhalb des Fehlers dem für diese Universalitätsklasse vorhergesagten $z = 2$ entspricht [7]. Für $T > 1.04\,T_N$ enspricht die rote Kurve dem Exponenten $z\nu = 1.02(3)$. Mit dem theoretischen $\nu_{\mathrm{3D\,HAFM}}$ ergibt sich $z = 1.43(5)$, was nahe bei dem für 3D Heisenberg-Antiferromagneten (3D HAFM) erwarteten $z = 1.5$ liegt. Die Daten $\Gamma_\parallel(T)$ zeigen einen Übergang von 3D IAFM nahe T_N zu 3D HAFM Skalierung für $T > T_N$. Die relativen Amplituden (~ 3) aus diesem Fit sind in guter Übereinstimmung mit dem Wert 3.1, der von Riedel und Wegner berechnet wurde [10, 11]. Wir erhalten als Übergangstemperatur $T_x = 69.2(1)\,$K oder $t_x = 0.029(1)$ in guter Übereinstimmung mit der Vorhersage $t_x = 0.036$ von Pfeuty *et al.* [12].

Die Linienbreite $\Gamma_\perp(T)$ der transversalen Fluktuationen ist in Fig. 0.1 (b) zusammen mit TAS Daten aus der Literatur aufgeragen [13, 14]. Wir beobachten einen schnellen Anstieg von $\Gamma_\perp$ zwischen T_N und der unteren Grenze des Übergangsbereichs bei $1.01\,T_N$, wobei $\Gamma_\perp$ bei etwa $300\,\mu$eV in Sättigung geht. Berechnungen haben diesen Sättigungswert vorausgesagt, der einem Exponenten $z_\perp = 0$ entspricht [11, 15, 16].

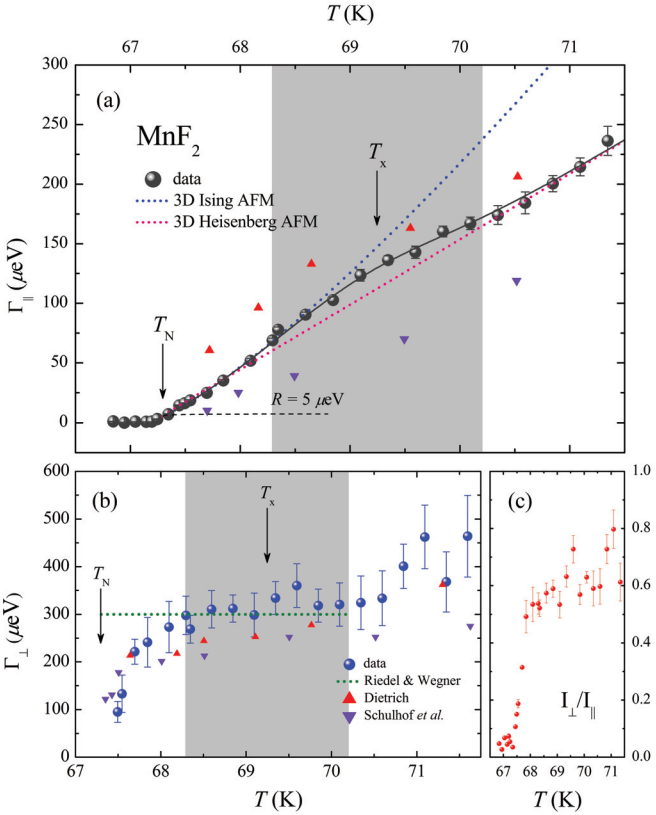

Fig. 0.1: Temperaturabhängigkeit in MnF_2 von (a) $\Gamma_\parallel$ und (b) $\Gamma_\perp$. (c) Verhältnis der integrierten Intensitäten. [9].

$\Gamma_\perp$ wächst oberhalb des Übergangsbereichs ($T > 1.04\,T_N$), so wie es für 3D HFAM Skalierung erwartet wird. Die Fehlerbalken werden bei hohen Temperaturen groß, da die Flügel der Lorentz-förmigen Linie durch die Transmissionsfunktion des TAS beschnitten werden. Daher erlaubt die Qualität der Daten hier keine Bestimmung des kritischen Exponenten und qualitative Bestätigung der 3D HAFM Skalierung von $\Gamma_\perp$ für $T \gg T_N$.

Fig. 0.1 (c) zeigt das Verhältnis der integrierten Intensitäten von longitudinalen und transversalen Fluktuationen. Nahe T_N dominieren wegen der uniaxialen Anisotropie

die longitudinalen Korrelationen die kritische Streuung. Mit wachsendem T steigt das Verhältnis der integrierten Intensitäten schnell an und geht gegen 1 für $T \gg T_N$, was dem Übergang des Systems in die 3D HFAM Skalierung entspricht.

Im Folgenden diskutieren wir die Ergebnisse für Rb_2MnF_4. Das Mermin-Wagner Theorem besagt, dass in 2D Heisenberg-Antiferromagneten keine Ordnung mit langer Reichweite für $T > 0\,\mathrm{K}$ auftritt. Die 3D antiferromagnetische Ordnung in Rb_2MnF_4 unterhalb $T_N = 38.4\,\mathrm{K}$ wird durch kleine Spin-Asymmetrie α_1 induziert. Fig. 0.2 (a) zeigt $\Gamma_\parallel(T)$, das nahe $T = 44\,\mathrm{K}$ die Steigung ändert. Wegen der dipolaren Anisotropie erwartet man einen Übergang des Verhaltens von 2D Ising Antiferromagnetismus (2D IAFM) für $T \sim T_N$ nach 2D HAFM für $T \gg T_N$. Solch ein Übergang in der longitudinalen Korrelationslänge wurde nahe $T_x = 1.2\,T_N$ von Lee *et al.* [17] beobachtet. Im Intervall $T_N < T < 1.16\,T_N$ ergibt unser Experiment den Exponenten $z\nu = 1.387(4)$. Mit dem theoretisch für 2D IAFM vorhergesagten $\nu_{\mathrm{2DIAFM}} = 1$ erhalten wir $z = 1.387(4)$, das sich signifikant vom erwarteten $z_{\mathrm{2D\,IAFM}}$ unterscheidet [18]. Das bedeutet, dass unsere Daten für $\Gamma_\parallel$ nahe T_N nicht konsistent mit 2D IAFM sind. Solch eine Abweichung von 2D IAFM Skalierung wurde für den statischen kritischen Exponenten β auch von Birgeneau *et al.* [19] beobachtet. Das aus der Magnetisierungkurve für $T < T_N$ bestimmte $\beta = 0.18$ unterscheidet sich deutlich vom erwarteten $\beta = 0.125$ [20]. Eine mögliche Ursache für dieses unerwartete Skalierungsverhalten von $\Gamma_\parallel$ für $T > 1.20\,T_N$ ist die dipolare Wechselwirkung, die auch wesentlich für das Magnonen-Gap im geordneten Zustand verantwortlich ist, und durch die lange Reichweite das universelle Skalierungsverhalten ändern kann. Ein Fit mit dem Ausdruck $\Gamma_\parallel(t) \propto \xi_{\mathrm{eff}}^{z_\parallel}$ ergibt $z_\parallel = 0.96(4)$ in Übereinstimmung mit der Vorhersage $z = 1$ für 2D HAFM [7]. Die Übergangstemperatur $T_x = 44.3(4)\,\mathrm{K}$ oder $t_x = 0.179$ ist etwas kleiner als der vorhergesagte Wert.

Die Linienbreite $\Gamma_\perp$ der transversalen Fluktuationen ist in Fig. 0.2 (b) aufgetragen. $\Gamma_\perp$ hat bei T_N einen Wert > 0, formt ein Plateau bei $200\,\mu\mathrm{eV}$ und wächst kontinuierlich für $T > T_x$. Unser Fit ergibt $z_\perp = 0.97(15)$ wie für 2D HAFM Skalierung erwartet. Dieses Ergebnis ist auch konsistent mit dem Verhältnis der Integrierten Intensitäten in Fig. 0.2 (c), das oberhalb T_x gegen 1 geht, wie für das identische Verhalten transversaler und longitudinaler Fluktuationen in 2D HAFM erwartet wird.

In Fig. 0.3 sind die wesentlichen Ergebnisse unserer Studie des dynamischen kritischen Verhaltens von zwei schwach anisotropen $S = 5/2$ Antiferromagenten mit zwei- und dreidimensionaler Spinkopplung zusammengefasst. Beide Verbindungen zeigen einen Übergang im Skalierungsverhalten, der aus der kleinen uniaxialen Anisotropie resultiert. Der dynamische kritische Exponent von MnF_2 ändert sich von $z_\parallel = 1.43(5)$ oder 3D HAFM Skalierung bei hohem T nach $z_\parallel = 1.98(3)$ oder 3D IAFM nahe T_N. Dieser Übergang tritt bei $T_x = 1.03\,T_N$ auf, was den Vorhersagen entspricht. Die transversale Linienbreiten $\Gamma_\perp$ sind konsistent mit dem vorhergesagten $z = 0$ nahe

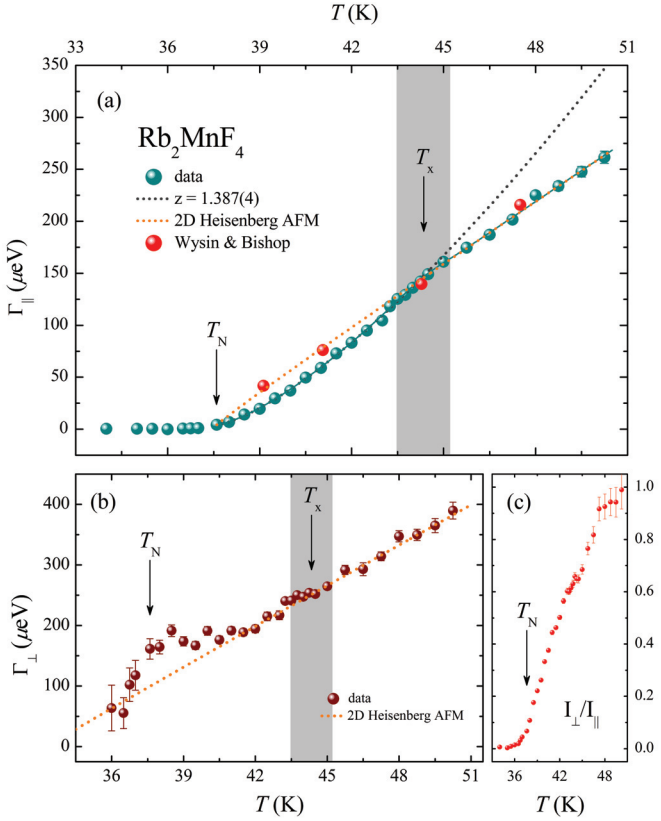

Fig. 0.2: Temperaturabhängigkeit in Rb_2MnF_4 von (a) $\Gamma_\parallel$ und (b) $\Gamma_\perp$. (c) Verhältnis der integrierten Intensitäten. [9].

T_x, aber sinken deutlich bei Abkühlung Richtung T_N. Der dynamische kritische Exponent $z_\parallel$ in Rb_2MnF_4 ändert sich an der Übergangstemperatur $T_x = 1.18\,T_N$ von $z_\parallel = 0.96(4)$ bei $T > T_x$, das entpricht 2DHAF Saklierung, nach $z_\parallel = 1.387(4)$ für $T_N < T < T_x$. Der letzte Wert entspricht nicht dem für das 2D Ising Modell erwarteten $z = 1.75$. Diese Skalierung resultiert wahrscheinlich von der langreichweitigen Natur der dipolaren Kräfte, die dynamischen Fluktuationen durch das Öffnen zusätzlicher Zer-fallskanäle beeinflussen, während die statischen Eigenschaften nicht beeinflusst werden. Die transversalen Fluktuationen zeigen konstante Linienbreiten mit $z_\perp = 0$ nahe T_N und sind identisch mit den longitudinalen Fluktuationen für hohe Tempera-

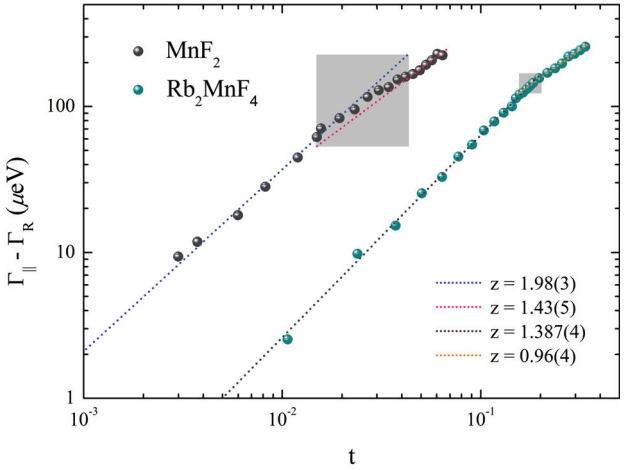

Fig. 0.3: Linienbreiten der longitudinalen kritischen Streuung in MnF_2 und Rb_2MnF_4. [9].

turen $T \gg T_N$, d.h. sie zeigen 2DHA Skalierung mit $z_\perp = 0.97(15)$.

Die hochauflösende Dreiachsen-Spinecho Technik hat in dieser Arbeit einen detaillierten Einblick in die kritische Dynamik von Antiferromagneten ermöglicht und zur Klärung vorheriger widersprüchlicher Ergebnisse beigetragen. Unsere Methode, die eine Trennung von longitudinalen und transversalen Fluktuationen erlaubt, kann direkt auf eine große Klasse von Fragen über kritische magnetische Fluktuationen angewendet werden. Der nächste Schritt wird die Durchführung einer ähnlichen Studie über quantenkritische Fluktuationen in $TlCuCl_3$ in der Nähe des quantenkritischen Punktes bei moderatem Druck ohne Magnetfeld sein. Erste Testexperimente mit neu entwickelten Gasdruckzellen wurden durchgeführt.

Abstract

Critical Dynamics in Classical Antiferromagnets

This thesis reports on a neutron spin-echo study of the critical dynamics in the $S = 5/2$ antiferromagnets MnF_2 and Rb_2MnF_4 with three-dimensional (3D) and two-dimensional (2D) spin systems, respectively, in zero external field. Both compounds are Heisenberg antiferromagnets with a small uniaxial anisotropy resulting from dipolar spin-spin interactions, which leads to a crossover in the critical dynamics close to the Néel temperature, T_N. By taking advantage of the μeV energy resolution of the spin-echo spectrometer, we have determined the dynamical critical exponents z for both longitudinal and transverse fluctuations. In MnF_2, both the characteristic temperature for crossover from 3D Heisenberg to 3D Ising behavior and the exponents z in both regimes are consistent with predictions from the dynamical scaling theory. The amplitude ratio of longitudinal and transverse fluctuations also agrees with predictions. In Rb_2MnF_4, the critical dynamics crosses over from the expected 2D Heisenberg behavior for $T \gg T_N$ to a scaling regime with exponent $z = 1.387(4)$, which has not been predicted by theory and may indicate the influence of long-range dipolar interactions.

This work establishes a basis for high-resolution studies of critical antiferromagnetic fluctuations by neutron spin-echo. The next step is the investigation of magnetic quantum criticality. First measurements were conducted on $TlCuCl_3$, which exhibits a quantum critical point under moderate pressure.

1 Introduction

Critical fluctuations occur close to continuous phase transitions. They were first observed in the early 19th century at the liquid-gas transition in CO_2. Density fluctuations induce enhanced scattering of light and lead to opalescence of the otherwise transparent system. Thomas Andrews in 1869 first pointed out the connection between critical opalescence and phase transitions [1]. The basic parameter for the description of critical fluctuations is the correlation length ξ, which sets an universal length scale and diverges at the phase transition. In the case of CO_2, ξ shows large values up to 1cm, which are visible by bare eye. The study of critical fluctuations remained an attractive subject during nearly 150 years. In the 20th century, researchers focused on magnetic phase transitions. These have the advantage to show a broad range of parameters: one- to three-dimensional interactions of the spins, with quantum ($S = 1/2$) or nearly classical ($S \gg 1/2$) character. Neutron scattering played an important role in the investigation of critical magnetic fluctuations, as the neutron spin couples to the fluctuating magnetic moments, and dynamic effects result in inelastic scattering of the neutrons, which is resolvable with modern spectrometers. The intense research has been summarized in several excellent reviews. The books by Als-Nielsen [2] and Collins [3], for example, have summarized results on magnetic fluctuations obtained by neutron scattering. Levelt-Sengers [4] has reviewed critical fluctuations in fluids, and the article by Hohenemser [5] has summarized studies of magnetic systems with a focus on NMR.

For magnetic phase transitions, the static (time-averaged) properties depend only on the lattice and spin dimensionality in systems with short-range interactions, but not on the microscopic Hamiltonian. This is the so-called universality of the phase transition. In approaching the critical temperature from above and below, the static properties, such as magnetization, susceptibility, specific heat, and correlation length, become singular and can be described by power laws, of the reduced temperature $t \equiv T/T_{c,N} - 1$ with critical exponents β, γ, α, and ν [see Table 2.1]. The relations among these exponents are governed by the so-called scaling laws.

The dynamic properties of magnetic phase transitions were first quantitatively described by the dynamic critical hypothesis proposed by Halperin and Hohenberg [6, 7]. One basic result is that the characteristic energy width Γ of spin fluctuations scales with the static magnetic correlation length ξ,

$$\Gamma \sim \xi^{-z} \sim t^{z\nu} \tag{1.1}$$

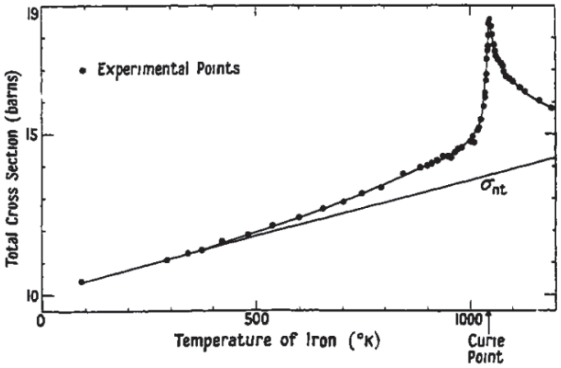

Fig. 1.1: The first neutron scattering on critical fluctuations of Fe: the total cross section *vs.* temperature. The nuclear cross section $\sigma_{\rm nt}$ shows a weak and featureless variation with temperature. From [21].

with z the dynamical critical exponent. Approaching the critical temperature ($t = 0$), the correlation length diverges and Γ goes to zero, corresponding to the so-called critical slowing down of the spin fluctuations. z can be experimentally verified by measuring Γ as a function of temperature or momentum transfer. The dynamic scaling depends both on the universality class, and on conservation laws of a system. This leads to different z for a given universality class if the conservation law that applies to the systems are different. For example, $z = 2.5$ and $z = 1.5$ are predicted for the three-dimensional Heisenberg ferromagnets (3D HFMs) and antiferromagnets (3D HAFMs), respectively. In addition, the presence of non-conserving forces arising from the long-range spin interactions can drastically affect the critical dynamics.

To investigate the magnetic critical phenomena, neutron scattering is a valuable tool for probing the order parameter and spin fluctuations of a system in the vicinity of critical point. The triple-axis spectrometer (TAS) allows direct measurement of the dynamic structure factor $S(\boldsymbol{Q}, \omega)$ in momentum-energy ($\boldsymbol{Q}$-ω) space. Other macroscopic tools, such as specific heat measurement and nuclear techniques, can only probe the averaged properties of spin fluctuation in the long-wavelength $\boldsymbol{Q} = 0$ limit. Indeed, the results of neutron scattering experiments played a key role in understanding critical phenomena. Historically, the first neutron scattering experiments on the critical fluctuations can be traced back to the 1950's. Latham and Cassels [22], and later Squires [21] found that the total scattering cross section of various ferromagnets increases at their respective Curie temperatures $T_{\rm c}$, signaling the onset of long-range magnetic orders of the systems. Fig. 1.1 shows the temperature dependent total cross section of Fe,

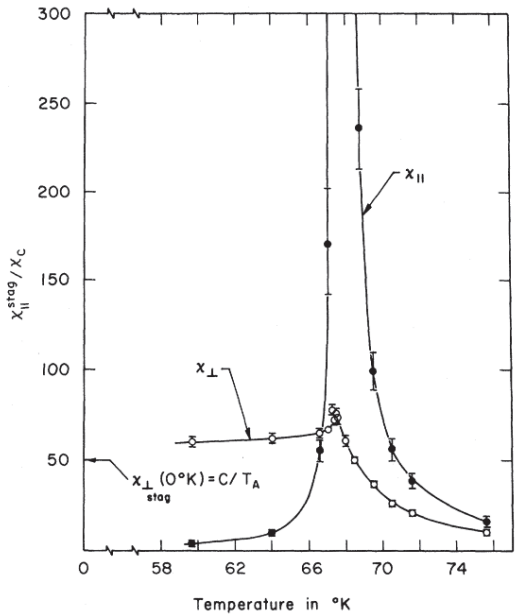

Fig. 1.2: The temperature dependence on longitudinal ($\parallel$) and transverse ($\perp$) susceptibility χ of MnF_2. Owing to the uniaxial anisotropy, only $\chi_\parallel$ diverges at $T_N = 67.3$ K. From [13].

together with the total nuclear contribution σ_{nt}. A sharp peak at T_c indicates the onset of ferromagnetic order. Als-Nielsen's and Dietrich's seminal work on β-brass in 1967 [23, 24, 25] found three static critical exponents $\beta = 0.305(5)$, $\nu = 0.65(2)$, and $\gamma = 1.25(2)$. These results are clearly different from the mean field predictions [26] but in good agreement with the prediction by series expansions using renormalization group theory [see Table 2.2]. Since then, neutron scattering studies on critical fluctuations of various materials in different lattice and spin dimensionality have made large progress.

The 3D model systems

In 3D HFMs, static properties of the model systems such as Ni, Fe, and EuO agree well with the prediction of the 3D Heisenberg model, while dynamic properties are less understood due to crossover effects resulting from dipolar or equivalent long-

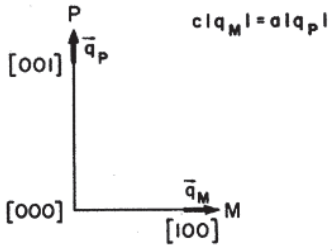

Fig. 1.3: The experimental strategies for separating the longitudinal and transverse spin fluctuations in the weakly anisotropic MnF_2. Along the $[100]$ direction, the *pure* transverse fluctuations contribute to the scattering, while along the $[001]$ direction, a mixture of the longitudinal and transverse parts contributes. From [13].

range interactions [27]. Among 3D HAFMs, $RbMnF_3$ is one of the best experimental realizations for both static and dynamic properties of critical phenomena: the static properties [28] follow the 3D Heisenberg model; and the dynamical critical exponent $z = 1.43(4)$ [29] is in good agreement with the dynamical scaling theory which predicts $z = 1.5$ [7]. Among the three-dimensional Ising antiferromagnets (3D IAFMs), FeF_2 and MnF_2 are the best realizations from theoretical and experimental aspects. Below the Néel temperature T_N, the uniaxial anisotropy of both leads to the Ising spin arrangement along the crystalline c axis. In strongly anisotropic FeF_2, the static and dynamic behavior ideally fits the 3D IAFM scaling. In MnF_2, where dipolar spin-spin interactions induce a small uniaxial anisotropy, the measured static critical exponents β, ν, and γ follow 3D Ising behavior [13, 30], as expected close to T_N, but the dynamic exponent z obtained from neutron scattering is close to the value 1.5 predicted for the 3D HAFM scaling [13]. In addition, $z = 1.75(5)$ [30] and $z = 2.3(3)$ [31] were deduced from the nuclear techniques in MnF_2. The origin of these discrepancies in z has not yet been conclusively resolved. They are probably caused by the limited energy resolution of TAS [13], which precludes inelastic scattering measurements sufficiently close to T_N. Another reason is the data treatment used in conventional TAS and nuclear techniques in discriminating the longitudinal and transverse spin fluctuations especially for anisotropic materials.

Regarding the critical phenomena of 3D IAFM, only the longitudinal fluctuations along the uniaxial spin anisotropy become critical, while the transverse components of spin fluctuations are suppressed by the anisotropy and thus are non-critical. In previous TAS studies on MnF_2, the two transverse components of the spin fluctuations were assumed to be identical [13, 14]. Fig. 1.2 shows the experimental results of the longitudinal and transverse staggered susceptibilities, $\chi_\parallel$ and $\chi_\perp$, of MnF_2 as a function of temperature [13]. $\chi_\parallel$ diverges at T_N whereas $\chi_\perp$ remains finite in the critical region. The crystals were aligned in the $(H0L)$ scattering plane as depicted in Fig. 1.3. Note that only the spin fluctuations that are perpendicular to the scattering vector $\boldsymbol{Q}$ make the contribution to the neutron scattering cross section. Hence, measurements along the $[001]$ direction signal the *pure* transverse spin fluctuations since the longitudinal

fluctuations are parallel to $\boldsymbol{Q}$. The scattering function for this *pure* transverse mode S_{P} can be expressed as

$$S_{\mathrm{P}}(q,\omega) \propto \frac{A_{\mathrm{P}}}{\kappa_{\perp}^2+q^2}\,\frac{1}{2}\Big[\frac{\Gamma_{\perp}}{\Gamma_{\perp}^2+(\omega-\omega_0)^2}+\frac{\Gamma_{\perp}}{\Gamma_{\perp}^2+(\omega+\omega_0)^2}\Big]. \tag{1.2}$$

On the other hand, measurements along the [100] direction consist of mixed contributions from the longitudinal and transverse spin fluctuations. The corresponding *mixed* scattering function S_{M} gives

$$\begin{aligned} S_{\mathrm{M}}(q,\omega) \propto{}& \frac{A_{\mathrm{M}}}{\kappa_{\parallel}^2+q^2}\,\frac{\Gamma_{\parallel}}{\Gamma_{\parallel}^2+\omega^2} \\ &+\lambda\,\frac{A_{\mathrm{M}}}{\kappa_{\perp}^2+q^2}\,\frac{1}{2}\Big[\frac{\Gamma_{\perp}}{\Gamma_{\perp}^2+(\omega-\omega_0)^2}+\frac{\Gamma_{\perp}}{\Gamma_{\perp}^2+(\omega+\omega_0)^2}\Big]. \end{aligned} \tag{1.3}$$

In the above two expressions, q denotes the amplitude of a reduced wave vector from the magnetic zone center and ω_0 is the magnon energy gap of the transverse components below T_{N}. A_{P} and A_{M} are the amplitudes of the scattering functions and λ describes the relative weight. In both experiments along the [001] and [100] directions, the dynamic property of the longitudinal spin fluctuations, the energy linewidth $\Gamma_{\parallel}$, can be extracted by subtracting the *pure* transverse component from the *mixed* scattering function.

The 2D model systems

After Onsager's exact solution on the static properties of two-dimensional Ising antiferromagnets (2D IAFMs), the K_2NiF_4-type compounds, such as K_2CoF_4 and K_2MnF_4, were identified as good realizations of the 2D spin systems [32, 33]. Among them, the dynamic critical exponent follows the conventional value $z = 1.75$ [34], independent of the spin value S. In the magnetically ordered state, the systems usually cross from 2D IAFM scaling near T_{N} to 3D IAFM scaling well below T_{N}. This leads to a changeover in the exponent β from the sublattice magnetization.

Following the discovery of high-temperature superconductivity in doped antiferromagnets, the spin dynamics of 2D antiferromagnets has received considerable attention in recent years. Since the spin systems of the parent compounds of the copper- and iron-based superconductors are nearly isotropic [35, 36, 37], the spin excitations and critical dynamics of Heisenberg antiferromagnets have been widely studied by inelastic neutron scattering [38, 39]. The undoped parent compounds of the cuprate superconductors, such as La_2CuO_4, are excellent models for the two-dimensional Heisenberg antiferromagnets (2D HAFMs) with $S = 1/2$. The temperature dependent magnetic correlation length ξ measured by neutron scattering is well described by theoretical work on the 2D HAFMs, not only for $S = 1/2$ compounds La_2CuO_4 and

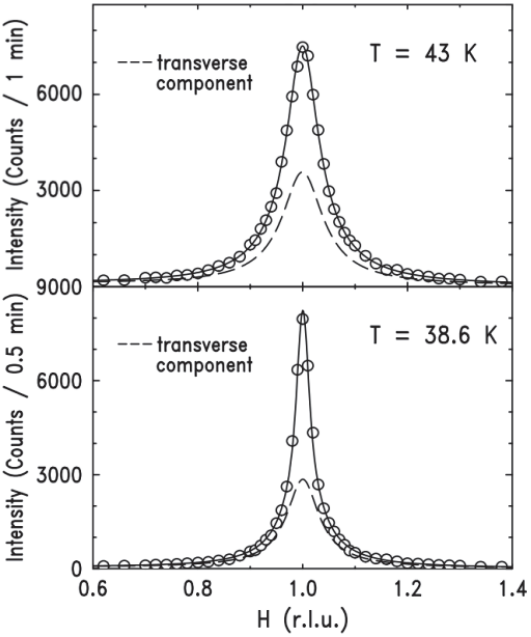

Fig. 1.4: Two energy-integrating scans on Rb_2MnF_4 along the [H/2 H/2 L] direction at $T = 43$ and 38.6 K with $T_N = 38.4$ K. The dashed lines are the transverse component of the magnetic scattering. From [17].

$Sr_2CuO_2Cl_2$ [35, 36, 37, 40], but also for related $S = 1$ K_2NiF_4 [38] and La_2NiO_4 [39] compounds and $S = 5/2$ Rb_2MnF_4 [17, 41]. The static properties of the 2D HAFM in the paramagnetic state generally agree with scaling relations predicted by the theories in the classical [42, 43] or quantum limit [44, 45, 46].

Measurements on the spin dynamics in the paramagnetic state of $S = 1/2$ $Sr_2CuO_2Cl_2$ and $Sr_2Cu_3O_4Cl_2$ systems are in good agreement with the exponent $z = 1$ predicted for the 2D HAFM [40]. For the quasi-2D $S = 5/2$ compound Rb_2MnF_4, on the other hand, the uniaxial spin-space anisotropy is expected to generate a crossover from 2D HAFM to 2D IAFM behavior upon cooling towards T_N, which precludes experimental tests of the dynamical scaling by neutron scattering, as in the case of MnF_2. Lee *et al.* [17] performed a two-axis neutron scattering experiment under zero magnetic field and utilized an analysis strategy to separate the longitudinal and transverse spin fluctuations. They

assumed the scattering function

$$S(q_{2D}) = \sin^2\phi \frac{S_{\parallel}(0)}{1 + q_{2D}^2/\kappa_{\parallel}^2} + (1 + \cos^2\phi) \frac{S_{\perp}(0)}{1 + q_{2D}^2/\kappa_{\perp}^2}, \tag{1.4}$$

where q_{2D} is a measure of wave vector from the magnetic Bragg point in the 2D sheets. $S_{\parallel,\perp}$ are the static scattering amplitude for longitudinal and transverse correlations, respectively. ϕ is defined according to the geometric configuration of the crystal mounting, which is subtended by a scattering wave vector $\boldsymbol{Q}$ and the c axis. Fig. 1.4 shows the analysis results of Eq. (1.4) for data at T = 43, and 38.6 K. By deducing data from the longitudinal correlation, they found $\nu = 1.0(1)$ at the temperatures within 1.2 T_N, in good agreement with the 2D IAFM scaling. Later, Leheny *et al.* [41] and Christianson *et al.* [8] performed neutron scattering experiments in a magnetic field H close to the bicritical point in the H-T phase diagram of Rb_2MnF_4, such that the spin anisotropy is expected to become irrelevant. The static properties are well described by the 2D HAFM theory in the classical limit [42, 43]. However, the dynamic properties yielded a value of $z = 1.35(2)$, clearly different from the theoretically predicted $z = 1$ for the 2D HAFM scaling [8]. The origin of this unexpected exponent has thus far remained unresolved.

Among the aforementioned model systems in 2D and 3D, experimental results of the static properties are in reasonable agreement with the theoretical predictions, independently of whether the spins are in the classical or quantum limit. They confirm the universality and scaling hypothesis of magnetic critical phenomena. However, much less information is available on the critical dynamics of the model systems. Several discrepancies were observed in dynamic scaling behavior, especially for systems with the admixture of anisotropy field arising from the long-range dipole-dipole interactions. MnF_2 and Rb_2MnF_4 are in this special case: they are a well-suited pair of classical antiferromagnets that are structurally and chemically closely similar and host 3D and 2D spin systems, respectively. So far, the long-standing puzzles for the critical dynamics of these materials with small spin anisotropy have not been experimentally articulated.

For conventional neutron scattering experiments, the following technical difficulties contributed to these discrepancies.

- One of the reasons for these discrepancies is the limited energy or momentum resolution of the neutron spectrometers used in previous times. For weakly anisotropic antiferromagnets, a small anisotropy causes uniaxial spin alignment along the c axis below T_N. At temperatures close to T_N, the magnetic correlation length (the inverse of the momentum-width) and the magnetic lifetime (the inverse of the energy linewidth) of the spin fluctuations become infinity. Experimentally, these facts make it difficult to resolve the much narrower widths in the momentum and energy scans with conventional neutron spectrometer. Typically,

the momentum and energy resolutions for a triple axis spectrometer at a thermal neutron source are around $0.01\,\text{Å}^{-1}$ and 1 meV, respectively. The limited momentum and energy resolution restricts experiments to approach the asymptotic critical region, which is more pronounced if the system is weakly anisotropic like MnF_2 and Rb_2MnF_4. This corresponds to a small crossover wave vector or crossover temperature, separating the *anisotropic* and *isotropic* critical regions of a system.

- The second reason is the data treatment to distinguish different components of the spin fluctuations. As illustrated in Eq. (1.2) to (1.4), the transverse (non-critical) component of the scattering cross section arising from the spin-wave scattering is subtracted by incorporating assumptions based on the scattering geometry and symmetry of the crystal. Although these strategies could model the data reasonably well, information of the relative intensities of the longitudinal and transverse components is missing. A clear separation of both components would offer a direct verification for applicability of these data treatments, since the integrated intensity of the longitudinal component dominates the scattering cross section as $T \to T_N$.

Motivated by these open questions in dynamic critical scaling and experimental difficulties, we have re-investigated the critical dynamics of the model compounds MnF_2 and Rb_2MnF_4 by means of the neutron spin-echo (NSE) triple-axis spectroscopy technique with energy resolution in the μeV range. A related NSE technique was first used by Mezei to study the critical dynamics of poly-crystalline iron [47, 48] and later optimized for the measurement of linewidths of quasi-elastic excitations at small momentum transfer $\boldsymbol{Q}$ [49]. For the present study at larger $\boldsymbol{Q}$, we took advantage of a modified type of NSE based on radio-frequency spin flippers incorporated in a TAS spectrometer (termed neutron resonant spin-echo, NRSE) [50, 51]. In this setup, the TAS provides good momentum resolution and helps suppress the background, but offers a comparatively coarse energy resolution, while the spin-echo device enhances the energy resolution by about two orders of magnitude.

For magnetic neutron scattering, it has thus far proven difficult to find a scattering vector $\boldsymbol{Q}$ where only one of the two components of the scattering function has a nonzero cross section. With the advantage of the NRSE setup, we are able to *echo* the desired longitudinal or transverse spin fluctuations along the corresponding $\boldsymbol{Q}$-space by selecting an appropriate magnetic field configuration on the spectrometer arms. However, the neutron spin-flip processes related to the magnetic scattering by spin excitations lead to complicated spin-echo signals, which makes the experimental data analysis difficult to deal with. To describe these effects, we introduce an analysis technique based on a neutron ray-tracing simulation of the spectrometer. In this way, we are able to discriminate between longitudinal and transverse fluctuations at positions in $\boldsymbol{Q}$-space where both fluctuation components contribute to the scattering cross section. This is

an additional distinct advantage of the NRSE-TAS setup. In this way, we were able to obtain new insight into the dynamical critical exponents and crossover temperatures in classical 3D and 2D antiferromagnets.

2 Critical phenomena in magnetic systems

2.1 Magnetic phase transitions and related critical exponents

Critical fluctuations at second order phase transition have been extensively studied for more than 100 years, from the liquid-gas transition in CO_2 [1] to quantum phase transitions that appear at $T = 0\,\mathrm{K}$ [52]. A second order phase transition shows a discontinuity in the second derivative of the Gibbs free energy at the critical point.

Magnetic model systems play an important role in understanding magnetic critical phenomena. An ideal model system possesses relatively simple exchange interactions between the magnetic ions, and the magnetic moments are not coupled to the lattice. In the high-temperature paramagnetic phase, the moments are randomly disordered and form a well-defined magnetic structure as the temperature is cooled below the critical temperature $T_{\mathrm{C,N}}$ for ferromagnetism and antiferromagnetism, respectively. The magnetically ordered and disordered phases of a system are thus separated by $T_{\mathrm{C,N}}$.

The key features of magnetic phase transition are [3]:

- There is a broken symmetry at the critical point. In the magnetic critical phenomena, this symmetry is represented by the time-averaged order parameter M of a system, which tends to zero in the high-temperature phase and is non-zero below the critical point. Indeed, each physical quantity following the above rule can be referred to as M for all phase transitions. In ferro- and antiferromagnetism, the order parameters are the magnetization and sublattice magnetization, respectively. Fig. 2.1 shows a typical example for the magnetic critical scattering in a prototype antiferromagnet MnF_2 at $\boldsymbol{Q} = \boldsymbol{G} + \boldsymbol{q}$ [14]. The dashed curve represents the data collected at the pure magnetic Bragg point with $q = 0$, showing the intensity of the antiferromagnetic Bragg peak ($\propto M^2$). With small deviations from the magnetic zone center, the solid curves signal the pure contribution from the magnetic critical scattering, with the peak positions located at $T = T_{\mathrm{N}}$.

- The magnetic correlation length ξ tends to infinity, both by approaching $T_{\mathrm{C,N}}$ from above or below. From a microscopic point of view, this divergent behavior

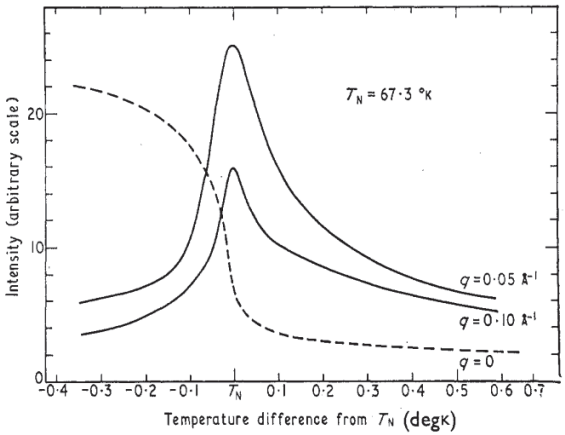

Fig. 2.1: Intensities of neutron critical scattering in MnF_2 (with $T_N = 67.3\,K$) at and in the vicinity of the magnetic Bragg reflection $\boldsymbol{G} = (100)$. From [14].

illustrates that the disordered spins or spin clusters become correlated over long distances compared to spin-spin interaction distances as the critical temperature is approached.

- The lifetime of spin fluctuations of a system tends to infinity as the critical point is approached. This dynamic (time-dependent) property is the so-called critical slowing down, which is the main subject of this thesis.

For the description of critical phenomena, the so-called static and dynamic properties are treated separately. The static properties are described by a time-averaged correlation function, which is determined by the so-called universality classes. The latter only depends on the spin and lattice dimensionality of the system and is independent of the local interactions. For the description of the dynamic properties, both the universality class and the conservation laws have to be taken into account. For example, in ferromagnets the order parameter commutes with the total energy, which is not the case in antiferromagnets. This leads to different dynamic critical exponents in ferro- and antiferromagnetism with the same universality class.

2.1.1 Static critical phenomena

The static (time-averaged) properties of magnetic phase transition can be described by the Gibbs free energy $G(T,H)$ of a system. By definition, the first and second derivative of G lead to static variables, including the order parameter M, the specific heat C_H at a constant magnetic field, and the isothermal susceptibility χ_T [3, 5].

$$M = -(\partial G/\partial H)_T, \quad C_H = -T(\partial^2 G/\partial T^2)_H, \quad \chi_T = -(\partial^2 G/\partial H^2)_T. \tag{2.1}$$

The correlation length ξ, which describes the size of regions of correlated spins, is obtained from the equal-time correlation function

$$C^{\alpha\beta}(\boldsymbol{r},\xi) = |r|^{-1} e^{-|r|/\xi}. \tag{2.2}$$

By taking the Fourier transform of $C^{\alpha\beta}(\boldsymbol{r},\xi)$, it gives

$$\hat{C}(\boldsymbol{q},\kappa) = S(\boldsymbol{q},\kappa) \simeq S(0,\kappa)[1 + (q/\kappa)^2]. \tag{2.3}$$

$S(\boldsymbol{q},\kappa)$ is proportional to the cross section for neutron scattering [2]. The reduced momentum transfer is $\boldsymbol{q} = \boldsymbol{Q} - \boldsymbol{G}$, where $\boldsymbol{Q}$ is the momentum transfer and $\boldsymbol{G}$ is a magnetic Bragg point. The inverse correlation length, $\kappa = \xi^{-1}$, is the characteristic width of $S(\boldsymbol{q},\kappa)$ with respect to q. In accordance with the fluctuation-dissipation theorem,

$$S(\boldsymbol{q},\kappa) \propto \chi(\boldsymbol{q},\kappa), \tag{2.4}$$

with $\chi(\boldsymbol{q},\kappa)$ the q-dependent susceptibility. In practice, neutron scattering provides a direct measure of $\chi(\boldsymbol{q},\kappa)$.

Upon approaching the critical point, all the static variables diverge and their singular behavior is best described in power law dependencies as a function of the reduced temperature $t \equiv |(T - T_{\mathrm{C,N}})|/T_{\mathrm{C,N}}$. The static critical exponents α, β, γ, ... can be obtained from different thermodynamic properties. Table 2.1 shows the definition of

Exponents	Properties	Definition	Conditions
β	Magnetization, M	$M \propto \lvert t\rvert^{\beta}$	$H = 0$
δ	Magnetization, M	$M \propto H^{1/\delta}$	$t = 0$
γ	Susceptibility, χ	$\chi \propto \lvert t\rvert^{-\gamma}$	$H = 0$
α	Specific heat, C_H	$C_H \propto \lvert t\rvert^{-\alpha}$	$H = 0$
ν	Correlation length, ξ	$\xi \propto \lvert t\rvert^{-\nu}$	$H = 0$
η	Correlation function, S	$S(q,\kappa) \propto q^{-2+\eta}$	$H = 0$

Table 2.1: Definition of the static (time-averaged) critical exponents.

model	mean field	Ising	Ising	Heisenberg
n	any	1	1	3
d	any	2	3	3
γ	1	1.75	1.2372(5)	1.3960(9)
ν	0.5	1	0.6301(4)	0.7112(5)
α	–	0	0.110(1)	-0.1336(15)
β	0.5	0.125	0.3265(3)	0.3689(3)
δ	3	15	4.789(2)	4.783(3)
η	0	0.25	0.0364(5)	0.0375(5)
Refs.	[26]	[20]	[53]	[54]

Table 2.2: Static critical exponents calculated for various spin (n) and lattice (d) dimensionality. The dash indicates the corresponding quantity doesn't follow a power law in the critical region.

various static critical exponents.

The Weiss molecular mean field theory of phase transition, introduced by Weiss in 1907, is the simplest one for magnetic systems [26]. It gives a general expression of the order parameter M below the critical temperature and the corresponding critical exponent $\beta = 0.5$. However, this prediction is insufficient to describe real magnetic systems since it neglects the effects of the spin fluctuations, which are crucial to magnetic phase transitions. Nonetheless, the mean field theory acts as the starting point in the development of theories of phase transitions. Later in 1944, Onsager [20] solved the 2D Ising model exactly and the resulting critical exponents are different from the mean field results [see Table 2.2]. However, no experimental data from layered magnetic systems were available to verify these predictions at that time.

More recently, Wilson applied the renormalization group theory (RGT) to the problems concerning continuous phase transitions [55, 56]. The RGT makes it possible to calculate the values of critical exponents more precisely. With the advantage of new computing techniques using RGT, precise results of the calculable exponents have been obtained. Table 2.2 shows the static critical exponents in various universality classes. It is clear that the static critical exponents within a certain class are universal, and they do not depend on the microscopic details of magnetic interactions. Real systems with identical spin and lattice dimensionality but with different exchange couplings share the same critical exponents.

In the so-called scaling approach proposed by Kadanoff *et al.* [57], the temperature dependent static correlation function $S(\boldsymbol{q}, \kappa)$ can be expressed as a product of q or κ

and a homogeneous scaling function g in q/κ

$$S(\boldsymbol{q},\kappa) = \kappa^{-2+\eta} g(q/\kappa), \tag{2.5}$$

$$S(\boldsymbol{q},\kappa) = q^{-2+\eta} g'(q/\kappa), \tag{2.6}$$

where the Fisher exponent η measures the deviation of the exponents in q and κ of Eq. (2.5) and (2.6) from −2 [58]. Experimentally, η can be determined by measuring the deviation of $\chi(q,T)$ from the simple Ornstein-Zernike theory [59] close to the critical point:

$$\chi(q,T) \propto \Big(\frac{1}{\kappa^2 + q^2}\Big)^{1-\eta/2}. \tag{2.7}$$

In addition to the universality of second-order phase transitions, critical exponents obey the so-called scaling laws defining the relation between different exponents. An example of deriving a scaling law is as follows. By taking the properties of Eq. (2.5) and the definition of the inverse correlation length $\kappa \sim t^{\nu}$, it gives

$$\lim_{q\to 0} S(q,\kappa) \sim \kappa^{-2+\eta} \sim t^{\nu(-2+\eta)}. \tag{2.8}$$

According to Eq. (2.4) and the definition of the magnetic susceptibility $\chi \sim t^{-\gamma}$, we obtain

$$\lim_{q\to 0} S(q,\kappa) \sim \chi(0,\kappa) \sim t^{-\gamma}. \tag{2.9}$$

From Eq. (2.8) and (2.9), the exponents of t yield a static scaling law

$$\nu(2-\eta) = \gamma. \tag{2.10}$$

In addition to Eq. (2.10), the rest of the static scaling laws are as follows.

$$\alpha + 2\beta + \gamma = 2 \tag{2.11}$$

$$\alpha + \beta(\delta + 1) = 2 \tag{2.12}$$

$$\gamma(\delta + 1) = (2-\alpha)(\delta - 1) \tag{2.13}$$

$$\beta = \nu(d - 2 + \eta)/2 \tag{2.14}$$

$$\delta = (d + 2 - \eta)/(d - 2 + \eta) \tag{2.15}$$

It is of practical importance for experimentalists to check the universality predictions by measuring at least three of the static critical exponents. The static critical exponents and the scaling laws in various universality classes have been confirmed. Table 2.3 illustrates the static critical exponents α, β, and γ for three-dimensional isotropic and anisotropic (Ising) model systems. These values are in overall good agreement with the

System	α	β	γ	$\alpha + 2\beta + \gamma$
Ni (FM)	−0.091(2) [60]	0.385(5) [61]	1.31(1) [62]	1.989(14)
Fe (FM)	−0.103(11) [60]	0.367(5) [63]	1.33(5) [64]	1.96(5)
EuO (FM)	−0.026(5) [65]	0.370(6) [66]	1.30(2) [66]	2.014(24)
FeF_2 (AFM)	0.111(7) [67]	0.325(7) [68]	1.25(2) [69]	2.011(19)
MnF_2 (AFM)	0.091(5) [67]	0.333(3) [30]	1.27(2) [13]	2.027(22)

Table 2.3: Experimental verification of the scaling law of $\alpha + 2\beta + \gamma = 2$ in three-dimensional ferromagnets (FMs) and antiferromagnets (AFMs).

theories for the given universality and their scaling relation is governed by the universal scaling law.

In summary, the current understanding of static critical phenomena has made tremendous progress after more than 100 years of intensive studies.

2.1.2 Dynamic critical phenomena

For the description of the dynamic properties of critical phenomena, frequency- or time-dependent correlations are introduced in addition to the (static) time-averaged spin-spin correlation function $\hat{C}$ [3] [see Eq. (2.3)],

$$\hat{C}(\boldsymbol{q}, t, \omega) = \hbar\beta\omega_c^{-1}\hat{C}(\boldsymbol{q}, t)F(\boldsymbol{q}, t, \omega/\omega_c). \tag{2.16}$$

The spectral weight function F in the dynamic part of Eq. (2.16) is normalized such that

$$\int_{-\infty}^{\infty} F(\boldsymbol{q}, t, \omega)d\omega = 1, \tag{2.17}$$

and the characteristic frequency ω_c is defined by

$$\int_{-\omega_c}^{\omega_c} F(\boldsymbol{q}, t, \omega)d\omega = \frac{1}{2}. \tag{2.18}$$

If $\hat{C}(\boldsymbol{q}, t, \omega)$ is a Lorentzian, then the characteristic frequency ω_c is the half-width-half-maximum (HWHM) Γ of the frequency spectrum. The dynamic scaling hypothesis [6, 7] requires that $\omega_c(q)$ is a homogeneous function of the wave vector $\boldsymbol{q}$ and the inverse magnetic correlation length $\kappa = \xi^{-1} \sim t^{\nu}$. The related scaling relations are

$$\omega_c(q, \kappa) = \kappa^z\Omega(q/\kappa), \tag{2.19}$$

$$\omega_c(q, \kappa) = q^z\Omega'(q/\kappa). \tag{2.20}$$

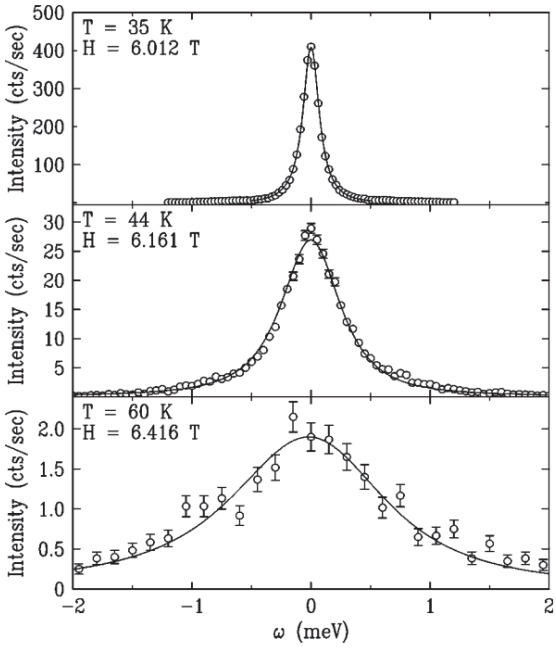

Fig. 2.2: Experimental example for the critical slowing down of spin fluctuations in Rb_2MnF_4 measured by neutron three-axis spectroscopy at the antiferromagnetic magnetic Bragg peak $\boldsymbol{Q} = (010)$, with $T_N = 38.4$ K. The energy width increases with temperature, indicating that the lifetime of the critical fluctuations decreases. From [8].

z is the dynamic critical exponent. The quantity $\Omega = (q/\kappa)^z \Omega'$ is a homogeneous scaling function in q/κ, which depends on the static universality class. Experimentally, these relations can be verified by measuring the characteristic frequency as a function of the wave vector q at the critical temperature or as a function of temperature at the magnetic zone center $q = 0$. The quantity $\omega_c^{-1}(q, \kappa)$ is the lifetime of the spin fluctuations and is proportional to $t^{-z\nu}$ [see Eq. (2.19)]. This feature is the so-called critical slowing down of spin fluctuations, which is connected to the static critical exponent ν for a given universality class. Fig. 2.2 shows a typical example of such behavior in Rb_2MnF_4 [8].

Table 2.4 lists the dynamic critical exponents z for different spin systems, which is adapted from [7]. The dynamic critical phenomena are described as subsets of the static

Model system	Universality (n,d)	Conserving fields		Expression for z	z $(d=3)$
		yes	no		
Heisenberg ferromagnets (Model J)	$(3,d)$	M	–	$(d+2-\eta)/2$	$\sim 5/2$
Heisenberg antiferromagnets (Model G)	$(3,d)$	E	M	$d/2$	$3/2$
Anisotropic magnets (Model C)	$(1,d)$	E	M	$2+\alpha/\nu$	~ 2
Kinetic Ising anisotropic magnets (Model A)	(n,d)	–	M	$2+c\eta$ $c\sim 0.72$	~ 2

Table 2.4: Dynamic critical exponents z in different spin systems. For the conserving fields, M and E denote the order parameter and the energy, respectively. From [7].

universality classes in terms of (n,d), the spin (n) and lattice (d) dimensionalities. Besides the static universality class [see Sec. 2.1.1], the conservation laws of energy and spin of a system have to be taken into account for the critical dynamics. In the Heisenberg (isotropic) antiferromagnet (Model G of [7]) the order parameter M (staggered magnetization) is a non-conserved quantity, whereas in the Heisenberg ferromagnet (Model J of [7]) M is a conserved variable and commutes with the total energy E. This fact leads to different expressions of z for ferromagnets with $z=(d+2-\eta)/2$ and antiferromagnets with $z=d/2$, even if they belong to the same universality class $(3,d)$. The Models C and A correspond to anisotropic ferro- and antiferromagnets and possess a similar critical exponent $z\sim 2$. The physical origins of the anisotropic spin arrangements are somewhat relevant: the kinetic Ising model in Model A concerns the dynamic properties of systems with significant relaxation due to phonon or dipolar interactions, which break the conservation laws. The presence of the dipolar interactions causes the spin to align in an anisotropic manner. In discussing the expression of z in Model A, the small static critical exponent η in three-dimensional systems [53, 54] leads to the dynamic critical exponent $z\sim 2$. On the other hand, the conventional or Van Hove theory [34] states that the characteristic width ω_c is proportional to the inverse static susceptibility χ,

$$\omega_c \sim \chi^{-1} \sim \xi^{-2+\eta}. \tag{2.21}$$

Considering the dynamic critical exponent defined by $\omega_c \sim \xi^{-z}$, we obtain the so-called conventional (Van Hove) dynamic critical exponent $z=2-\eta$, suggesting $c=-1$ in the expression of Model A. Experimentally, this conventional exponent has been confirmed

for two-dimensional Ising model systems with $\eta = 0.25$ [32, 33, 70, 71].

In summary, the theory of dynamic critical phenomena by Hohenberg and Halperin offers a first insight to the dynamic properties in several model systems. However, much less information is available for the influences of non-conserving forces on the critical dynamics, which may cause crossover behavior in the critical region. It is the main task in this thesis to explore the critical dynamics in Heisenberg magnets with dipolar anisotropy.

In the following section, we review experimental results of dynamic critical phenomena for model systems with different spin and lattice dimensionalities and with different types of spin arrangements including ferromagnets and antiferromagnets. The experimental techniques to investigate critical dynamics discussed here include neutron scattering (NS), neutron spin-echo spectroscopy (NSE), nuclear magnetic resonance (NMR), electron spin resonance (ESR), muon spin relaxation (μSR), perturbed angular correlations (PAC) of γ-ray spectroscopy and the Mössbauer effect (ME).

2.1.2.1 The three-dimensional model ferromagnets

Dynamic critical phenomena were first studied in 3D Heisenberg ferromagnets (3D HFMs). In the 1970's, NS studies on Ni [72], Fe [73], and EuO [74] found dynamic critical exponents consistent with the exponent $z = 2.5$ expected for the 3D HFM scaling. In a pioneering PAC study, Chow *et al.* [75] measured the spin autocorrelation times for Ni and Fe, as shown in Fig. 2.3 (a). The slope of the fitted lines depends on z, ν, and η. z can be extracted under the assumption of a given universality class. z shows a change on cooling towards T_c. This change happens around the crossover temperature $t_x \sim 10^{-2}$ in both Ni and Fe. z crosses from the 3D HFM class with $z = 2.5$ well above t_x to the 3D dipolar FM class with $z = 2$ below t_x. With the invention of NSE, Mezei pushed the energy resolution of NS down to the μeV range, which allowed him to study the critical dynamics of poly-crystalline Fe and EuO close to T_c. The $z = 2.5$ found in Fe [47] and EuO [48, 76] is in good agreement with the 3D HFM. In contrast to NS, ESR studies allow one to measure the relaxation rates of spin fluctuations at $q = 0$ and at temperatures very close to T_c. Dunlap *et al.* [77] found $z = 2$ by ESR in EuO. This means there is a crossover in z between the parameter regions sampled by neutrons and ESR. The ESR data show strong evidence for the $z = 2$ dipolar FM class for $q = 0$ and for a very small reduced temperature in the order of 10^{-4}, in the so-called asymptotic critical region. A collection of experimentally determined z from selected materials and related theoretical predictions is listed in Table 2.5.

The crossover behavior in z in the scaling relation of Eq. (2.19) and Eq. (2.20) in the 3D HFMs results from the spin anisotropies. The latter originates from dipolar interactions or from crystal fields. It was realized that the long-range dipolar field, which does

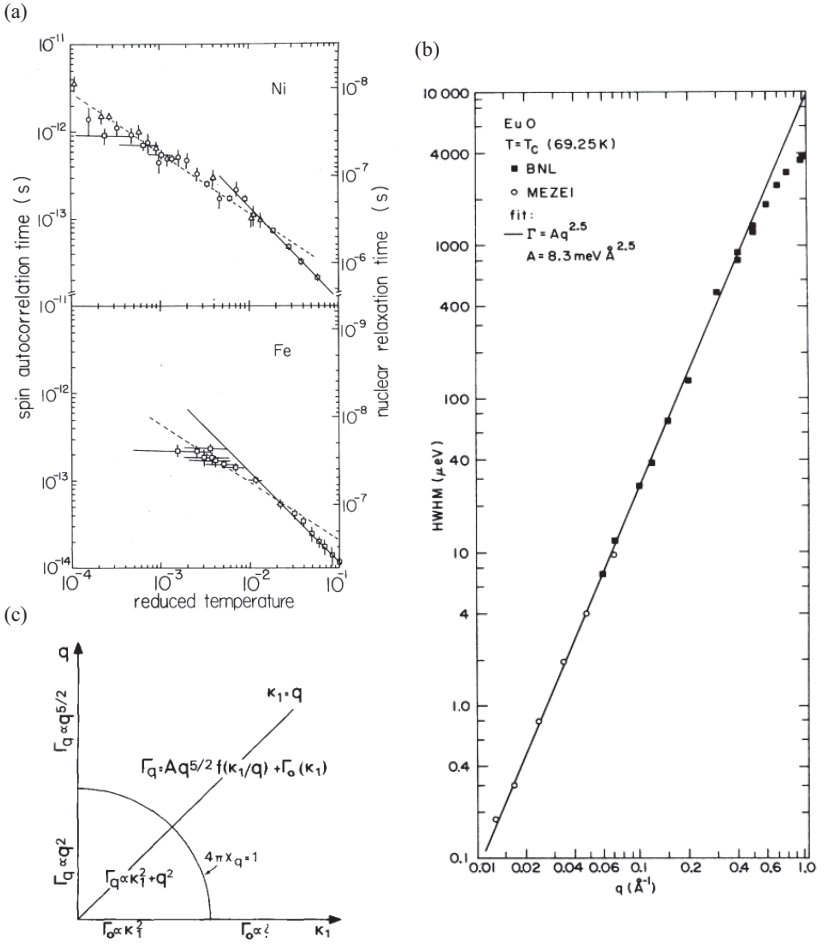

Fig. 2.3: (a) The divergence of spin autocorrelation time above T_c of Ni and Fe, deduced from the nuclear relaxation time of a PAC experiment. Both in Ni and Fe the scaling crosses from the the HFM ($z = 2.5$) to the dipolar FM ($z = 2$) class. The crossover temperatures are at around $t = 10^{-2}$. From [75]. (b) Energy linewidth Γ versus q at $T = T_c$ for EuO, obtained from NSE [48, 76] and NS [78]. The experimental data follow the prediction of 3D HFM ($z = 2.5$) up to $1/3$ of the zone boundary. (c) The scaling regions in the $q - \kappa$ plane with a crossover boundary line. From [79].

System	method	z	t or $q(\text{Å}^{-1})$ range	Reference
Ni	NS	2.45(25)	q : 0.04 – 0.2	Minkiewicz 1969 [72]
	PAC	2.06(4)	$t : 1 \times 10^{-4} - 0.01$	Chow 1980 [75]
		2.5(2)	t : 0.01 – 0.06	Hohenemser 1982 [27]
Fe	NSE	2.48(5)	q : 0.01 – 0.3	Mezei 1982 [47]
	PAC	2.06(4)	$t : 2 \times 10^{-3} - 0.01$	Chow 1980 [75]
		2.5(2)	t : 0.02 – 0.1	Hohenemser 1982 [27]
EuO	NS	2.29(3)	q : 0.12 – 0.48	Dietrich 1976 [74]
	ESR	2.04(7)	$t : 3 \times 10^{-4} - 0.1$	Dunlap 1980 [77]
	NS	2.50(5)	q : 0.01 – 0.4	Mezei 1984 [48]
	NSE			Mezei 1986 [76]
Theory	–	2.5	Heisenberg FMs [7] (Model J)	
Theory	–	2	Dipolar FMs [7] (Model A)	

Table 2.5: Observed and predicted z in 3D ferromagnets (FMs). NS: neutron scattering; PAC: perturbed angular correlations of γ-ray spectroscopy; ESR: electron spin resonance; NSE: neutron spin-echo spectroscopy.

not conserve spin, can change the critical dynamics drastically. As shown in Fig. 2.3 (c), the dipolar interaction becomes influential as $q^2 + \kappa^2 < q_{\text{d}}^2$, with q_{d} the crossover wave vector. Within the circular segment, the $z = 2$ for the 3D dipolar FM universality class is observed. Outside the circle, the system is expected to be in the isotropic FM class with $z = 2.5$.

For the 3D dipolar FMs, q_{d} is defined from the relation $g = (q_{\text{d}}a)^2$, with a the lattice parameter [15, 80]. The dimensionless quantity g is defined as

$$g = \frac{4\pi a^3}{v_a} \frac{(g_L \mu_B)^2/a^3}{2J}, \tag{2.22}$$

which is proportional to the ratio of the dipolar energy $(g_L\mu_B)^2/a^3$ and the exchange energy $2J$. v_a is the volume of the unit cell. By taking the measured exchange coupling, it allows one to estimate q_{d} to be $0.013\,\text{Å}^{-1}$ for Ni [81], $0.045\,\text{Å}^{-1}$ for Fe [76], and $0.147\,\text{Å}^{-1}$ for EuO [76, 81]. As NS is limited to $q > 0.01\,\text{Å}^{-1}$, the experimental approach to the inner region of the circle is difficult and thus one only observes $z = 2.5$, as in early NS studies in the 1970's. PAC and ESR are intrinsically limited to $q = 0$, and thus sample the inner region of the circle, with $z = 2$. The critical exponents for the 3D FMs Ni, Fe, EuO, and the theoretical results are summarized in Table 2.5.

On the theoretical side, the extended scaling approach for the anisotropic materials [10] and mode coupling studies [15, 80] have suggested that dipolar interactions should affect (non-critical) longitudinal and (critical) transverse correlations in FMs in

a different way. The existence of the dipolar interaction strongly suppresses the longitudinal fluctuations, leading to a finite susceptibility as the critical temperature is approached [82]. As a result, the non-critical fluctuations cross from $z = 2.5$ to $z = 0$ while the critical fluctuations changeover from $z = 2.5$ to $z = 2$. However, an experimental verification of these predictions is still lacking, mainly due to the technical difficulties in sufficiently separating the longitudinal and transverse correlations of materials in NS, ESR, and PAC experiments.

2.1.2.2 The three-dimensional model antiferromagnets

As mentioned above, the dynamic critical properties in ferromagnets and antiferromagnets are different due to their conservation laws. Here we review basic properties of the 3D antiferromagnets, where the reduced anisotropic energy α_I, the ratio of anisotropic energy and the exchange interaction, plays a key role.

$RbMnF_3$ is known as a nearly ideal 3D isotropic Heisenberg antiferromagnet (3D HAFMs) with very small $\alpha_I = 6 \times 10^{-6}$ [83, 84]. The static critical exponents, such as β, ν, γ, and η, have been previously measured by NS, consistent with the 3D Heisenberg universality class [28]. The dynamic critical exponent $z = 1.43 \pm 0.04$ below and above T_N is close to the value $z = 1.5$ predicted by the dynamic scaling theory for the 3D HAFM scaling (model G [7]). More recently, this fact has been confirmed by Tsai and Landau [16] using Monte Carlo simulations.

For anisotropic systems with larger α_I, including MnF_2, FeF_2, and CoF_2, the static properties are best represented by the 3D Ising model. However, only FeF_2 [85, 86] and CoF_2 [7] follow the dynamic scaling theory with $z = 2$ for the 3D Ising antiferromagnet (3D IAFM) scaling. Table 2.6 shows that the dynamic critical exponent of MnF_2 strongly depends on the experimental methods: z ranges from $1.49(7)$ by NS to $2.3(3)$ by μSR. The origin of these discrepancies probably results from the different q ranges sampled by these methods. As for the NS data of MnF_2, Fig. 2.4 (a) and (b) show the temperature and wave vector dependence of the characteristic energy widths $\Gamma_\parallel(q = 0, t)$ and $\Gamma_\parallel(q, t = 0)$, respectively.

$$\Gamma_\parallel(q = 0, t) = (6.6 \pm 0.6)\left[\kappa_\parallel(T)\right]^{1.49\pm0.07} \text{ meV} \tag{2.23}$$

$$\Gamma_\parallel(q, t = 0) = (7.0 \pm 0.9)\, q^{1.6\pm0.2} \text{ meV} \tag{2.24}$$

$z = 1.49(7)$ and $z = 1.6(2)$ are close to the prediction of the 3D HAFM scaling with $z = 1.5$, although the static exponents follow the 3D Ising model [13, 87]. This discrepancy likely results from the weak anisotropy and from limited momentum and energy resolution of conventional spectrometers, as discussed for the 3D FMs.

Riedel and Wegner [10, 11] have calculated the critical properties of the longitudinal

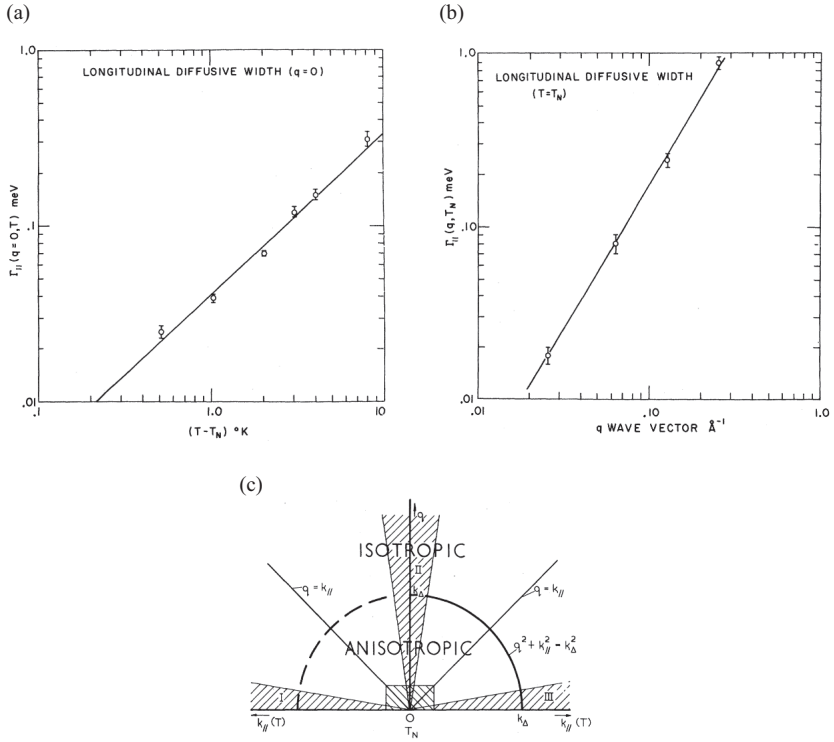

Fig. 2.4: (a) Temperature and (b) wave vector dependence of the longitudinal energy linewidth $\Gamma_\parallel(q=0,t)$ and $\Gamma_\parallel(q,t=0)$ for MnF_2, giving $z=1.49(7)$ and $z=1.6(2)$. From [13]. (c) $q-\kappa$ plane. The circle $q^2+\kappa_\parallel^2=\kappa_\Delta^2$ separates the anisotropic ($\kappa_\parallel \ll \kappa_\Delta$) and isotropic ($\kappa_\parallel \gg \kappa_\Delta$) critical regions of a system. From [86].

($\Gamma_\parallel$) and transverse ($\Gamma_\perp$) energy linewidths for MnF_2 and FeF_2 in the anisotropic (a) and isotropic (i) limits.

$$\Gamma_\perp^a = 0.3\,\text{meV}, \quad \Gamma_\parallel^a = 27\kappa_\parallel^2\,\text{meV}, \quad \Gamma_{\perp,\parallel}^i = 8.6\kappa_\parallel^{1.5}\,\text{meV} \quad \text{for } MnF_2 \tag{2.25}$$

$$\Gamma_\perp^a = 4.5\,\text{meV}, \quad \Gamma_\parallel^a = 17\kappa_\parallel^2\,\text{meV}, \quad \Gamma_{\perp,\parallel}^i = 12\kappa_\parallel^{1.5}\,\text{meV} \quad \text{for } FeF_2. \tag{2.26}$$

The crossover wave vector κ_Δ is represented by a boundary circle $q^2+\kappa_\parallel^2=\kappa_\Delta^2$ in the $q-\kappa_\parallel$ plane, separating these two critical regions [see Fig. 2.4 (c)]. In both MnF_2 and FeF_2, close to T_N the anisotropic interactions suppress the transverse fluctuations. This

3D Heisenberg AFMs:

System	method	z	t or $q(\text{Å}^{-1})$ range	Reference
$RbMnF_3$	NS	1.46(13)	t : 0.04 – 0.1	Tucciarone 1971 [28]
	NS	1.43(4)	q : 0.02 – 0.12	Coldea 1998 [29]
Theory	–	1.5	Heisenberg AFMs [7] (Model G)	
Theory	MC	1.49(3)	Tsai 2003 [16]	

3D Ising AFMs:

System	method	z	t or $q(\text{Å}^{-1})$ range	Reference
MnF_2	NMR	1.75(5)	$t : 2.2 \times 10^{-4} - 1.5 \times 10^{-2}$	Heller 1966 [30]
	NS	1.6(2)	q : 0.026 – 0.26	Schulhof 1971 [13]
		1.49(7)	$t : 7.8 \times 10^{-3} - 0.12$	
	μSR	2.3(3)	t : 0.01 – 0.1	de Renzi 1984 [31]
FeF_2	NMR	2.0(3)	$t : 5.1 \times 10^{-4} - 1.7 \times 10^{-2}$	Gottlieb 1971 [85]
	NS	2.1(2)	q : 0.067 – 0.4	Hutchings 1972 [86]
		2.3(4)	$t : 5.7 \times 10^{-4} - 0.08$	
CoF_2	μSR	2.09	$t : 1.3 \times 10^{-3} - 6.6 \times 10^{-3}$	de Renzi 1984 [31]
Theory	–	2	Anisotropic AFMs [7] (Model C)	

Table 2.6: Measured and calculated z in 3D antiferromagnets (AFMs). NS: neutron scattering; MC: Monte Carlo; NMR: nuclear magnetic resonance; μSR: muon spin relaxation.

leads in the anisotropic limit to a finite constant value of $\Gamma_\perp^a$ with $z_\perp = 0$. The dynamic critical exponent z of the longitudinal fluctuations crosses from $z_\parallel = 1.5$ in the 3D (isotropic) HAFM class to $z_\parallel = 2$ of the 3D (anisotropic) IAFM class. In the isotropic limit with $\kappa_\parallel \gg \kappa_\Delta$ (or $T \gg T_N$), $\Gamma_\parallel$ and $\Gamma_\perp$ become identical and $z_\parallel = z_\perp = 1.5$. κ_Δ was calculated as $0.054\,\text{Å}^{-1}$ and $0.29\,\text{Å}^{-1}$ for MnF_2 anf FeF_2, respectively. With the experimental results of $\kappa_\parallel$ [13, 86], the corresponding crossover temperatures can be estimated as $t_x = 0.03$ and $t_x = 0.4$. These small values of κ_Δ and t_x explain the discrepancy found in MnF_2, where q and t were not sufficiently small to reach the 3D anisotropic critical region. On the other hand, experimental results of FeF_2 [85, 86] show no contradictions with the 3D IAFM model, because κ_Δ and t_x are relatively large and the 3D IAFM scaling region is easily accessible by experiments. Table 2.6 summarizes the experimental and theoretical results of z for the 3D IAFM and 3D HAFM model systems. Following the crossover behavior of 3D dipolar FMs, Frey and Schwabl [15] further discussed the case for the 3D dipolar AFMs. On the basis of Eq. (2.22), they calculated the characteristic wave vector of AFMs,

$$\kappa_\Delta = \left(\frac{1}{12}\right)^{2/3} (q_d a)^{4/3} q_{BZ}, \tag{2.27}$$

where $q_{BZ} = \pi/a(3/4\pi)^{1/3}$ is the boundary of the first Brillouin zone. Taking the experimentally determined values of the exchange coupling, κ_Δ is about $0.06\,\text{Å}^{-1}$ for MnF_2.

Pfeuty *et al.* [12] have extended the scaling theory to anisotropic systems and predicted the crossover behavior from Heisenberg to Ising universality classes as t approaches zero. The reduced anisotropy $\alpha_I = H_A/H_E$ is introduced as the relevant scaling field of the dynamic scaling hypothesis, where H_A and H_E are the anisotropy field and exchange field of a system, respectively. The crossover phenomenon is postulated to appear at a certain temperature, the so-called crossover temperature t_x.

$$\mid t_x \mid = \mid \alpha_I \mid^{1/\phi} = \mid H_A/H_E \mid^{1/\phi}, \tag{2.28}$$

where ϕ is a crossover exponent and it is calculated to be 1.25 in the 3D case. Thus a system is expected to show 3D Heisenberg behavior in the temperature range $t > t_x$, and is expected to follow the Ising model as $t < t_x$. In the intermediate temperature range $t \sim t_x$, a smooth crossover occurs between the Heisenberg and Ising universality classes. With the experimental values of α_I from the antiferromagnetic resonance studies [88, 89], $t_x(MnF_2) = 0.036$ and $t_x(FeF_2) = 0.45$ are obtained.

2.1.2.3 The two-dimensional Ising model

K_2NiF_4 and compounds with the same structure [19], such as Rb_2MnF_4 and K_2CoF_4, are the best examples for two-dimensional (2D) antiferromagnets, whose magnetic ions have relatively large exchange interactions J between neighboring ions in the planes. Typically, the ratio of the effective interplane coupling J' and J is of the order of 10^{-6}, leading to a 2D spin nature. Another feature of these 2D systems is the reduced anisotropy energy α_I, which determines if the critical dynamics is Ising-like or Heisenberg-like. The anisotropic α_I results from crystal-field effects in the nickel and cobalt salt, and from dipolar interactions in the manganese salt. The magnetic moments are aligned along the crystalline c axis in the ordered state.

On the theoretical side, the static properties of the 2D Ising universality class have been calculated exactly in 1944 by Onsager [20] and have been verified experimentally in the model systems K_2CoF_4 [90] and Rb_2CoF_4 [91]. However, a clarification of the dynamic properties is still lacking: Mazenko and Valls [18] have reviewed different calculations of the dynamic critical exponent z and found a large spread ranging from $z = 1.15$ to $z = 2.95$ in the literature. These discrepancies result from the much narrower asymptotic dynamic critical region than in the static case. On the other hand, the conventional value of the dynamic critical exponent $z = 2 - \eta = 1.75$ [34] holds only if the temperature is not too close T_N.

Experimentally, early NMR studies of K_2CoF_4, K_2MnF_4, and Rb_2CoF_4 were per-

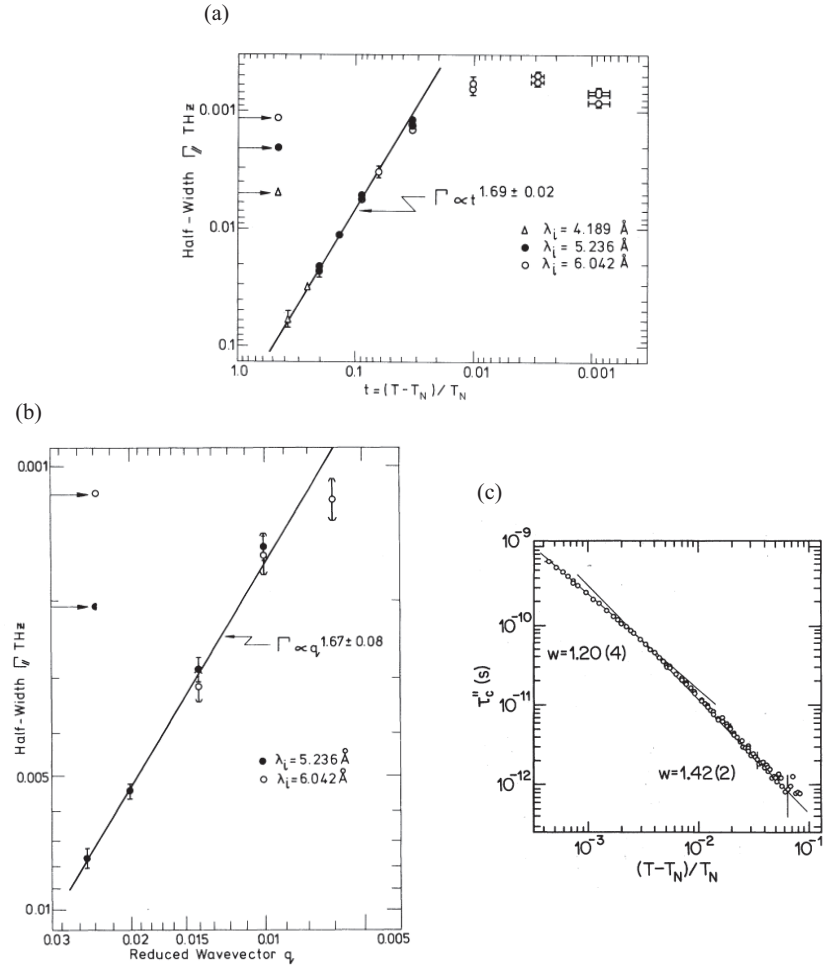

Fig. 2.5: (a) Temperature and (b) wave vector dependence of the longitudinal energy linewidth $\Gamma_\parallel(q=0,t)$ and $\Gamma_\parallel(q,t=0)$ for Rb_2CoF_4, giving $z = 1.69(2)$ and $z = 1.67(8)$. From [71]. (c) ME study on $KFeF_4$ in the critical region. Within the experimental range, the critical exponent crosses from $w = 1.20(4)$ at low t to $w = 1.42(2)$ at high t. From [92].

System	method	z	t or $q(\text{Å}^{-1})$ range	Reference
K_2CoF_4	NMR	1.77(3)	$t: 0.1 - 2$	Bucci 1971 [32]
K_2MnF_4	NMR	1.75(10)	$t: 0.01 - 2$	Bucci 1974 [33]
Rb_2CoF_4	NMR	1.65(5)	$t: 0.1 - 0.4$	Bucci 1972 [70]
	NS	1.67(8)	$q: 0.01 - 0.025$	Hutchings 1982 [71]
		1.69(2)	$t: 3 \times 10^{-2} - 0.4$	
$KFeF_4$	ME	1.77(5)	$t: 5 \times 10^{-3} - 0.1$	Slivka 1984 [92]
		1.55(4)	$t: 4 \times 10^{-4} - 5 \times 10^{-3}$	
Theory	conventional	1.75	Mazenko 1981 [18]	
	others	1.15 – 2.95		

Table 2.7: z in anisotropic 2D antiferromagnets (AFMs). NMR: nuclear magnetic resonance; NS: neutron scattering; ME: Mössbauer effect.

formed by Bucci *et al.* [32, 33, 70]. They found that the dynamic properties match the conventional value of $z = 1.75$ for the 2D Ising AFMs. In NS experiments on Rb_2CoF_4 by Hutchings *et al.* [71], $z = 1.69(2)$ and $z = 1.67(8)$ were obtained by the scaling relations of $\Gamma(q = 0, T)$ *vs.* q and $\Gamma(q, T = T_N)$ *vs.* T, respectively [see Fig. 2.5 (a) and (b)]. These experiments support the conventional value of $z = 1.75$ for the 2D Ising AFMs. However, it is not known whether these studies are sufficiently in the asymptotic critical region or not.

In a surprising ME study of weakly anisotropic $KFeF_4$, Slivka *et al.* [92] found two critical regions while approaching T_N, as shown in Fig 2.5 (c). For ME studies [93], the relation between the critical exponents gives

$$w = \nu(z + 2 - d - \eta), \tag{2.29}$$

where ν, d, and η are known values for a given universality class. In the temperature range $4 \times 10^{-3} < t < 0.1$, $w = 1.42(2)$ or $z = 1.77(5)$ was found in good agreement with the conventional value, while in $4 \times 10^{-4} < t < 5 \times 10^{-3}$ an unconventional value of $w = 1.20(4)$ or $z = 1.55(4)$ was observed. In summary, Table 2.7 shows a list of z obtained from these model systems with experimental conditions and the theoretical predictions.

2.2 Physics of two-dimensional Heisenberg antiferromagnets

After discussing the model systems in the 2D Ising universality class with large α_{I}, we summarize here the properties of two-dimensional Heisenberg antiferromagnets (2D HAFMs) with small α_{I}. For ideal 2D HAFMs, the Mermin-Wagner theorem [94] predicts that there is no transition to magnetic long-range order above $T = 0\,\mathrm{K}$. However, this is clearly not the case for real layered compounds. The interlayer exchange interactions, as well as easy-axis or easy-plane anisotropies of the intralayer interaction lead to a finite transition temperature of the system. Interest in the physics of the 2D HAFMs was renewed following the discovery of high temperature superconductivity in 1986 [95]. The undoped parent compounds of the copper oxide superconductors, such as La_2CuO_4 [35], are nearly ideal representatives of the $S = 1/2$ 2D HAFMs, where pronounced quantum effects are observed. In this section, a brief experimental review of the static and dynamic properties of 2D HAFMs will be presented, ranging from the quantum limit $S = 1/2$ to the classical case $S \to \infty$.

2.2.1 Quantum limit $S = 1/2$

To describe the static and dynamic critical behavior of 2D HAFMs, an effective field theory has first been established by Chakravarty, Halperin, and Nelson (CHN), by mapping the 2D HAFM into the quantum non-linear sigma model [44, 45]. The CHN model gives the correlation length ξ in the renormalized classical region. Later, the CHN theory was extended by Hasenfratz and Niedermayer (HN) [46] to a more precise expression, which is referred to as the CHN-HN formula and is given by

$$\frac{\xi}{a} = \frac{e}{8}\frac{c/a}{2\pi\rho_s} e^{2\pi\rho_s/T}\Big[1 - \frac{1}{2}\Big(\frac{T}{2\pi\rho_s}\Big) + O\Big(\frac{T}{2\pi\rho_s}\Big)^2\Big]. \tag{2.30}$$

a is the lattice constant. $\rho_s = Z_\rho(S)S^2J$ and $c = Z_c(S)2\sqrt{2}aSJ$ are the spin-stiffness and spin-wave velocity, respectively. J is the nearest neighbor exchange coupling constant. One should note that the terms of Z_ρ and Z_c are the quantum renormalization factors depending on S, i.e. $Z_\rho \simeq 0.699$ and $Z_c \simeq 1.18$ are obtained for $S = 1/2$ [96].

On the basis of CHN's work assuming the dynamic scaling hypothesis [6, 7], the dynamic properties of 2D HAFMs have been investigated by Tyc, Halperin, and Chakravarty (THC) using a molecular dynamic simulation [97]. In the scaling region, the dynamic correlation function $S(\boldsymbol{k}, \omega)$ is expressed as

$$S(k, \omega) = \omega_0^{-1} S(k)\Phi(q, \nu), \tag{2.31}$$

$$\omega_0 = c\xi^{-1}(T/2\pi\rho_s)^{1/2}, \tag{2.32}$$

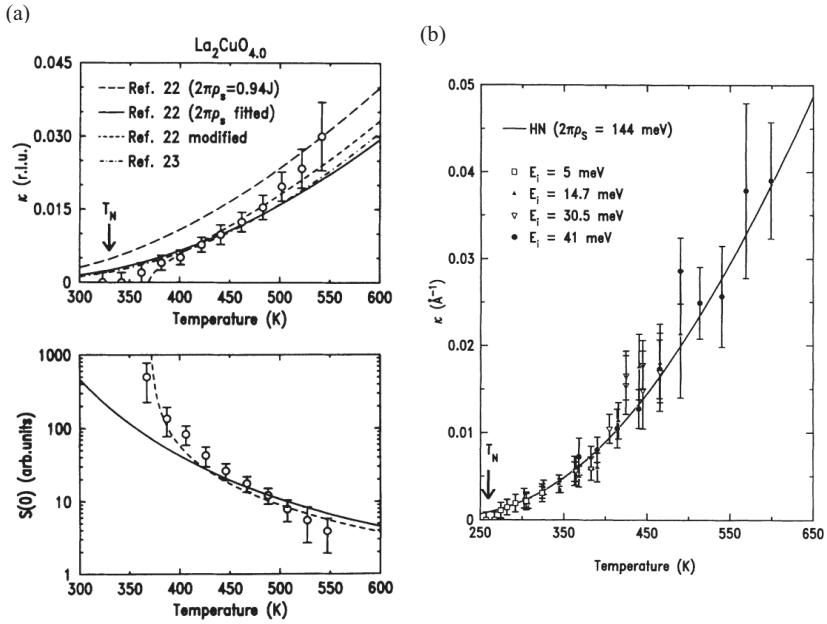

Fig. 2.6: Two experimental representations of static properties for the $S = 1/2$ 2D HAFMs of (a) La_2CuO_4 and (b) $Sr_2CuO_2Cl_2$, together with the prediction by CHN-HN, where the modified ξ due to spin anisotropies was involved. From [35, 36].

where k is the distance from the magnetic zone center and ω_0 is the characteristic energy width. $S(k)$ is the time-averaged correlation function and the dimensionless scaling variables are defined as $\nu = \omega/\omega_0$ and $q = k\xi$. In addition, the temperature dependence of the scattering amplitude S_0 is

$$S_0 \sim \left(\frac{T}{2\pi\rho_s}\right)^2 \xi^2. \tag{2.33}$$

In real compounds, Fig. 2.6 shows the static properties of (a) $S = 1/2$ La_2CuO_4 [35] and (b) $Sr_2CuO_2Cl_2$ [36, 37], which follow the CHN-HN formula reasonably well. Keimer *et al.* [35] have proposed a generic mean-field expression for ξ to account for the effective anisotropy α_{eff}

$$\xi(\alpha_{\text{eff}}, T) = \frac{\xi_0(T)}{\sqrt{1 - \alpha_{\text{eff}}\xi_0(T)^2}}. \tag{2.34}$$

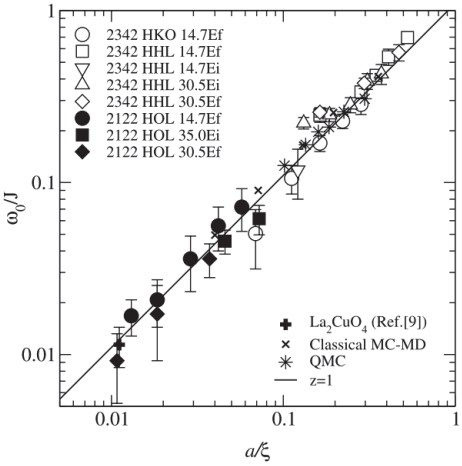

Fig. 2.7: Logarithmic plot of the scaled characteristic width versus inverse correlation length in 2D HAFMs. A comparison of the quantum ($S = 1/2$) and classical ($S = \infty$) Monte Carlo simulations were also made, illustrating that all data are on the same curve as $\omega_0 \sim \xi^{-1}$. From [40].

ξ_0 is the correlation length of the unperturbed 2D HAFM and α_{eff} denotes a combination of the perturbations arising from the anisotropies. In Fig. 2.6 (a), this α_{eff} modification of ξ (dashed curve) shows a much better agreement between the CHN-HN formula and experiment.

As for the dynamic properties of 2D HAFMs, $Sr_2CuO_2Cl_2$ and $Sr_2Cu_3O_4Cl_2$ are the only experimental realizations so far for testing the validity of dynamic scaling $\omega_0 \sim \xi^{-z}$ for $S = 1/2$ [40]. Other copper oxide superconductors like La_2CuO_4 with rather larger $J \sim 100$ meV make neutron scattering experiment difficult to perform at this energy scale. Fig. 2.7 shows the scaled ω_0/J versus a/ξ of $S = 1/2$ $Sr_2CuO_2Cl_2$ (filled symbols) and $Sr_2Cu_3O_4Cl_2$ (open symbols). From there, Kim *et al.* [40] have found the dynamic critical exponent $z = 1.0 \pm 0.1$ for the $S = 1/2$ 2D HAFM, which is in good agreement with the dynamic scaling theory with $z = 1$.

As a result, theoretical work by CHN-HN and THC have nicely captured the static and dynamic properties of $S = 1/2$ 2D HAFM. However, the description of the static properties of 2D HAFM suggested by the CHN-HN formula was reported not to hold for systems with $S > 1/2$. Such experimental results like in K_2NiF_4 [37, 38] and La_2NiO_4 [39] for $S = 1$ and in Rb_2MnF_4 [8, 17, 41] for $S = 5/2$ show large deviations from the CHN-HN formula.

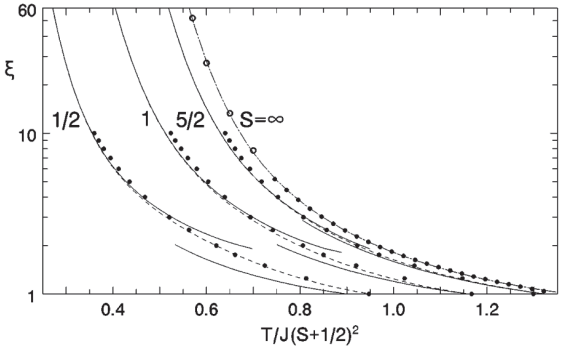

Fig. 2.8: PQSCHA calculations of the correlation length *vs.* the reduced temperature for various spin values S. The solid lines are obtained from the low and high temperature results. The dashed lines are the results by taking the cutoff effect of spin waves. Classical and quantum results of HTE are illustrated as the filled circles. From [42].

2.2.2 Classical limit $S \to \infty$

To resolve the above-mentioned discrepancies found in CHN-HN formula, Elstner *et al.* [98] calculated high-temperature expansions (HTE) for 2D HAFM with different spin values S ranging from $S = 1/2$ to $S = 5/2$. In a different theoretical approach, Cuccoli *et al.* [42, 43] have proposed a semi-classical theory, which is referred to as the pure quantum self-consistent harmonic approximation (PQSCHA), to compute the thermal properties of 2D HAFM with quantum corrections. From both HTE and PQSCHA, these authors observed a strong deviation of the calculated ξ from the CHN-HN theory, especially for large S. Fig. 2.8 shows the HTE and PQSCHA results of ξ in units of lattice constant a for various S, in which the HTE results are only calculated up to $\xi = 10$ and thus are insufficient to describe the high-ξ (low-T) data of classical 2D HAFM.

In the PQSCHA, Cuccoli *et al.* [42, 43, 100] have used the effective Hamiltonian method to treat the pure quantum fluctuations by a self-consistent Gaussian approximation. As for the renormalized terms due to quantum fluctuations, the reduced temperature $t = T/J\tilde{S}^2$ and effective spin length $\tilde{S} = S + 1/2$ are defined, given that the connection between the quantum correlation length $\xi(t)$ and its classical counterpart $\xi_{\rm cl}(t)$ reads

$$\xi(t) = \xi_{\rm cl}(t_{\rm cl}) \quad \text{with} \quad t_{\rm cl} = \frac{t}{\theta^4(t)}, \tag{2.35}$$

where $\theta^4(t)$ is a renormalized temperature factor which approaches unity as $S \to \infty$.

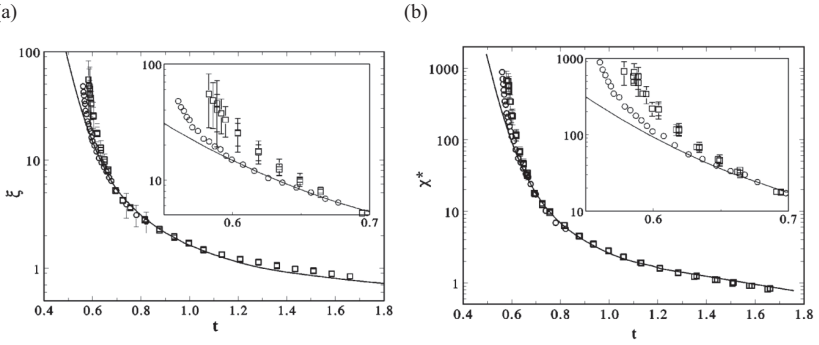

Fig. 2.9: (a) Correlation length and (b) staggered susceptibility $\propto S_0$ versus $t = T/J\tilde{S}^2$ for $S = 5/2$. Experimental data for $KFeF_4$ [99] and Rb_2MnF_4 [17] are expressed in circles and squares, respectively. From [100].

Fig. 2.9 shows the experimental verification of the PQSCHA for $S = 5/2$ $KFeF_4$ [99] and Rb_2MnF_4 [17]. These two compounds possess a nearly identical magnitude of reduced spin anisotropy α_I, with $\alpha_I = 0.0045$ for $KFeF_4$ and $\alpha_I = 0.0047$ for Rb_2MnF_4. Good agreement of the correlation length and staggered susceptibility between the experimental data and calculation are found in the whole temperature range except for the magnified regions, where the crossover behavior, arising from α_I, between the 2D Ising and 2D Heisenberg universality class is expected. In summary, the static properties of 2D HAFM are properly described by the PQSCHA.

The success of the PQSCHA in describing the static properties of $S = 5/2$ 2D HAFM, led the Birgeneau group to re-examine the neutron scattering experiments on the spin dynamics of Rb_2MnF_4. Leheny *et al.* [41] first performed the experiments under external magnetic fields along the spin-flop line proposed by Cowley *et al.* [101]. Thus the spin anisotropy α_I is expected to become irrelevant. Fig. 2.10 (a) shows the field-temperature (H-T) phase diagram of Rb_2MnF_4. The spin-flop line separates the low-field Ising and high-field XY spin phases with a relation

$$H = \sqrt{28.09 + 0.23T}, \tag{2.36}$$

where H and T are in units of Tesla and K. Accordingly, they obtained the static properties of 2D HAFM: the correlation length ξ and static structure amplitude S_0 as a function of temperature. Fig. 2.10 (b) shows that these results are in good agreement with Cuccoli's semiclassical calculation for $S = 5/2$ in the whole experimental region. In addition, S_0/ξ^2 shows a weak temperature dependence at high T, but has a strong

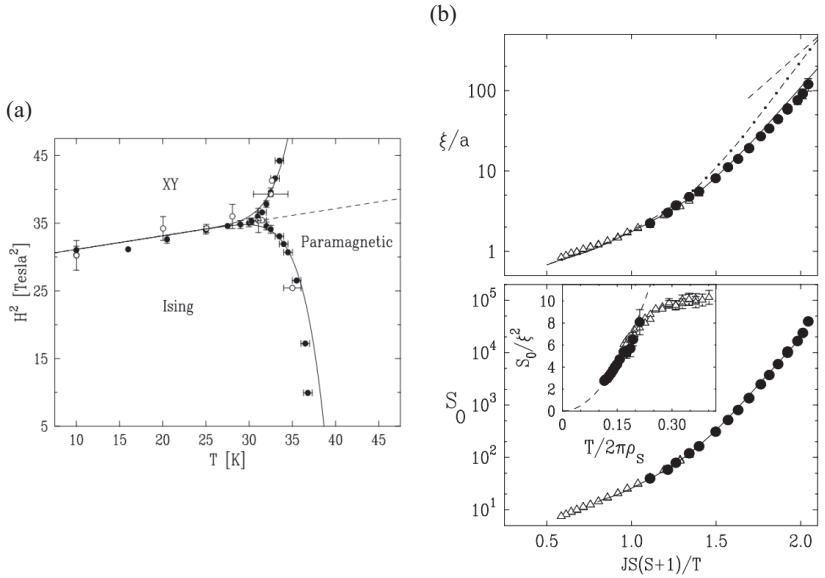

Fig. 2.10: (a) The H-T phase diagram of Rb_2MnF_4. (b) Static properties of the ξ and amplitude of structure factor S_0 as a function of scaled temperature in Rb_2MnF_4. The triangle data are taken from Lee *et al.* [17] without applying magnetic field. From [41].

temperature dependence on T^2 at low T which agrees with the prediction of the low temperature theory for 2D HAFM [see Eq. (2.33)]. This might reflect the crossover behavior between the classical and renormalized classical regions of 2D HAFM [102].

Continuing Leheny's work, Christianson *et al.* [8] performed a quasielastic neutron scattering study under magnetic fields to investigate the dynamic properties of the classical 2D HAFM Rb_2MnF_4. They demonstrated dynamic scaling as in Eq. (2.31) based on the static properties of [41]. Fig. 2.11 (a) shows the temperature profile of characteristic energy widths ω_0, which corresponds to the critical slowing down of the spin fluctuations. Fig. 2.11 (b) plots the energy width ω_0 against the inverse correlation length ξ^{-1} to test the dynamic scaling $\omega \sim \xi^z$. This yielded an unconventional exponent $z = 1.35(2)$, which is significantly different from the predicted exponents $z = 1$ for 2D HAFM and $z = 1.5$ for 3D HAFM scaling. This unsolved discrepancy might originate from differences between the dynamic scaling near the bicritical point and the ideal 2D HAFM scaling. Considering the conservation laws applied to the critical dynamics, the former possesses a conserved uniform magnetization along the magnetic field while the

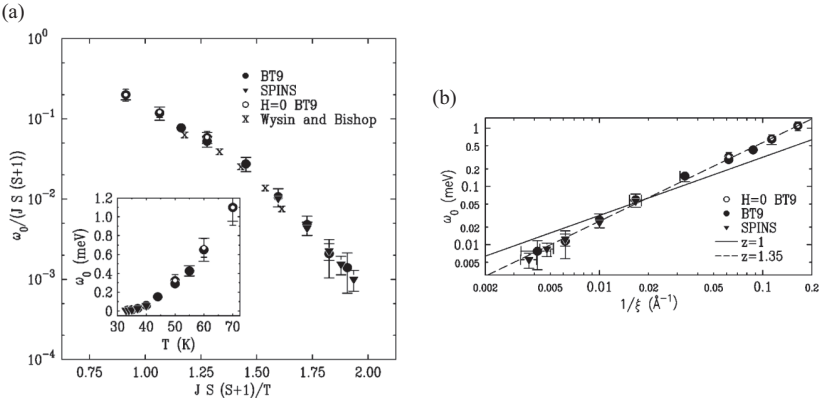

Fig. 2.11: (a) Scaled characteristic widths *vs.* the scaled temperature in Rb_2MnF_4. (b) A demonstration of dynamic scaling $\omega_0 \sim \xi^{-z}$, in which z was found with a deviation from the predicted 2D HAFM. From [8].

latter possesses an non-conserved sublattice magnetization. The 3D bicritical dynamics has been calculated and the resulting exponent was found larger than that for the 3D Heisenberg model [103]. However, studies of the 2D critical dynamics at the bicritical point are still lacking.

In summary, the static properties of 2D HAFMs are in overall agreement with theories, independently of whether the systems are in the quantum or classical limit. For the critical dynamics, only few materials can be used to test the dynamic scaling hypothesis since other 2D HAFMs, such as the parent compounds of the copper based superconductor, have large exchange couplings J. This makes quantitative studies using neutron scattering difficult. Experimentally, only $S = 1/2$ $Sr_2CuO_2Cl_2$ and $Sr_2Cu_3O_4Cl_2$ agree with 2D HAFM scaling, whereas for $S = 5/2$ Rb_2MnF_4, the discrepancy of the measured dynamic critical exponent from theoretical predictions has not yet been fully clarified.

3 Neutron spin-echo spectroscopy

3.1 Neutron scattering

Following the discovery of neutrons by James Chadwick in 1932, the first nuclear reactor "atomic pile" was constructed by Enrico Fermi and his co-workers in 1942. Modern research reactors, such as those at the ILL or the FRM II use compact cores with D_2O moderation to generate high neutron flux densities in the order of 10^{15} neutrons per cm^2 per second. Alternatively, neutrons are generated in a spallation source via the impact of GeV protons on a heavy nuclei such as W or Hg. Modern spallation sources are the SNS, J-Park, ISIS, and the PSI. A current construction project is the European spallation source in Lund.

Neutron scattering has become a valuable tool for probing structural and dynamic properties of solids on an atomic scale. The neutron's de-Broglie wavelength of the order of several Å and the energy of the order of several meV ideally match interatomic distances and the energy of elementary excitations such as phonons and magnons. The neutron is uncharged, which means it can deeply penetrate into the material and there is no Coulomb barrier to be overcome. The neutron interacts with the nucleus by the nuclear force. The cross section depends on the isotope and shows in contrast to X-rays no systematic dependence on the atomic number Z. An important application of this isotope dependence is the contrast variation by replacing hydrogen with deuterium. Further, the neutron carries a magnetic moment, which interacts with unpaired electrons. This is used to study magnetic ordering and spin dynamics.

The triple-axis spectrometer (TAS), invented by Bertram Brockhouse in 1961, is a versatile instrument in performing inelastic neutron scattering to measure the dynamic structure factor $S(\boldsymbol{Q},\omega)$ in momentum-energy ($\boldsymbol{Q}$-ω) space. It thus provides more information than from optical spectroscopy like infrared or Raman spectroscopy, which are limited to $\boldsymbol{Q} = 0$. Subsequently, TAS became a standard tool for measuring the momentum dependence of lattice vibrations (phonons) and spin excitations (magnons) in solids. For this development, Bertram Brockhouse was awarded the Nobel prize in Physics in 1994, together with Clifford Shull for neutron diffraction on antiferromagnetism.

Moving forward to the 1980's, the method of neutron spin-echo (NSE) was invented and developed by Ferenc Mezei [49, 104]. It is substantially different from the con-

ventional TAS method both conceptually and technically. Contrary to the conventional TAS, the energy transfer can be measured with resolution much narrower than the energy spread of the incident beam. In an attempt to measure the intrinsic linewidths of dispersive excitations like phonons, Mezei [105] and Pynn [106] proposed that one can tune the spin-echo resolution function to the slope of the dispersion curve via tilting the field boundaries of the spectrometer arms. With implementation of the inclined field boundaries on conventional NSE spectrometer using dc precession coils, however, several problems were reported. For example stray fields at the coil boundaries restrict the maximum tilting angle to about 10°, which only allowed the phonon-focusing with small group velocity like in superfluid ^{4}He [107]. Later on in 1987, a new solution was realized by Golub and Gähler [50], replacing the DC solenoids to create the static magnetic field used in the first NSE spectrometer with a sequence of radio frequency (RF) spin flipper coils. This is the so-called neutron resonance spin-echo (NRSE) technique, which allows one to shift the field boundary tilt angles up to 50° for the phonon-focusing technique.

At present, there are only few NRSE-TAS spectrometers in the world, for example the IN22 with the ZETA option (thermal source) at the Institut Laue-Langevin, Grenoble [108], TRISP (thermal source) at the FRM II, Garching near Munich and FLEXX (cold source) at the Helmholtz-Zentrum Berlin [107, 109]. Detailed illustration of the phonon-focusing technique are displayed in most recently PhD dissertations by Aynajian and Munnikes [110, 111]. In this chapter we discuss the application of spin-echo to quasielastic scattering and a new analysis technique for magnetic excitations.

3.2 Neutron spin-echo for quasi-elastic scattering

In an inelastic scattering process, the kinematics is governed by the laws of momentum and energy conservation.

$$\boldsymbol{Q} = \boldsymbol{k}_\mathrm{i} - \boldsymbol{k}_\mathrm{f} = \boldsymbol{G} + \boldsymbol{q} \tag{3.1}$$

$$E = \frac{\hbar^2}{2m_n}(k_\mathrm{i}^2 - k_\mathrm{f}^2) \tag{3.2}$$

From the above equations, the difference of the neutron wave vectors ($\boldsymbol{k}_\mathrm{i}$ and $\boldsymbol{k}_\mathrm{f}$) before and after a scattering process is defined, giving rise the total transferred momentum vector $\boldsymbol{Q}$ and energy transfer with m_n the neutron mass and $\hbar$ the reduced Planck's constant. $\boldsymbol{G}$ and $\boldsymbol{q}$ are respectively defined as the reciprocal lattice vector and relative vector within a Brillouin zone. The magnitude of the wave vector $k = 2\pi/\lambda$, where λ is the wavelength of the neutron beam.

Conventional neutron scattering is discussed in textbooks, e.g. in [112, 113, 114],

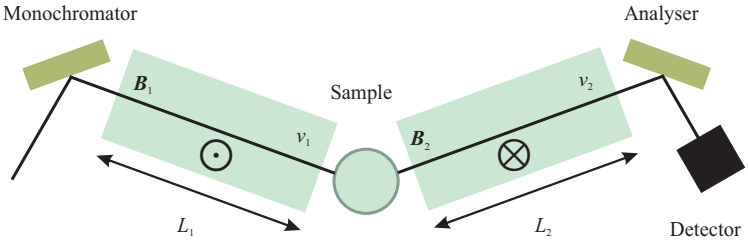

Fig. 3.1: Schematic layout of a neutron spin-echo apparatus for a non-spinflip scattering process.

using the formalism proposed by Van Hove [34]. The scattering cross section is proportional to $S(\boldsymbol{Q},\omega)$, the space and time Fourier transform of the time-dependent (τ) pair correlation function of the scattering system,

$$G(\boldsymbol{R},\tau) = \langle \rho(\boldsymbol{r},t)\,\rho(\boldsymbol{r}+\boldsymbol{R},t+\tau)\rangle, \tag{3.3}$$

where ρ is the scattering length density. In contrast to most conventional instruments, the NSE spectrometer can directly measure τ (and to some extent the $\boldsymbol{R}$) dependence of the $G(\boldsymbol{R},\tau)$, where $G(\boldsymbol{R},\tau)$ is in fact the more physically meaningful quantity, although most theories are formulated in the $(\boldsymbol{Q},\omega)$ space. In spin-echo, the energy transfer to the neutrons during scattering by a sample is measured via comparing the difference of Larmor precession before and after the scattering process. As a result, the measured quantity, the average neutron polarization, is proportional to the Fourier transform of the energy transfer spectrum. In the following, a simplified classical model of Larmor precession and NSE limited to quasi-elastic scattering is presented. For simplicity, we first restrict ourselves here to non-spin-flip scattering process, whereas magnetic spin-flip scattering processes are discussed in an analysis technique [see Sec. 3.4.2].

As a starting point, Fig. 3.1 shows a schematic setup of a NSE spectrometer. Neutrons with velocity $\boldsymbol{v}_1$ are assumed to travel along the trajectory (shown as black solid line). The neutron spins are initially polarized along the direction perpendicular to $\boldsymbol{v}_1$ and the magnetic field $\boldsymbol{B}_1$. The neutron spins precess in the first field region with length L_1, which can be driven either by RF spin flippers (*NRSE* mode) or by a DC coil (*DC* mode). The Larmor phase after passing $\boldsymbol{B}_1$ in the first spin-echo arm is

$$\phi_1 = \omega_L^{(1)}\frac{L_1}{v_1} = \frac{m}{\hbar}\frac{\omega_L^{(1)}L_1}{k_1}, \tag{3.4}$$

where $\omega_L^{(1)}$ and the following $\omega_L^{(2)}$ are the effective Larmor frequencies in the first

and second spin-echo arms, as illustrated in Sec. 3.3. After leaving the first precession region, the neutrons impinge onto a sample and enter the second precession region. In the second precession region (L_2) with *opposite* magnetic field $\boldsymbol{B}_2$ to the first spin-echo arm, the spins precess by

$$\phi_2 = -\omega_L^{(2)} \frac{L_2}{v_2} = -\frac{m}{\hbar} \frac{\omega_L^{(2)} L_2}{k_2}. \tag{3.5}$$

Taking $L_{1,2} = L$, $\omega_L^{(1,2)} = \omega_L$ and assuming $v_1 = v_2 + \delta v$ for quasi-elastic scattering to fulfill the spin-echo condition, the net Larmor phase is

$$\phi_{\mathrm{NSE}} = \phi_1 + \phi_2 = \omega_L L \left[\frac{1}{v_1} - \frac{1}{v_2} \right] = \frac{\omega_L L}{{v_1}^2} \delta v, \tag{3.6}$$

and the energy transfer ω is denoted by

$$\hbar\omega = \frac{m}{2} \left({v_1}^2 - {v_2}^2 \right) = m v_1 \delta v. \tag{3.7}$$

As a result, ϕ_{NSE} in Eq. (3.6) can be rewritten as

$$\phi_{\mathrm{NSE}} = \omega \frac{\hbar \omega_L L}{m v_1^3} \equiv \omega \tau_{\mathrm{NSE}}, \tag{3.8}$$

where $\tau_{\mathrm{NSE}} = \hbar \omega_L L / m_n v_1^3$ is defined as the spin-echo time, which depends on the magnetic field integral along the neutron's path and the neutron velocity.

Since $S(\boldsymbol{Q}, \omega)\, \mathrm{d}\omega$ describes the probability of a neutron being scattered with $\hbar\omega$, the measured quantity of NSE gives the average neutron polarization P as

$$\mathrm{P} = \langle \cos(\phi_{\mathrm{NSE}}) \rangle = \int S(\boldsymbol{Q}, \omega) \cos \phi_{\mathrm{NSE}}\, \mathrm{d}\omega \tag{3.9}$$

the Fourier cosine transform of $S(\boldsymbol{Q}, \omega)$. It has been shown [34] that Eq. (3.9) is identical to the intermediate scattering function

$$\mathrm{I}(\boldsymbol{q}, \tau_{\mathrm{NSE}}) = \int \langle \rho(\boldsymbol{r}, t)\, \rho(\boldsymbol{r} + \boldsymbol{R}, t + \tau_{\mathrm{NSE}}) \rangle\, \mathrm{d}^3 \boldsymbol{R}. \tag{3.10}$$

In the common case of a damped harmonic oscillator, the energy spectrum $S(\omega)$, the scattering law, is distributed over a ω range in the form of a Lorentzian function with half width at half maximum (HWHM) Γ, i.e.

$$S(\omega) = \frac{1}{\pi} \frac{\Gamma}{\Gamma^2 + \omega^2}. \tag{3.11}$$

This fact yields an exponential decay in the polarization,

$$\mathrm{P}(\tau_{\mathrm{NSE}}) = \mathrm{P}_0 \exp\left(-\frac{\Gamma \cdot \tau_{\mathrm{NSE}}}{\hbar}\right). \tag{3.12}$$

3.3 The NRSE-TAS spectrometer TRISP

TRISP is a novel high-resolution NRSE-TAS spectrometer, operated by the Max Planck Institute at the FRM II neutron source in Garching near Munich [115, 116]. A schematic top view of TRISP is shown in Fig. 3.2. At FRM II, the beam tube SR-5b equipped with a polarizing supermirror bender provides polarized thermal neutrons with wavelengths $0.8\,\text{Å} < \lambda < 4\,\text{Å}$ to TRISP, followed by a velocity selector to cut out high-order contamination of the incident beam. The pyrolytic graphite (PG) monochromator crystals for the (002) or (004) allow for vertically- and horizontally-focusing of the neutron beams. In the first and second spin-echo arms of the spectrometer, two RF spin flippers (standard, *NRSE* mode) or DC coils (optional, *DC* mode) are used to drive Larmor precession. In both spin-echo arms, surrounding mu-metal shields reduce the magnetic field along the beam path. Variable horizontally-focusing Heusler (Cu_2MnAl) alloy crystals (111) are used as an analyzer in front of the ^{3}He detector. At TRISP, there are two ways, the *NRSE* and *DC* modes, to drive the Larmor precession. In the following, the key features of these modes are

- *NRSE* mode: Each single RF coil incorporates a static vertical DC field $\boldsymbol{B}_0$ and a rotating magnetic field $\boldsymbol{B}_{\mathrm{rf}} \propto \cos(\omega_L t)$ in the scattering plane, with a frequency `FREQ` [kHz] in the range 50 – 400 kHz. The effective Larmor frequency ω_L can be expressed as

$$\omega_L = 2\pi\nu_L = 2\pi \cdot \texttt{FREQ} \cdot 10^3 \cdot \texttt{RFMODE}/2. \tag{3.13}$$

  ν_L is the effective frequency applied in the spin-echo arms. The value `RFMODE` defines the case of 2 (normal mode) or 4 (bootstrap mode) RF spin flippers coils operating per arm. In addition, the length of one spectrometer arm L corresponds to the assigned `RFMODE`, $L = 0.5$ m in bootstrap mode and $L = 0.406$ m in normal mode. For the *NRSE* mode, τ_{NSE} can be expresses as

$$\tau_{\mathrm{NSE}}[s] = 6.3897 \times 10^{-14} \cdot \nu_L[\mathrm{MHz}] \cdot L[cm] \cdot \lambda^3[\text{Å}] \tag{3.14}$$

$$= 4.0231 \times 10^{-15} \cdot \phi_{\mathrm{NSE}}[rad] \cdot \lambda^2[\text{Å}]. \tag{3.15}$$

  As a consequence the RF coils can only be operated in the range $\tau_{\mathrm{min}} \leq \tau_{\mathrm{NSE}} \leq 20 \times \tau_{\mathrm{min}}$. τ_{min} is the smallest approachable τ_{NSE} at `FREQ` = 50 and `RFMODE` = 2,

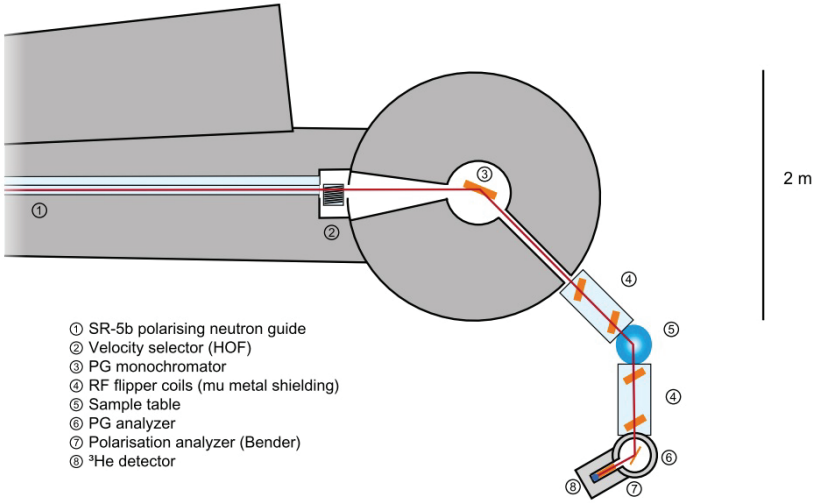

Fig. 3.2: The NRSE-TAS spectrometer TRISP at the FRM II, Garching. From [116].

with $\tau_{\min} = 4.09\,\text{ps}$ at $k_i = 2\pi/\lambda = 2.51\,\text{Å}$.

- *DC* mode: The DC coils are rectangular coils with mu-metal yokes to suppress the external stray field and generate a nearly homogeneous magnetic field $\boldsymbol{B}_0$, where the current in the 1 mm Al wire is driven up to 15 A. The effective Larmor frequency reads

$$\omega_L = 2\pi\gamma_n B_0 \quad \text{with} \quad \gamma_n = 2.916\,\text{kHz/Gauss}. \tag{3.16}$$

  γ_n is the neutron's gyromagnetic ratio. The advantage of the *DC* coils is that τ_{NSE} can be tuned continuously down to zero. This is not possible in the *NRSE* mode, where the range of τ_{NSE} smaller than $\tau_{\min} \simeq 10\,\text{ps}$ is not accessible.

The current setup in the *NRSE mode* at TRISP is well-suited for most of the cases in studying the dynamic properties of solids. However, in dynamic processes with strong relaxation already in the τ_{NSE} range below 10 ps, the use of DC coils is crucial. In this case, the spin-echo signal is often more complicated than the simple exponential decay [see Eq. (3.12)], and thus needs a more complicated analysis technique.

3.4 Analysis of spin-echo data including spin-flip scattering

Within the scope of this thesis, we are investigating the magnetic critical fluctuations of anisotropic materials. For the strong relaxation of critical dynamics, both the *NRSE* mode and *DC* mode at TRISP were employed to cover the whole experimental τ_{NSE} range $0 \leq \tau_{\mathrm{NSE}} \leq 20 \times \tau_{\mathrm{min}}$. Due to the anisotropic effect, a special treatment to separate fluctuations along different directions in $\boldsymbol{Q}$ – space is therefore highly desirable. In the following, we concentrate on the strategy to analyze the complicated neutron spin-echo signal, which includes

- the data combination from the *NRSE* mode and *DC* mode
- the scattering processes resulting from different spin fluctuations
- a conceptually new analysis technique based on the neutron ray-tracing method

The proposed analysis technique tracks the spin phase of each individual neutron from the monochromator, first spin-echo arm, sample, second spin-echo arm, and finally to the detector. It offers a clear and straightforward picture to describe the individual propagation of the neutron spin through the instrument. As a result, the polarization of neutrons, which is the ensemble average of the neutron spin states, can be obtained from the analysis technique.

3.4.1 Data combination: calibrating the *NRSE* and *DC* modes

The aim of the spin-echo experiment is to determine the polarization $\mathrm{P}(\tau_{\mathrm{NSE}})$ for a series of τ_{NSE}'s. For each τ_{NSE}, the precession fields or the frequencies applied to the RF coils are tuned according to Eq. (3.8). The polarization is measured by detuning (scanning) the precession region in one spectrometer arm, leading to a small additional phase $\Delta\phi_{\mathrm{NSE}} = \Delta(BL)$. This detuning is achieved by scanning the length L or the field B of one precession region. At TRISP, a NSE scan can be made through translating the last bootstrap coil (TC4) along the beam direction with the capability of $L = \pm 15\,\mathrm{mm}$ in the *NRSE* mode, or through tuning the driven current I0 up to 15 A in the *DC* mode.

In the beginning, a spin-echo scan using a graphite crystal PG (002) as sample was performed in the *NRSE* mode with $k_{\mathrm{i}} = k_{\mathrm{f}} = 2\,\mathrm{\AA}^{-1}$, $\mathtt{FREQ}_{1,2} = 200\,\mathrm{kHz}$, and $\mathtt{RFMODE} = 8$. The neutron count rate I as a function of the position TC4 of the last bootstrap coil is illustrated in Fig. 3.3 (a). The raw data of a spin-echo scan of the *NRSE* and *DC* modes can be expressed as

$$I = \frac{I_0}{2}\left\{1 + \mathrm{P}\cdot\cos\left[\frac{2\pi(\mathrm{x}-\mathrm{x}_0)}{\Delta x}\right]\right\} \quad (\mathrm{x}\text{: TC4 or I0, P: Polarization}), \tag{3.17}$$

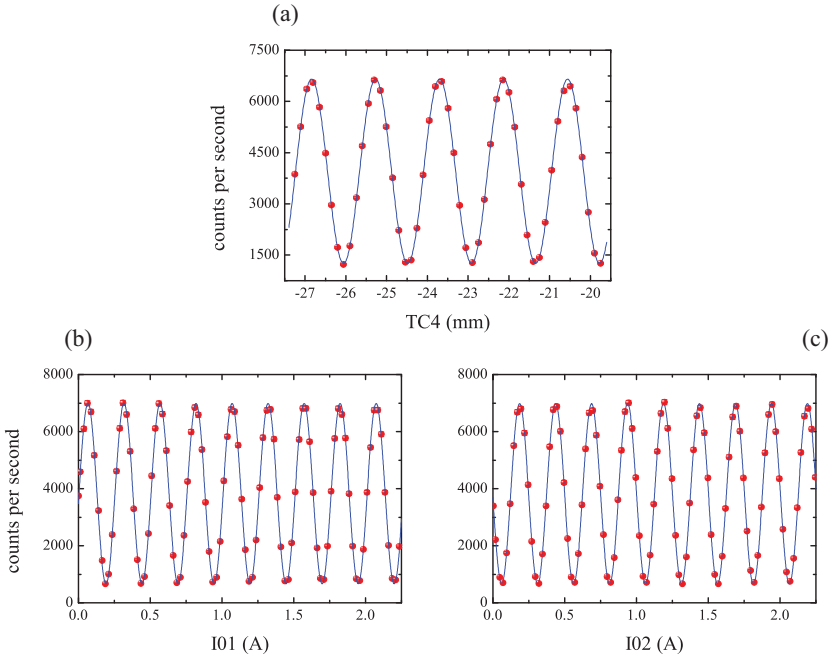

Fig. 3.3: Coil calibration from the NSE scans using (a) the *NRSE mode* and (b,c) the *DC mode*. Separate scans of two DC coils used in the (b) first and (c) second spin-echo arms are manifested.

where the bracket [...] denotes the phase offset $\Delta\phi_{\mathrm{NSE}}$. A fit for the data shown in Fig. 3.3 (a) using Eq. (3.17) gives

$$\mathrm{P} = 0.682(4) \quad \text{and} \quad \Delta\mathrm{TC4} = 1.5707(7)\,\mathrm{mm} \tag{3.18}$$

In the *NRSE* mode, the period of Eq. (3.17) is $\Delta\mathrm{TC4} = 2\pi \times \hbar k_{\mathrm{i}}/(m_n\omega_L)$. Taking the value of ω_L for the current settings, $k_{\mathrm{i}} = 1.9957(9)\,\text{Å}^{-1}$ is deducible and in good agreement with the assigned k_{i}.

While leaving the above configuration unchanged, the RF spin flippers coils are then switched off and replaced by the DC coils. In the *DC* mode, the Larmor phase in a spectrometer arm is assumed to be proportional to $\mathrm{I0(A)}$ and the neutron wavelength

$\lambda(\text{Å})$.

$$\phi_{\text{NSE}} = C_c \cdot \lambda \cdot \text{I0}, \tag{3.19}$$

C_c is an intrinsic DC coil parameter. In a NSE scan, the applied current I01 (I02) in the first (second) spectrometer arm is scanned, while I02 (I01) is kept constant. As a consequence, the small additional phase resulting from this detuning is

$$\Delta\phi_{\text{NSE}} = C_c \cdot \lambda \cdot (\Delta\text{I0}). \tag{3.20}$$

In calibrating the *DC* mode using PG (002), Fig. 3.3 (b) and (c) show two spin-echo scans of I01 and I02 at I02 = 0 and I01 = 0, respectively. Concerning the observed periods $\Delta\text{I0} = 2\pi/(C_c\lambda)$ found in I01 and I02 scans, one obtains the intrinsic parameter $C_c = 7.958\,\text{Å}^{-1}\text{A}^{-1}$. Combining Eq. (3.15) and Eq. (3.19), τ_{NSE} for the *DC* mode becomes

$$\tau_{\text{NSE}}[s] = 3.2016 \times 10^{-14} \cdot \lambda^3[\text{Å}] \cdot \text{I0}[\text{A}]. \tag{3.21}$$

To combine the experimental data from the *NRSE* and *DC* modes [see Eq. (3.14) and (3.21)], the conversion relation between these modes yields

$$\tau_{\text{NSE}}[\text{ps}] = 0.12289 \cdot \tau_{\text{min}} \cdot \text{I0}[\text{A}]. \tag{3.22}$$

3.4.2 Magnetic scattering process

For magnetic neutron scattering, only the components of the spin fluctuations $\boldsymbol{M}$ perpendicular to the scattering vector $\boldsymbol{Q} = \boldsymbol{k}_{\text{i}} - \boldsymbol{k}_{\text{f}}$ contribute to the scattering cross section [112]. These perpendicular components are denoted by $\boldsymbol{M}_\perp = \boldsymbol{Q} \times (\boldsymbol{M} \times \boldsymbol{Q})$. The neutron spin-flip processes can be described by the magnetic interaction operator

$$\boldsymbol{\sigma} \cdot \boldsymbol{M}_\perp = M_{\perp x}\sigma_x + M_{\perp y}\sigma_y + M_{\perp z}\sigma_z, \tag{3.23}$$

with $\boldsymbol{\sigma}$ the Pauli matrices

$$\sigma_x = \begin{pmatrix} 0 & 1 \\ 1 & 0 \end{pmatrix}, \quad \sigma_y = \begin{pmatrix} 0 & -i \\ i & 0 \end{pmatrix}, \quad \text{and} \quad \sigma_z = \begin{pmatrix} 1 & 0 \\ 0 & -1 \end{pmatrix}. \tag{3.24}$$

1-dimensional polarization analysis was introduced by Moon, Riste and Koehler [117] using a polarized triple-axis spectrometer (TAS), which allows one to investigate different spin-dependent cross sections in a magnetic neutron scattering experiment. Fig. 3.4 shows an experimental arrangement. At the sample site, a guide field is set to provide a magnetic field pointing in an arbitrary direction. The incident neutron spins are aligned along the guide field, and the polarization of the scattered neutrons is measured as the projection of the neutron spins on the analyzer. Before and after the sample, the spin

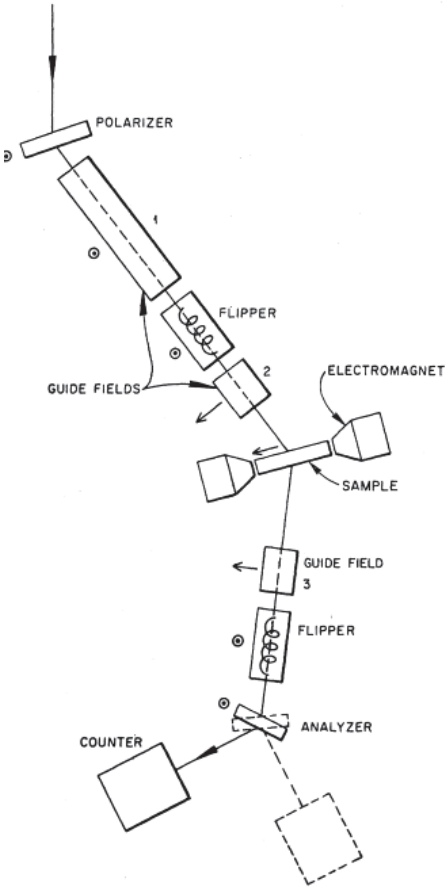

Fig. 3.4: An experimental setup for a polarized TAS. At the sample site, a guide field is generated by a electromagnet to have a freedom to point in an arbitrary direction. Two spin flippers before and after the sample select the desired neutron spin states. Four different scattering channels are illustrated in the text. From [117].

states of neutrons can be changed by two spin flippers, which allows one to select the spin-up ($|+\rangle$) or spin-down ($|-\rangle$) neutron state. In this setup, it is possible to measure the spin-flip channels of $++$, $+-$, $-+$, and $--$ in the magnetic neutron scattering. The matrix elements can be calculated as $\langle i|\boldsymbol{\sigma}\cdot\boldsymbol{M}_{\perp}|f\rangle$, where i and f represent the neu-

tron states in the incident and scattered beam, respectively. The four transition matrix elements are

$$\langle +|\boldsymbol{\sigma}\cdot\boldsymbol{M}_\perp|+\rangle = M_{\perp z}, \tag{3.25}$$

$$\langle -|\boldsymbol{\sigma}\cdot\boldsymbol{M}_\perp|-\rangle = -M_{\perp z}, \tag{3.26}$$

$$\langle -|\boldsymbol{\sigma}\cdot\boldsymbol{M}_\perp|+\rangle = M_{\perp x} + iM_{\perp y}, \tag{3.27}$$

$$\langle +|\boldsymbol{\sigma}\cdot\boldsymbol{M}_\perp|-\rangle = M_{\perp x} - iM_{\perp y}. \tag{3.28}$$

The corresponding scattering cross sections are proportional to $|\langle i|\boldsymbol{\sigma}\cdot\boldsymbol{M}_\perp|f\rangle|^2$, for example in the $-+$ channel

$$|\langle -|\boldsymbol{\sigma}\cdot\boldsymbol{M}_\perp|+\rangle|^2 = (M_{\perp x} + iM_{\perp y})^*(M_{\perp x} + iM_{\perp y}) = M_{\perp x}^2 + M_{\perp y}^2. \tag{3.29}$$

The polarization analysis is the standard technique available to measure the magnetic fluctuations or separate the magnetic scattering from nuclear scattering, for the latter one is always non-spin-flip.

In contrast to conventional polarization analysis, no guide field is applied at the sample site in an NRSE experiment. Now we turn our attention to discuss the spin-flip processes for a magnetic scattering at the sample site, and the influence of these processes on the spin-echo signal. In Fig. 3.5, if we assume that the neutron spin impinging on the sample has a initial phase φ_i with respect to $\boldsymbol{x} \parallel \boldsymbol{Q}$ after passing through the first spin-echo arm. This corresponds to the spinor

$$\boldsymbol{s}_i = \begin{pmatrix} \exp(-i\varphi_i/2) \\ \exp(i\varphi_i/2) \end{pmatrix}, \tag{3.30}$$

with the expectation value of polarization $\boldsymbol{P}_i$ of $\boldsymbol{s}_i$,

$$\boldsymbol{P}_i = \begin{pmatrix} \langle \boldsymbol{s}_i|\sigma_x|\boldsymbol{s}_i\rangle \\ \langle \boldsymbol{s}_i|\sigma_y|\boldsymbol{s}_i\rangle \\ \langle \boldsymbol{s}_i|\sigma_z|\boldsymbol{s}_i\rangle \end{pmatrix} = \begin{pmatrix} \cos\varphi_i \\ \sin\varphi_i \\ 0 \end{pmatrix}. \tag{3.31}$$

In the remainder of this chapter, all components of $\boldsymbol{\sigma}\boldsymbol{M}_\perp$ with "$\perp$" defined in Eq. (3.23) are omitted for simplicity. The components of magnetic scattering by in-plane ($\boldsymbol{M}_y$) and out-of-plane ($\boldsymbol{M}_z$) fluctuations lead to the following final states $\boldsymbol{s}_{f,y}$, $\boldsymbol{s}_{f,z}$, respectively:

$$\boldsymbol{s}_{f,y} = M_y\sigma_y|\boldsymbol{s}_i\rangle = \frac{M_y}{\sqrt{2}}\begin{pmatrix} -i\exp(i\varphi_i/2) \\ i\exp(-i\varphi_i/2) \end{pmatrix}, \tag{3.32}$$

$$\boldsymbol{s}_{f,z} = M_z\sigma_z|\boldsymbol{s}_i\rangle = \frac{M_z}{\sqrt{2}}\begin{pmatrix} \exp(-i\varphi_i/2) \\ \exp(i\varphi_i/2) \end{pmatrix}. \tag{3.33}$$

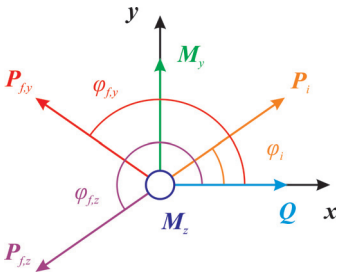

Fig. 3.5: General case of the neutron spinflip processes at the sample site. The polarization $\boldsymbol{P}_i$ of the incident beam are spread within the $\boldsymbol{x} - \boldsymbol{y}$ plane, where $\boldsymbol{x} \parallel \boldsymbol{Q}$ and $\boldsymbol{z}$ is vertical. Only magnetic fluctuations $\boldsymbol{M}_y$ and $\boldsymbol{M}_z$ contribute to the scattering cross section. The $\boldsymbol{P}_i$ with Larmor phase φ_i is flipped to $\boldsymbol{P}_{f,y}$ and $\boldsymbol{P}_{f,z}$ by $\boldsymbol{M}_y$ and $\boldsymbol{M}_z$, respectively.

The corresponding expectation values of the polarization are

$$\boldsymbol{P}_{f,y} = M_y^2 \begin{pmatrix} -\cos\varphi_i \\ \sin\varphi_i \\ 0 \end{pmatrix} \quad \text{and} \quad \boldsymbol{P}_{f,z} = M_z^2 \begin{pmatrix} -\cos\varphi_i \\ -\sin\varphi_i \\ 0 \end{pmatrix}. \tag{3.34}$$

The spin phases after the scattering processes become

$$\varphi_{f,y} = \pi - \varphi_i \quad (\uparrow\uparrow), \tag{3.35}$$

$$\varphi_{f,z} = \pi + \varphi_i \quad (\uparrow\downarrow). \tag{3.36}$$

To fulfill the spin-echo condition, i.e. the recovery of polarization after the second precession region, the fields of the two precession regions must be antiparallel in case of non-spin-flip scattering. Eq. (3.35) shows that the phase $\varphi_{f,y}$ resulting from $\boldsymbol{M}_y$ inverts the sign of φ_i and this fact effectively acts as an inversion of the sign of $\boldsymbol{B}_1$ from the first arm of NRSE-TAS. Thus to fulfill the spin-echo condition, a parallel field configuration ($\uparrow\uparrow$) of $\boldsymbol{B}_1$ and $\boldsymbol{B}_2$ is required. On the other hand in Eq. (3.36), the sign of $\varphi_{f,z}$ resulting from $\boldsymbol{M}_z$ remains the same as φ_i with a constant π adding to the phase, and therefore the spin-echo condition is achieved in the usual anti-parallel field configuration ($\uparrow\downarrow$) setting. The π phase shifts have no practical meaning in most experiments and can be compensated for. However, they play a key role in a ray-tracing modeling, as explained in the following section. To summarize, one should apply the $\uparrow\uparrow$ ($\uparrow\downarrow$) magnetic field configuration for the in-plane (out-of-plane) fluctuations in a NSE measurement.

3.4.3 Modeling based on a ray-tracing simulation

For large spin-echo time τ_{NSE}, only the scattering process fulfilling the spin-echo condition [see Eq. (4.4)] contributes to the echo signal, the other mentioned spins are depolarized and lead to an unpolarized background. For small τ_{NSE} in the case of DC coils, all scattering processes contribute to the signal, which then shows a strong oscillation instead of the simple exponential decay of $\mathrm{P}(\tau_{\mathrm{NSE}})$ observed in conventional spin-echo experiments. To model the polarization, we use here a simple ray-tracing model, which traces the spin of individual neutrons in the precession regions and takes the corresponding scattering process into account. By assumption, the applied current in the first spin-echo arm I01 is kept positive ($\uparrow$), while positive or negative sign of the applied current I02 in the second arm can be considered as the parallel ($\uparrow\uparrow$) or antiparallel ($\uparrow\downarrow$) magnetic field configurations. In a quasi-elastic scattering, each neutron is defined by the wave vector $\boldsymbol{k}$, the polarization vector $\boldsymbol{P}$, and a probability p. p is the probability that a neutron exists in the assigned state. In addition, several parameters like $\boldsymbol{k}_{\mathrm{i}}$, the resolution function $R(\omega)$ [118], or energy transfer ω, are assumed to follow a Gaussian or Lorentzian distribution. Convenient coordinates $(\boldsymbol{x}, \boldsymbol{y}, \boldsymbol{z})$ of this model are chosen as (1) $\boldsymbol{x} \parallel \boldsymbol{k}_{\mathrm{i}}$ in the incident beam, (2) $\boldsymbol{x} \parallel \boldsymbol{Q}$ at the sample site, and (3) $\boldsymbol{x} \parallel \boldsymbol{k}_{\mathrm{f}}$ in the scattered beam. The scattering plane is spanned by vectors $\boldsymbol{x}$ and $\boldsymbol{y}$, with z pointing upwards.

The neutron spin polarization is calculated in the following steps.

- I. In the incident beam ($\boldsymbol{x} \parallel \boldsymbol{k}_{\mathrm{i}}$), neutrons are selected with a uniform distribution on the magnitude of wave vector k_{i} and we assume the initial polarization $\boldsymbol{P_i} \perp \boldsymbol{k}_{\mathrm{i}}$. The Larmor phases $\phi_{\mathrm{i}}(k_{\mathrm{i}}, \mathrm{I01})$ of the neutrons propagating through the first spin-echo arm are calculated. The probability p_{i} of the neutrons is given by a Gaussian distribution of k_{i} with FWHM Δk_{i}, which can be estimated from a Cooper-Nathans model of the monochromator [119]. Typically, $\Delta k_{\mathrm{i}} = 0.04\,\text{Å}^{-1}$ for $k_{\mathrm{i}} = 2.51\,\text{Å}^{-1}$ at TRISP.

- II. For different scattering processes (consisting of in-plane M_1 and out-of-plane M_2 fluctuations, indexed by 1 and 2), we transform ϕ_{i} into the sample coordinate ($\boldsymbol{x} \parallel \boldsymbol{Q}$) as ϕ_{si}. Energy transfers $\omega_{1,2}$ are assigned to different scattering channels arising from M_1 and M_2. The magnitude of the scattered wave vectors (k_{f1} and k_{f2}) and the corresponding shift in Larmor phases (ϕ_{sf1} and ϕ_{sf2}) in accordance with Eq. (3.35) and (3.36) are calculated. We assume the scattering function $S(\boldsymbol{Q}, \omega)$ to be independent of $\boldsymbol{Q}$ within the small momentum range defined by the TAS resolution ellipsoid $R(\boldsymbol{Q}, \omega)$. The probability function of the scattering process $p_{\omega_{1,2}}$ is then expressed as

$$p_{\omega_{1,2}} = S_{1,2}(\omega_{1,2}, \Gamma_{1,2}) \cdot R(\omega) \cdot \mathrm{I}_{1,2}. \tag{3.37}$$

  The resolution function of the TAS, $R(\omega)$, is modeled as a Gaussian , and the

FWHM is taken as the *Vanadium width* determined experimentally. $I_{1,2}$ is proportional to the integrated intensities scattered by $M_{1,2}$ with $I_1 + I_2 = 1$. $S_{1,2}(\omega_{1,2}, \Gamma_{1,2})$ is modeled as a Lorentzian. The total scattering function thus reads

$$S(\omega_{1,2}, \Gamma_{1,2}) = I_1 \times \frac{\Gamma_1}{\omega_1^2 + \Gamma_1^2} + I_2 \times \frac{\Gamma_2}{\omega_2^2 + \Gamma_2^2} \tag{3.38}$$

In the energy band $d\omega$, the probability for a energy transfer is $S_{1,2}(\omega_{1,2}, \Gamma_{1,2})\, d\omega$ and is normalized to 1 via

$$\int S(\omega_{1,2}, \Gamma_{1,2})\, d\omega_{1,2} = 1. \tag{3.39}$$

The selection of $\omega_{1,2}$ was made in a reasonable band $\Delta\omega_{1,2} = \pm 10\,\Gamma_{1,2}$ to avoid cutting of the Lorentzian wings. Moreover, if Γ_1 and Γ_2 are different, the probability $p_{\omega 1,2}$ has to be normalized to the ω band as $p_{\omega 1,2} \cdot \Delta\omega$.

- III. After transforming ϕ_{sf1} and ϕ_{sf2} to the scattered beam coordinate ($\boldsymbol{x} \parallel \boldsymbol{k}_f$), we add precession phases $\phi_{f1,2}(\omega_{1,2}, k_{f1,2})$ in the second spin-echo arm, which is driven by a I02. The magnitude of the polarization vector $\boldsymbol{P}$ after the second precession region is

$$\mathbb{P} = |\boldsymbol{P}| = \left|\frac{\sum p_i \cdot p_{\omega_{1,2}} \cdot (cos\phi_{f1,2}, sin\phi_{f1,2})}{\sum p_i \cdot p_{\omega_{1,2}}}\right|. \tag{3.40}$$

One should note that the polarization is the ensemble average over the spin states in a neutron beam with $P = (N_\uparrow - N_\downarrow)/(N_\uparrow + N_\downarrow)$, where $N_\uparrow$ ($N_\downarrow$) is the number of neutrons with spin up (down).

- IV. The model was implemented as a MATLAB function and calculates the polarization as

$$P = P_0 \times \mathbb{P}(\tau_{NSE}, k_i, \Delta k_i, \Gamma_1, \Gamma_2, I_1). \tag{3.41}$$

For quasielastic scattering, I01 = |I02| is kept fixed to ensure the spin-echo condition. τ_{NSE} can be derived from I0 by Eq. (3.22). P_0 is the spin-echo resolution function, including instrumental effects resulting from the beam divergence and from small field inhomogeneities in the *NRSE* and *DC* modes. This can be determined experimentally by measuring the polarization of the unscattered beam or of a nuclear Bragg reflection.

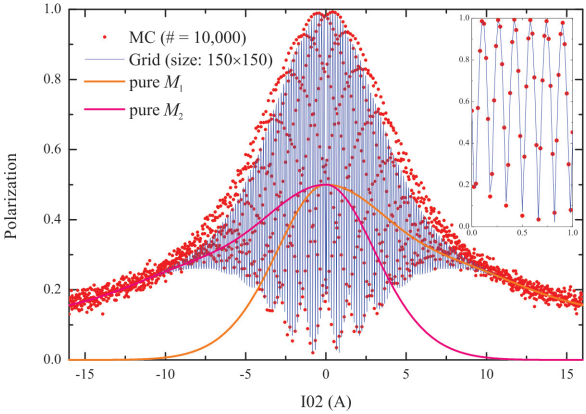

Fig. 3.6: Calculations of $\mathbb{P}$ from the MC and Grid methods in the *isotropic* case using k_i = 2.51 Å^{-1}, Δk_i = 0.04 Å^{-1}, $\Gamma_1 = \Gamma_2$ = 100 μeV, and $I_1 = I_2$ = 0.5. The resolution function $R(\omega)$ is neglected for simplicity. The inset shows the oscillating behavior of the polarization arising from the interference between M_1 and M_2.

3.4.4 Numerical calculations and discussion

In practice, there are several ways to generate the above-mentioned $\mathbb{P}$ to analyze the spin-echo data. Considering the step I. in Sec. 3.4.3, the generation of neutrons can be made (1) by creating random numbers as in the Monte Carlo (MC) technique, or more efficiently, (2) on equally spaced grids. The former offers easier and transparent insight, while the latter is faster and more efficient.

Fig. 3.6 shows two different numerical results of $\mathbb{P}$ from the MC and grid methods for comparison, in calculating the polarization as a function of the applied current I02 with I01 = |I02|. By neglecting the instrumental effect $R(\omega)$, the parameters k_i = 2.51 Å^{-1}, Δk_i = 0.04 Å^{-1}, $\Gamma_1 = \Gamma_2$ = 100 μeV, and $I_1 = I_2$ = 0.5 are used in both calculations. One should bear in mind that these calculations are actually in the *isotropic* case, where the integrated intensities resulting from both fluctuations are identical. In the MC method, N = 10000 neutrons are used to repeat the previous steps I to III, this means that k_i and ω are generated as random numbers. In the Grid method, a uniform grid of size 150 is assigned to generate the neutrons with a Gaussian distribution of k_i and ω, hence the resulting calculation is based on a two-dimensional matrix with a size of 150 × 150. As seen in Fig. 3.6, theses two results are in good agreement with each other. By using the MC formalism within a fitting routine (MINUIT) [120], however, it turns out that the statistical noise tends to disturb the minimization algorithm unless a very high number of neutrons is used in the simulation. On the other hand, the Grid formalism avoids

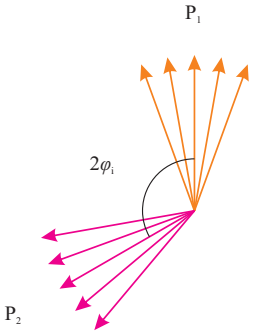

Fig. 3.7: A simple diagram of different polarizations P_1 and P_2 (arising from M_1 and M_2) with a phase difference $2\varphi_i$. This reveals the oscillating nature of polarization found in Fig. 3.6.

the statistical noise introduced by random numbers. We thus used the latter one in the following data analysis for MnF_2 and Rb_2MnF_4.

An important feature observed in Fig. 3.6 is the oscillating behavior of the polarization. This fact can be explained as a consequence of the different spin-flip processes, as shown in Fig. 3.5. The ↑↑ (↑↓) magnetic field configuration has to be applied to obtain the spin-echo of the in-plane M_y (out-of-plane M_z) fluctuations. However, there is also a further non-negligible contribution from M_z (M_y), especially in the small I02 (or small τ_{NSE}) region. That is to say, the number of Larmor precessions is not sufficient to depolarize the contributions, which do not contribute to the echo signal. Clearly, the calculations in Fig. 3.6 are in this limit. M_1 (M_2) are the in-plane (out-of-plane) magnetic fluctuation, and the positive (negative) abscissa of I02 in Fig. 3.6 represents the ↑↑ (↑↓) field configuration. The non-echo contributions of M_1 and M_2 are found in the current range of $-10\,\mathrm{A} < \mathrm{I02} < 0\,\mathrm{A}$ and $0\,\mathrm{A} < \mathrm{I02} < 10\,\mathrm{A}$, respectively. At currents > 10 A, these non-echo components are depolarized and the oscillation disappears. The polarization decays exponentially corresponding to the assigned linewidth of $\Gamma = 100\,\mu\mathrm{eV}$. Therefore, the interference behavior found for $|\mathrm{I02}| < 10\,\mathrm{A}$ causes a failure in the normal treatment of NSE data.

In fact, the complicated behavior of M_1 and M_2 can be illustrated by a simple diagram shown in Fig. 3.7. As discussed in Sec. 3.4.3, there exists a net phase difference $2\varphi_i$ between the in-plane M_1 and out-of-plane M_2 from different scattering processes, which can be deduced from Eq. (3.35) and (3.36). Accordingly, this leads to an effective phase offset $2\varphi_i$ between P_1 and P_2. The resulting polarization is bouncing up and down within a boundary between $|P_1 + P_2|$ and $|P_1 - P_2|$, because φ_i is a function of I02. The ratio of the maximum in P_1 to P_2 at $\mathrm{I02} = 0$ indicates the ratio of the integrated intensities I_1/I_2. In addition, the observed oscillatory period T is thus expected to be

related to the average of $\cos(2\varphi_\mathrm{i})$. More specifically, it gives

$$\langle \cos(2\varphi_i) \rangle = \langle \cos\left(\frac{4\pi C_c}{k_\mathrm{i}} \cdot \mathrm{I01}\right) \rangle = \langle \cos\left(\frac{2\pi}{\mathrm{T}} \cdot \mathrm{I01}\right) \rangle. \tag{3.42}$$

It indicates that $\mathrm{T} = k_\mathrm{i}/(2C_c)$, which depends only on the assigned k_i and the intrinsic spin-echo coil parameter C_c. As a result, T can be estimated to be 0.1483 A, which is in good agreement with our calculations shown in Fig. 3.6.

In summary, in this thesis a model was developed to describe spin-echo data resulting from magnetic scattering with different spin-flip processes, which only partially fulfill the spin-echo condition. This model is especially important for the range of small τ_NSE, which is crucial in the case of relatively large linewidth $\Gamma > 100\,\mu$eV. The new model can be applied to all spin-echo experiments on spin excitations. An efficient implementation in MATLAB allows direct application in standard fitting functions.

4 Experiment

4.1 Crystal and magnetic structures of MnF_2 and Rb_2MnF_4

4.1.1 3D AFM MnF_2

MnF_2 is a textbook example of a classical $S = 5/2$ antiferromagnetic insulator. It crystallizes in the tetragonal rutile structure with space group $P4_2/mnm$ and lattice constants $a = 4.874$ Å, $c = 3.300$ Å [121]. Fig. 4.1 (a) shows the nuclear and magnetic structures of MnF_2. The magnetic Mn^{2+} ion has half-filled $3d^5$ electronic configuration, leading to a high spin state with $S = 5/2$. The main magnetic interactions result from the direct ferromagnetic exchange J_1 between the nearest-neighbor $S = 5/2$ Mn^{2+} ions along the $[001]$ axis and the antiferromagnetic superexchange coupling J_2 between the eight next-nearest neighbors of the Mn^{2+} ions along the $[111]$ axis. $J_2 = -1.76$ K is by a factor of 5.5 larger than J_1 [122]. The the Mn^{2+} ions have no orbital components ($L = 0$). A uniaxial anisotropiy in MnF_2 is predominantly due to dipole-dipole interactions. This causes the spins to align along the tetragonal c-axis. The spin Hamiltonian of MnF_2 is given by

$$H = -\frac{1}{2}J_1 \sum_{i,j} \cdot \boldsymbol{S}_i \boldsymbol{S}_j - \frac{1}{2}J_2 \sum_{i,k} \boldsymbol{S}_i \cdot \boldsymbol{S}_k - D_A \sum_i (S_i^z)^2. \tag{4.1}$$

The summation runs over all magnetic ions i, their nearest neighbors j, and their next-nearest neighbors k. The anisotropy term is expressed as $H_A = -D_A \sum_i (S_i^z)^2$, which explains the preferred spin alignment below the critical temperature. This magnitude of the anisotropy was calculated by Keffer [123] and later verified experimentally by Johnson *et al.* in an antiferromagnetic resonance measurement [88]. As a result, they confirmed that the anisotropy is mainly originating from the dipole-dipole interaction of Mn^{2+} and the reduced anisotropy is $\alpha_1 = 1.6 \times 10^{-2}$.

4.1.2 2D AFM Rb_2MnF_4

Rb_2MnF_4 belongs to the tetragonal K_2NiF_4-type structure with space group $I4/mmm$ and lattice parameters $a = 4.230$ Å, $c = 13.82$ Å [124]. As shown in Fig. 4.1 (b), the square-lattice MnF_2 planes are separated by two sheets containing non-magnetic ions.

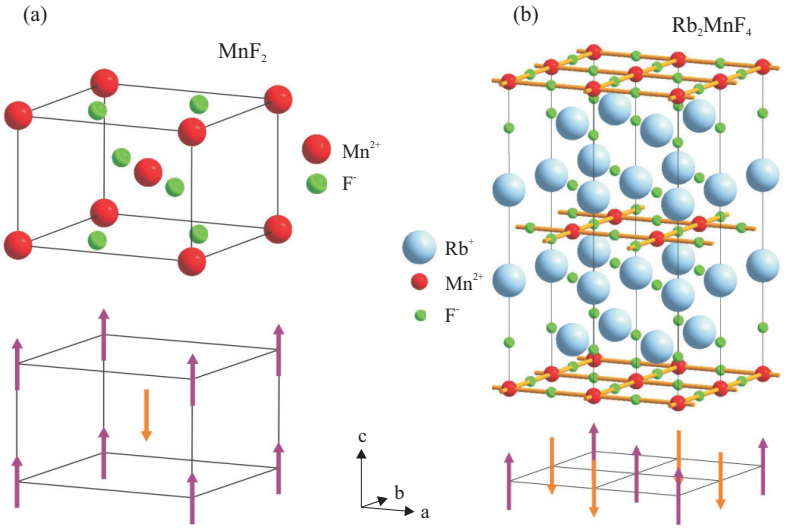

Fig. 4.1: Nuclear (top) and magnetic (bottom) structures of (a) MnF_2 and (b) Rb_2MnF_4. Rb_2MnF_4 forms a 2D spin structure due to the relatively small interplane magnetic interaction J'. In the ordered state, the spins in both compounds are aligned along the tetragonal c-axis.

This leads to a c much larger than a. The dominant magnetic interaction is the antiferromagnetic superexchange coupling J between the $S = 5/2$ spins of the Mn^{2+} ions, between the four nearest neighbors in the (MnF_2) ab-plane in Rb_2MnF_4. The interplane magnetic interaction J' is much smaller than J, roughly by a factor of 10^{-6}. Thus the spin coupling has a 2D nature [125]. Due to the existence of magnetic Mn^{2+} ions, the single-ion anisotropy arising from dipole-dipole interaction causes the spins to align uniaxially along the c-axis. It can be described by a spin Hamiltonian without interplane coupling

$$H = J_{nn} \sum_{i,j} \boldsymbol{S}_i \cdot \boldsymbol{S}_j + \sum_i g_i \mu_B H_i^A S_i^z. \tag{4.2}$$

J_{nn} is the coupling for the nearest neighbors of spins in the MnF_2 plane. The staggered anisotropic field H_i^A denotes the effect of dipolar anisotropy. $J_{nn} = 7.36\,\mathrm{K}$ was obtained, for example, by NMR studies on the sublattice magnetization [126] and by neutron scattering measurements of the spin-wave dispersion [96, 127, 128]. The re-

duced anisotropy is

$$\alpha_{\mathrm{I}} = g\mu_B H^A \Big/ \sum_{j=nn} J_{nn} S_j \simeq 4.7 \times 10^{-3}. \tag{4.3}$$

It is worth noting that in an early neutron diffraction experiment carried out by Birgeneau *et al.* [19], two phases in Rb_2MnF_4 were observed. These consist of K_2NiF_4 and Ca_2MnO_4 structures with a ferromagnetic and an antiferromagnetic stacking arrangements of the MnF_2 sheets. These two phases were reported to have the same critical temperature within the experimental errors and follow the same critical behavior with an exponent β closer to the 2D Ising scaling.

Concerning the small α_{I}, MnF_2 and Rb_2MnF_4 are considered as weakly anisotropic Heisenberg antiferromagnets with 3D and 2D spin arrangements, respectively. In MnF_2, pure magnetic Bragg reflections occur at reciprocal lattice points H + L = odd in the (H0L) plane. In this plane, all Bragg reflections are either pure nuclear or pure magnetic. In Rb_2MnF_4, pure magnetic Bragg reflections occur for half-integer H and K in the (HK0) plane.

4.2 Neutron scattering experiments

4.2.1 Sample alignment

Large single crystals of MnF_2 (Rb_2MnF_4) with a volume of 10 cm^3 (3 cm^3) and mosaic spread of $0.44'$ ($0.99'$) were available from a previous experiment [129]. The mosaic spreads were measured by γ-diffractometry at room temperature using (200) reflections. The crystals were mounted on the goniometers in the (H0L) plane for MnF_2 and the (HK0) plane for Rb_2MnF_4, as shown in Fig. 4.2 (a) and (b).

Prior to the NSE investigations, experiments using the neutron Laue camera at the FRM II were performed to check the crystal's orientation and quality at room temperature. Neutron Laue diffraction probes the bulk of a crystal in contrast to X-rays, which only see the surface. Fig. 4.2 (c) and (d) show the patterns from neutron Laue camera of the MnF_2 crystal along the [001] and [100] directions, respectively. In both patterns, strong nuclear Bragg reflections were observed so as to confirm that the crystal is single-domain.

The spin-echo experiments were conducted at the NRSE-TAS spectrometer TRISP at the FRM II [115]. TRISP was operated with a graphite PG (002) monochromator and a Heusler (111) analyzer, with open collimation and scattering senses SM = −1, SS = −1, SA = 1 at the monochromator, sample, and analyzer, respectively (−1 is clockwise). The crystals were mounted in a closed cycle cryostat in exchange ^{4}He gas.

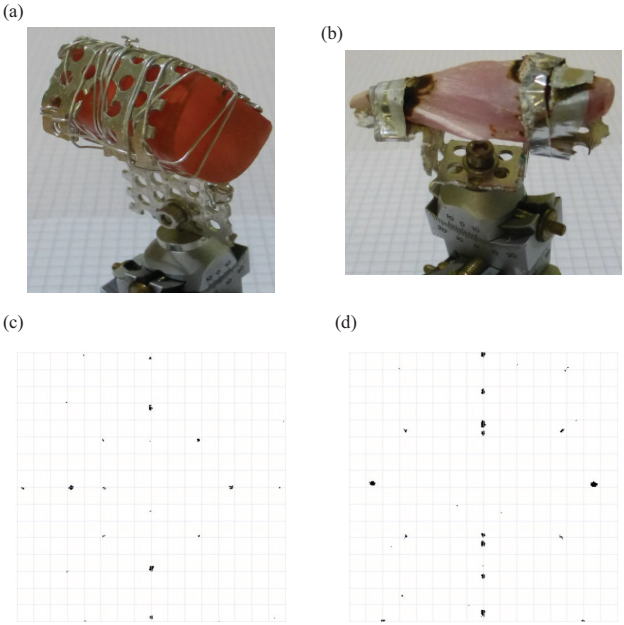

Fig. 4.2: Photographs of the (a) MnF_2 and (b) Rb_2MnF_4 single crystals. Both crystals were mounted on the goniometers. Neutron Laue patterns of the MnF_2 crystal, which were taken in backscattering configuration along the (c) $[001]$ and (d) $[100]$ directions.

The data were collected at reciprocal lattice points corresponding to magnetic Bragg reflections. For the experiment on MnF_2 at $\boldsymbol{Q} = (300)$, we used an incident wave number $k_\mathrm{i} = 2.35\,\text{Å}^{-1}$ with a TAS energy resolution $V = 0.8\,\mathrm{meV}$ (*vanadium width*, full width at half maximum, FWHM). For Rb_2MnF_4, k_i was set to $2.51\,\text{Å}^{-1}$ at $\boldsymbol{Q} = (0.5\,0.5\,0)$ with $V = 1.1\,\mathrm{meV}$. For the crystal alignment, we used TRISP in TAS mode with spin-echo coils switched off. Fig. 4.3 shows the rocking scans of MnF_2 and Rb_2MnF_4 at $\boldsymbol{Q} = (300)$ and $\boldsymbol{Q} = (0.5\,0.5\,0)$, respectively. The widths are 0.3° and 0.4°, which corresponds to the intrinsic TAS resolution of the instrument.

4.2.2 Antiferromagnetic order parameter

Fig. 4.4 (a) and (b) show the temperature dependence of intensities of the antiferromagnetic Bragg peaks (300) in MnF_2 and $(0.5\,0.5\,0)$ in Rb_2MnF_4. Such temperature

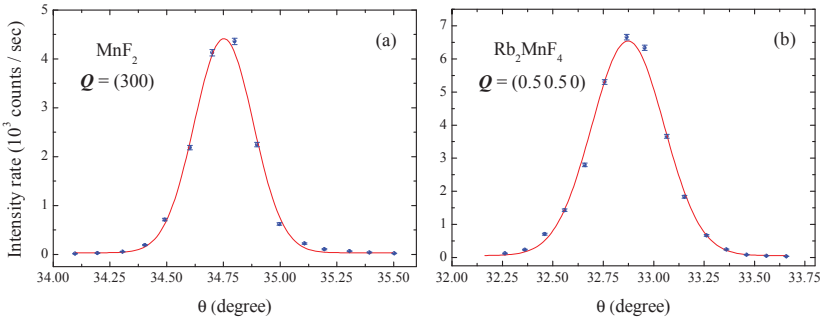

Fig. 4.3: Rocking scans of the magnetic Bragg peaks in (a) MnF_2 and (b) Rb_2MnF_4 below T_N. The solid lines are from Gaussian fits.

scans with sweep rates of the order of 0.05 K/min where taken at the beginning of each experiment at TRISP. Thus consistent thermometry is ensured. In Fig. 4.4 (a), $T_N = 67.29$ K of MnF_2 was determined from the maximum slope of the intensity I of the magnetic (300) Bragg reflection [130]. For Rb_2MnF_4, the sharp peak of I *vs.* T in Fig. 4.4 (b) results from the longitudinal critical scattering [131] and thus defines $T_N = 37.6$ K. As a result, the observed Néel temperatures are close to values in the literature [8, 13, 14, 17, 41].

4.3 Magnetic scattering processes

Quasielastic experiments on classical antiferromagnets MnF_2 and Rb_2MnF_4 were conducted at the $\boldsymbol{Q} = (300)$ and $(0.5\,0.5\,0)$ magnetic Bragg reflections, respectively. In both materials, the sublattice magnetization $\boldsymbol{M}$ below T_N is uniaxial along the crystallographic c axis. The magnetic fluctuations parallel to $\boldsymbol{M}$ are defined as the longitudinal fluctuations $\boldsymbol{M}_\parallel$ and the others perpendicular to $\boldsymbol{M}$ are the transverse fluctuations $\boldsymbol{M}_\perp$. In magnetic neutron scattering, only magnetic fluctuations $\boldsymbol{M} \perp \boldsymbol{Q}$ are visible by neutrons and thus contribute to the magnetic cross section.

The relation between the coordinates xyz and the longitudinal and transverse spin fluctuations $\boldsymbol{M}_\parallel$ and $\boldsymbol{M}_\perp$ is shown in Fig. 4.5. In Fig. 4.5 (a), the MnF_2 crystal was mounted in the (HK0) plane, indicating that the $\boldsymbol{M}_\parallel$ lies in the scattering plane and the visible $\boldsymbol{M}_\perp$ is out of the ac-plane and perpendicular to c. In Fig. 4.5 (b), the Rb_2MnF_4 crystal was aligned in the (HK0) plane. This leads to the visible $\boldsymbol{M}_\perp$ along $\boldsymbol{y}$ and the $\boldsymbol{M}_\parallel$ perpendicular to the ac-plane. Fig. 4.5 (c) and (d) show the spin-flip processes for

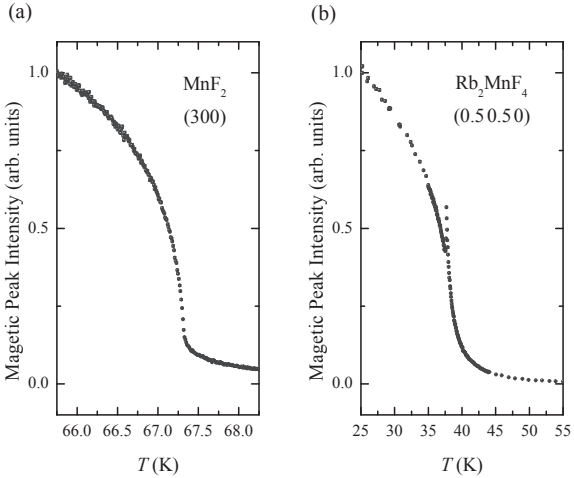

Fig. 4.4: Antiferromagnetic order parameters. (a) Intensity of the antiferromagnetic Bragg peak (300) in MnF_2 as a function of temperature. The maximum slope defines the Néel temperature T_N. (b) Intensity of the $(0.5\,0.5\,0)$ magnetic Bragg reflection of Rb_2MnF_4. The sharp peak results from critical scattering and defines T_N.

MnF_2 and Rb_2MnF_4. For both materials, the initial $\boldsymbol{P}_i$ undergoes spin flips around the respective component of $\boldsymbol{M}$, such that $\boldsymbol{M}_\parallel$ flips $\boldsymbol{P}_i$ to $\boldsymbol{P}_{f,\parallel}$ and $\boldsymbol{M}_\perp$ flips $\boldsymbol{P}_i$ to $\boldsymbol{P}_{f,\perp}$. In summary, the corresponding spin flips and the appropriate field configurations that follow the spin-echo condition are

$$\mathrm{MnF_2}: \begin{cases} \varphi_{f,\parallel} = \pi - \varphi_i & (\uparrow\uparrow) \\ \varphi_{f,\perp} = \pi + \varphi_i & (\uparrow\downarrow) \end{cases} \qquad \mathrm{Rb_2MnF_4}: \begin{cases} \varphi_{f,\parallel} = \pi + \varphi_i & (\uparrow\downarrow) \\ \varphi_{f,\perp} = 3\pi/2 - \varphi_i & (\uparrow\uparrow) \end{cases} \tag{4.4}$$

The spin-echo condition is fulfilled if the Larmor phase of the first spin-echo arm is inverted in the second one. Note that for $\varphi_{f,\parallel}$ in MnF_2 and $\varphi_{f,\perp}$ in Rb_2MnF_4, the minus sign of the scattered spin phases corresponds to an effective sign inversion of the magnetic field applied in the first spin-echo arm. Hence, the magnetic fields in these two cases have to be chosen parallel $(\uparrow\uparrow)$ to fulfill the echo condition. On the other hand, the spin flips of $\varphi_{f,\perp}$ in MnF_2 and of $\varphi_{f,\parallel}$ in Rb_2MnF_4 don't change the sign of φ_i. The echo condition is fulfilled if the magnetic fields are antiparallel $(\uparrow\downarrow)$. The neutron spins scattered by the component of $\boldsymbol{M}$ not fulfilling the echo conditions effectively precess with the same sign in both spin-echo arms. They are depolarized if their phase

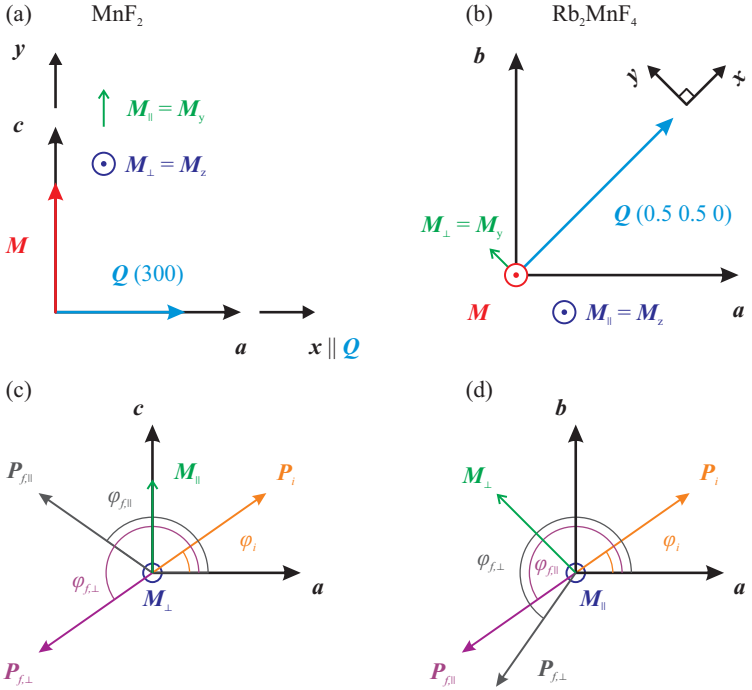

Fig. 4.5: Top panel: spin fluctuations parallel and perpendicular to the sublattice magnetization $\boldsymbol{M}$ are referred to as longitudinal (labeled $\parallel$) and transverse (labeled $\perp$). In both MnF_2 and Rb_2MnF_4, $\boldsymbol{M}$ is parallel to the tetragonal c-axis. (a) In MnF_2, the ac-plane was aligned in the scattering plane, thus the $\boldsymbol{M}_\parallel$ are along $\boldsymbol{y}$, and the $\boldsymbol{M}_\perp$ along $\boldsymbol{z}$. (b) Rb_2MnF_4 was aligned in the ab-plane with $\boldsymbol{M}_\parallel$ along $\boldsymbol{z}$ and $\boldsymbol{M}_\perp$ along $\boldsymbol{y}$. Bottom panel: Spin flip processes at (c) MnF_2 and (d) Rb_2MnF_4. The initial polarization $\boldsymbol{P}_\mathrm{i}$ is flipped to $\boldsymbol{P}_{f,\parallel}$ and $\boldsymbol{P}_{f,\perp}$ resulting from $\boldsymbol{M}_\parallel$ and $\boldsymbol{M}_\perp$, respectively.

is spread by more than 2π at the exit of the second region.

4.4 TAS resolution function

In TAS, the monochromator selects a small band of the incident neutron wave vectors $\boldsymbol{k}_\mathrm{i}$ with an averaged value $\boldsymbol{k}_\mathrm{I}$. The analyzer in the scattered beam selects a band of $\boldsymbol{k}_\mathrm{f}$ with mean $\boldsymbol{k}_\mathrm{F}$. As a consequence the momentum and energy transfers of the neutrons are distributed around the average value $(\boldsymbol{Q}_0, \omega_0)$, where $\boldsymbol{Q}_0 = \boldsymbol{k}_\mathrm{I} - \boldsymbol{k}_\mathrm{F}$ and $\omega_0 = \hbar^2(\boldsymbol{k}_\mathrm{I}^2 - \boldsymbol{k}_\mathrm{F}^2)/2m_n$. The TAS resolution function $R(\boldsymbol{Q}, \omega)$ defines the probability of detecting a scattering process at $(\boldsymbol{Q}, \omega)$ with the instrumental setting $(\boldsymbol{Q}_0, \omega_0)$. $R(\boldsymbol{Q}, \omega)$ is a 4-dimensional Gaussian distribution [119]

$$R(\boldsymbol{Q}, \omega) = R_0 \exp\left[-\frac{1}{2}\sum_{i=1}^{4}\sum_{j=1}^{4} M_{ij} x_i x_j\right], \tag{4.5}$$

with R_0 a constant, $(x_1, x_2, x_3) = \boldsymbol{Q} - \boldsymbol{Q}_0$ measured in $\mathrm{Å}^{-1}$, and $x_4 = \omega - \omega_0 = \Delta E$ measured in meV. M is the TAS resolution matrix.

The momentum resolution is usually given by three components, the longitudinal resolution $\Delta\boldsymbol{Q}_\parallel \parallel \boldsymbol{Q}_0$, the transverse $\Delta\boldsymbol{Q}_\perp \perp \boldsymbol{Q}_0$ within the scattering plane, and the out-of-plane $\Delta\boldsymbol{Q}_z$. If the instrumental configurations are known, M can be calculated by Cooper's method [119], or more advanced by Popovici's method that includes spatial effects [132]. We use the RESCAL program implemented in MATLAB [133] to calculate the resolution matrix using these methods. The calculated results of the resolution matrix M for MnF_2 and Rb_2MnF_4 are shown below by using Popovici's method. Instead of labeling the components of $\boldsymbol{Q}$ by (x_1, x_2, x_3), often the coordinate labels (x, y, z) are used, where $x \parallel \boldsymbol{Q}_0$, $y \perp \boldsymbol{Q}_0$ in the scattering plane, and $z \perp \boldsymbol{Q}_0$ perpendicular to the scattering plane.

For MnF_2 with $k_\mathrm{I} = k_\mathrm{F} = 2.35\,\mathrm{Å}^{-1}$ and $\boldsymbol{Q} = (300)$, the resolution matrix at TRISP is

$$M = 10^4 \times \begin{pmatrix} 0.3715 & -0.5814 & 0 & -0.0357 \\ -0.5814 & 1.4227 & 0 & 0.0949 \\ 0 & 0 & 0.1214 & 0 \\ -0.0357 & 0.0949 & 0 & 0.0072 \end{pmatrix}. \tag{4.6}$$

This matrix defines an ellipsoid in the 4-dimensional x_i space. Typically, the cross sections in $\boldsymbol{Q}$ of this ellipsoid are given as Bragg widths. This is the width of a scan across a Bragg peak in the given direction. For MnF_2, the Bragg widths are $Q_\mathrm{x} = 0.039\,\mathrm{Å}^{-1}$, $Q_\mathrm{y} = 0.020\,\mathrm{Å}^{-1}$, $Q_\mathrm{z} = 0.068\,\mathrm{Å}^{-1}$. The projection of the ellipsoid on a plane containing the energy axis (x_4) gives the *Vanadium width* $V = 0.816\,\mathrm{meV}$.

For Rb_2MnF_4, the resolution matrix for $k_\mathrm{I} = k_\mathrm{F} = 2.51\,\mathrm{Å}^{-1}$ and $\boldsymbol{Q} = (0.5\,0.5\,0)$ is

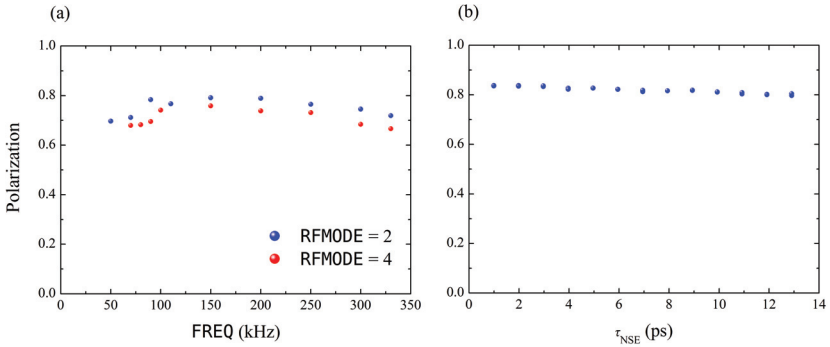

Fig. 4.6: (a) Direct beam calibration for $k = 2.3\,\text{Å}^{-1}$ in the *NRSE* mode. (b) Coil calibration in the *DC* mode at $k = 2\,\text{Å}^{-1}$. The above results were used to normalized the spin-echo raw data.

obtained

$$M = 10^5 \times \begin{pmatrix} 0.0823 & -0.1519 & 0 & -0.0170 \\ -0.1519 & 1.1476 & 0 & 0.1155 \\ 0 & 0 & 0.0110 & 0 \\ -0.0170 & 0.1155 & 0 & 0.0117 \end{pmatrix}. \tag{4.7}$$

This yields the Bragg widths: $Q_x = 0.026\,\text{Å}^{-1}$, $Q_y = 0.007\,\text{Å}^{-1}$, $Q_z = 0.071\,\text{Å}^{-1}$ and $V = 1.091$ meV.

4.5 Analysis of the NRSE data

4.5.1 Effect of coil inhomogeneities

In the procedure of data correction, instrumental effects from small field inhomogeneities in the RF and DC coils have to be taken into account. This contribution can be experimentally determined by performing a so-called direct beam calibration or by measuring the polarization of a nuclear Bragg reflection of a standard material, such as PG (002).

Fig. 4.6 (a) shows the results of direct beam calibration for $k = 2.3\,\text{Å}^{-1}$ in the *NRSE* mode, consisting of experimental data from `RFMODE` = 2 and `RFMODE` = 4 (see Sec. 3.3). The polarization is rather smooth as a function of frequency `FREQ`. The slight drop of the polarization observed at the minimum `FREQ` in both modes is a property of the

RF spin-flipper related to the Bloch-Siegert shift known from NMR [134]. Fig. 4.6 (b) shows the coil calibration in the *DC* mode in measuring the polarization of a PG (002) at $k = 2\,\text{Å}^{-1}$. A fit of this curve using Eq. (3.12) with $\hbar = 658\,\mu\text{eV}\cdot\text{ps}$ gives

$$\text{P} = 0.84126 \cdot \exp(-\frac{2.5271 \cdot \tau_{\text{NSE}}}{\hbar}). \tag{4.8}$$

We obtain the non-intrinsic linewidth broadening $\Gamma_0 = 2.5271\,\mu\text{eV}$. Practically, the raw NSE data are normalized by the calibrated P for the *NRSE* and *DC* modes such that $\text{P}(\tau_{\text{NSE}} = 0) = 1$. In this way, it allows us to extract the intrinsic linewidth of a system.

4.5.2 Finite momentum resolution effect

Here we discuss how the finite momentum resolution defined by the TAS resolution ellipsoid $R(\boldsymbol{Q}, \omega)$ affects the spin-echo resolution. The data of the present experiments were taken at magnetic Bragg reflections $\boldsymbol{G}$, where $\boldsymbol{q} = \boldsymbol{G} - \boldsymbol{Q}$ and $S(\boldsymbol{q}, \omega)$ vary within the 4-dimensional region defined by $(x_1, x_2, x_3, x_4) = (\boldsymbol{q} - \boldsymbol{q}_0, \omega - \omega_0)$, as discussed in Sec. 4.4. To estimate the effect on the linewidth measured by spin-echo, we calculated the polarization by

$$\text{P}(\tau_{\text{NSE}}) = \text{P}_0 \times \int S(\boldsymbol{Q}, \omega) R(\boldsymbol{Q}, \omega) \cos(\omega \tau_{\text{NSE}}) d\omega, \tag{4.9}$$

where the $R(\boldsymbol{Q}, \omega)$ was calculated with matrix elements $M_{i,j}$ corresponding to the spectrometer configurations [119]. The scattering functions $S(q, \omega)$ are taken from previous work in MnF_2 [13] and Rb_2MnF_4 [8, 41].

For the 3D spin system of MnF_2, q is defined as $q = \sqrt{x_1^2 + x_2^2 + c^2/a^2 \cdot x_3^2}$ due to the tetragonal structure. We use the following expressions to calculate the resolution effect. The scattering function can be expressed as

$$S(q, \omega) = \frac{1}{\pi} \frac{1}{q^2 + \kappa^2} \frac{\Gamma_\Delta}{\Gamma_\Delta^2 + x_4^2}. \tag{4.10}$$

κ is the inverse correlation length above T_{N}, which reads $\kappa(T) = 0.032(T - T_{\text{N}})^{0.634}\,\text{Å}^{-1}$. The linewidth difference is

$$\Gamma_\Delta = \Gamma(q, T) - \Gamma(0, T) \quad \text{with} \quad \Gamma(q, T) = [\kappa(T)]^{1.5} \Omega[q/\kappa(T)]. \tag{4.11}$$

Ω is a scaling function. Consequently, we performed a 4-dimensional integration implemented in MATLAB to calculate the momentum resolution effect on $\text{P}(\tau_{\text{NSE}})$ according to Eq. (4.9).

For the 2D spin system of Rb_2MnF_4, the momentum transfer $\boldsymbol{Q}_{2D}$ lies in the magnetic planes and the reduced momentum transfer $q_{2D} = \sqrt{x_1^2 + x_2^2}$ is measured from the antiferromagnetic zone center. Regarding to the dynamic scaling hypothesis of the 2D HAFM [Eq. (2.31)], the scattering function S reads

$$S(q_{2D}, \omega) = \frac{S_0}{1 + q_{2D}^2 \xi^2} \frac{\Gamma \gamma_q}{\Gamma^2 \gamma_q^2 + x_4^2}, \tag{4.12}$$

where ξ is the correlation length and $\gamma_q = \sqrt{1 + 1.7 q^2 \xi^2}$. By inserting Γ of Rb_2MnF_4 obtained at TRISP, it allows us to estimate the effects of the intrinsic energy resolution and finite momentum resolution. In contrast to MnF_2, the latter was calculated assuming 2D correlations in the $(HK0)$ scattering plane.

In both cases, the corresponding linewidth broadening Γ_R is obtained by fitting of $P(\tau_{NSE})$ to Eq. (3.12). As a result, Γ_R is roughly independent of temperature for $T \geq T_N$ and amounts to about $5\,\mu$eV in MnF_2 and $1.6\,\mu$eV in Rb_2MnF_4. The latter value includes $0.8\,\mu$eV of the intrinsic spin-echo resolution and $0.8\,\mu$eV of the finite momentum resolution. The reason for the larger value in MnF_2 is the relaxed vertical resolution Q_z, which has no effect in the 2D spin system of Rb_2MnF_4.

4.5.3 An experimental verification of the analysis technique

At first, we used the MnF_2 crystal to check the applicability of our analysis technique in analyzing the critical scattering measurement at $T = 69\,$K. Fig. 4.7 shows typical NSE data $P(\tau_{NSE})$ of MnF_2 using the *DC* mode at TRISP at the pure antiferromagnetic Bragg point $\boldsymbol{Q} = (300)$ and the result of a fit to the model described above. A prominent feature of the data is the fast oscillation of the polarization in the low τ_{NSE} region, which is displayed as red area in panel (a) and resolved in the zoomed version in panel (b). As discussed in Sec. 3.4.4, these oscillations result from the τ_{NSE}-dependent phase difference between $\boldsymbol{P}_{f,\parallel}$ and $\boldsymbol{P}_{f,\perp}$ [see Fig. 4.5 (c) and Eq. (4.4)],

$$\varphi_{f,\parallel} - \varphi_{f,\perp} = -2\varphi_i, \tag{4.13}$$

where φ_i depends on the wave vector $k_i = k_f = 2.35\,\text{Å}^{-1}$. According to Eq. (3.42), the oscillation period is = 0.148 A or 0.09 ps, in good agreement with our observation in Fig. 4.7 (b). For positive τ_{NSE} ($\uparrow\uparrow$ field configuration), only the polarization $\boldsymbol{P}_{f,\parallel}$ obeys the spin-echo condition, whereas the polarization $\boldsymbol{P}_{f,\perp}$ is depolarized with increasing τ_{NSE}, such that the oscillation amplitude decreases.

For negative τ_{NSE} ($\uparrow\downarrow$ field configuration) $\boldsymbol{P}_{f,\perp}$ fulfills the spin-echo condition and the remaining polarization $\boldsymbol{P}_{f,\perp}$ generates the oscillations. In Fig. 4.7 (a), the amplitudes of $\boldsymbol{P}_{f,\parallel}$ and $\boldsymbol{P}_{f,\perp}$, denoted by $P_\parallel$ and $P_\perp$, are extracted from these complicated spin-echo

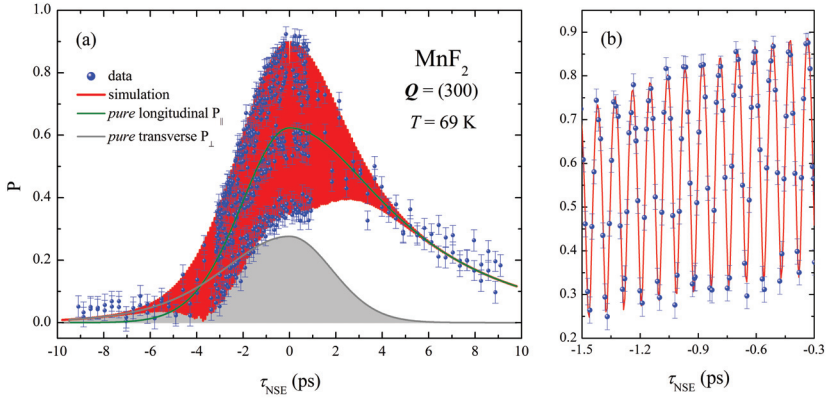

Fig. 4.7: Sample echo data of critical scattering in MnF_2 and fit with the model described in the text at $\boldsymbol{Q} = (300)$ at $T = 69\,\mathrm{K}$, where $T_N = 67.3\,\mathrm{K}$. (a) and the zoom (b) show the fast oscillation of the polarization resulting from the interference of scattering by $\boldsymbol{M}_\parallel$ and $\boldsymbol{M}_\perp$. The oscillation period is discussed in the text. A positive (negative) sign of τ_{NSE} corresponds to ↑↑ (↑↓) field configuration. The lines $P_\parallel$ and $P_\perp$ show the contribution of the $\boldsymbol{M}_\parallel$ and $\boldsymbol{M}_\perp$ to the polarization, where the peaks of these curves are proportional to the integrated intensities.

signals. The lines of the $P_\parallel$ and $P_\perp$ result from the contribution of the $\boldsymbol{M}_\parallel$ and $\boldsymbol{M}_\perp$. The ratio of peaks at $\tau_{NSE} = 0$ between $P_\parallel$ and $P_\perp$ shows the relative integrated intensity $I_\parallel/I_\perp$. At large τ_{NSE} beyond the oscillation regime $\tau_{NSE} > 5$ ps, $P(\tau_{NSE})$ can be modeled by a simple exponential decay [see Eq. (3.12)]. Thus the asymmetry in the decay between $\tau_{NSE} > 0$ and $\tau_{NSE} < 0$ indicates $\Gamma_\parallel \ll \Gamma_\perp$.

4.5.4 Representative NSE data for MnF_2 and Rb_2MnF_4

In the following NSE scans on both materials, data were collected during several beam times at TRISP with slightly varying crystal mounts. Consistent thermometry between these runs was ensured by measuring the temperature dependent intensities of magnetic Bragg reflections at the beginning of each run. Representative scans of spin-echo polarization P *vs.* spin-echo time τ_{NSE} [ps] above T_N for MnF_2 and Rb_2MnF_4 are shown. With the advantage of the proposed analysis technique [see Sec. 3.4.3], we are able to discriminate between the longitudinal and transverse fluctuations ($\boldsymbol{M}_\parallel$ and $\boldsymbol{M}_\perp$) at positions in $\boldsymbol{Q} = (300)$ for MnF_2 and in $\boldsymbol{Q} = (0.5\,0.5\,0)$ for Rb_2MnF_4, respectively. During these measurements, the temperature was stable within 1 mK.

3D AFM MnF_2

Representative NSE data of MnF_2 and fits with the model are shown from Fig 4.8 to Fig. 4.10, from the temperature close to T_N to the temperature far away from T_N. The longitudinal and transverse contribution to the critical fluctuations are shown in green and grey with shaded areas, respectively. As discussed in Sec. 3.3, the *NRSE* and *DC* modes at TRISP were used to measure the polarization in the large and small τ_{NSE} regions, respectively. For the *DC* mode, the experimental range of τ_{NSE} is $|\tau_{NSE}| = 9.18\,ps$, while for the *NRSE* mode the τ_{NSE} range is $4.98\,ps < |\tau_{NSE}| < 100\,ps$. Note that the sign of τ_{NSE} shows the applied field configuration ($\uparrow\uparrow$ or $\uparrow\downarrow$).

Fig. 4.8 shows the NSE data at (a) $T = 67.35\,K$, (b) $T = 67.70\,K$, and (c) $T = 68.30\,K$, which are close to $T_N = 67.3\,K$. Due to the presence of the anisotropy field, only the longitudinal fluctuations $\boldsymbol{M}_\parallel$ become critical and largely dominate the magnetic critical scattering. This fact leads to the smaller amplitudes of the curve $P_\perp$ resulting from the transverse fluctuations $\boldsymbol{M}_\perp$. In Fig. 4.8 (a), $P_\perp$ is negligible compared to the longitudinal contribution to the polarization $P_\parallel$. The small longitudinal linewidth $\Gamma_\parallel$ (or inverse magnetic lifetime) indicates that $\boldsymbol{M}_\parallel$ is still small and remains static. In addition, $P_\parallel$ in the positive τ_{NSE} range can be fitted using a conventional exponential decay [see Eq.(3.12)]. While T increases as in Fig. 4.8 (b) and (c), both $\boldsymbol{M}_\parallel$ and $\boldsymbol{M}_\perp$ become more relaxational and thus the use of the *DC* mode at TRISP is needed to resolve such a large Γ of the magnetic fluctuations. Further, Fig. 4.8 (c) shows the experimental data resulting from the *NRSE* and *DC* modes, which gives a credence to our coil calibrations.

Fig. 4.9 illustrates the cases of P *vs.* τ_{NSE} in the intermediate temperature range at (a) $T = 68.60\,K$, (b) $T = 69.10\,K$, and (c) $T = 69.60\,K$. In addition, at $T \gg T_N$ the NSE data of MnF_2 are shown in Fig. 4.10 with (a) $T = 70.10\,K$, (b) $T = 70.85\,K$, and (c) $T = 71.35\,K$. Among these experimental data, the use of the *DC* mode at TRISP plays an important role to resolve the highly relaxational $\boldsymbol{M}_\parallel$ and $\boldsymbol{M}_\perp$. The oscillation behavior resulting from the interference of $\boldsymbol{M}_\parallel$ and $\boldsymbol{M}_\perp$ disappears when the non-echo fluctuations are fully depolarized. In the positive τ_{NSE} range, $\boldsymbol{M}_\perp$ is the non-echo contribution to the polarization and thus the curve $P_\perp$ vanishes eventually when τ_{NSE} increases. Consequently $P(\tau_{NSE} > 5\,ps)$ reflects the pure longitudinal contribution $P_\parallel$. In the negative τ_{NSE} range, $\boldsymbol{M}_\parallel$ is the non-echo contribution to the polarization but with large scattering intensity. This makes the conventional data analysis difficult, especially in the current case where $\boldsymbol{M}_\perp$ is quite relaxational. With the advantage of our analysis technique, we are able to discriminate the contribution of $\boldsymbol{M}_\parallel$ and $\boldsymbol{M}_\perp$ in the whole experimental data range. In Fig. 4.9 (c), we verified again the behavior of oscillations arising from the interference of scattering by $\boldsymbol{M}_\parallel$ and $\boldsymbol{M}_\perp$. The obtained oscillating period is in good agreement with our expectation.

In summary, Table 4.1 lists the fitting results of MnF_2 extracted from our analysis model, containing the $\Gamma_\parallel$, $\Gamma_\perp$, and $I_\perp/I_\parallel$ at various T and the corresponding reduced

T(K)	t	$\Gamma_{\parallel}(\mu\text{eV})$	$\Gamma_{\perp}(\mu\text{eV})$	$I_{\perp}/I_{\parallel}$
67.35	2.8×10^{-3}	7.0312 ± 0.2532	3.3669 ± 2.5565	0.035
67.45	4.3×10^{-3}	14.304 ± 0.35666	39.614 ± 14.919	0.106
67.50	5.1×10^{-3}	16.043 ± 0.32748	94.904 ± 21.74	0.150
67.55	5.8×10^{-3}	18.564 ± 0.54683	133.254 ± 38.98	0.187
67.70	8.0×10^{-3}	24.885 ± 0.58036	221.529 ± 26.303	0.314
67.85	0.010	35.165 ± 0.92449	241.121 ± 52.163	0.492
68.10	0.014	51.798 ± 1.8904	273.267 ± 53.833	0.535
68.30	0.017	68.865 ± 1.8718	297.651 ± 40.268	0.538
68.35	0.018	77.788 ± 2.3526	268.573 ± 29.196	0.521
68.60	0.022	90.391 ± 2.2326	310.486 ± 38.983	0.574
68.85	0.025	102.708 ± 2.5447	311.99 ± 28.62	0.589
69.10	0.029	123.505 ± 4.9495	298.383 ± 45.832	0.534
69.35	0.033	136.32 ± 3.5908	334.104 ± 34.487	0.632
69.60	0.036	142.862 ± 5.1161	359.997 ± 45.92	0.728
69.85	0.040	160.236 ± 4.6085	318.166 ± 34.692	0.569
70.10	0.044	167.092 ± 5.267	320.291 ± 45.448	0.630
70.35	0.048	174.039 ± 7.8894	324.17 ± 56.203	0.590
70.60	0.051	184.22 ± 9.1761	333.678 ± 57.371	0.597
70.85	0.055	200.427 ± 6.7651	400.719 ± 46.51	0.728
71.10	0.059	214.516 ± 7.5503	462.295 ± 66.872	0.798
71.35	0.063	236.336 ± 12.273	367.983 ± 63.282	0.613
71.60	0.066	231.213 ± 12.041	463.919 ± 85.715	0.822

Table 4.1: Experimental results of critical scattering in MnF_2 at $\boldsymbol{Q} = (300)$. $\Gamma_{\parallel}$, $\Gamma_{\perp}$, and the relative integrated intensities are extracted from the aforementioned analysis technique.

temperature t. It is clear that the system tends to enter the *isotropic* paramagnetic state, where the relative integrated intensities $I_{\parallel}/I_{\perp} \to 1$ as T increases. At $T \gg T_N$, the thermal fluctuations gradually come into play in the magnetic interactions of MnF_2 and thus suppress the contribution of the anisotropic field.

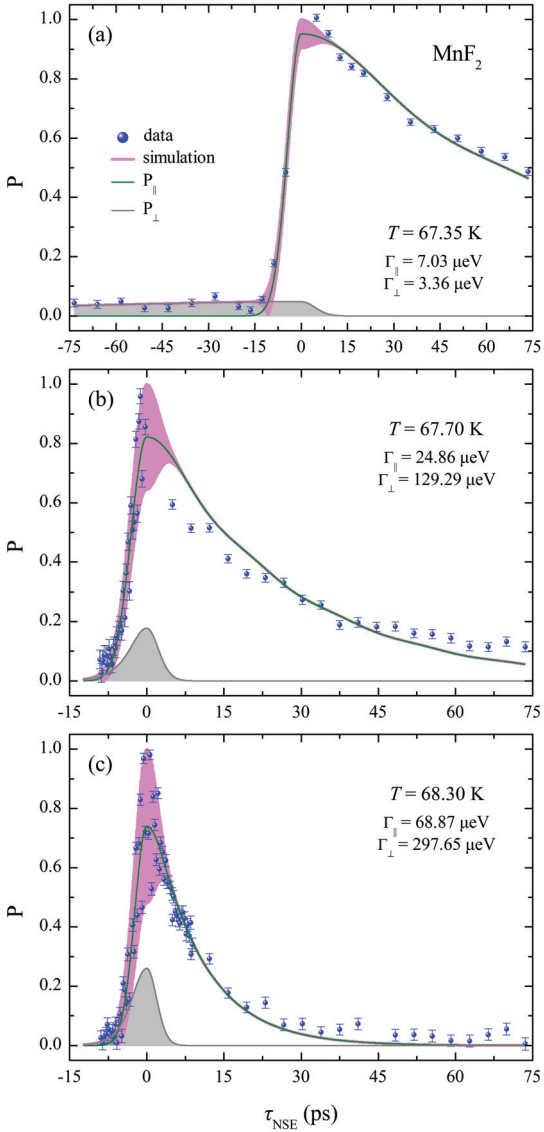

Fig. 4.8: Representative NSE data of critical scattering of MnF_2 and fits with the model at $\boldsymbol{Q} = (300)$ at temperatures close to $T_N = 67.3\,K$: (a) $T = 67.35\,K$, (b) $T = 67.70\,K$, and (c) $T = 68.30\,K$.

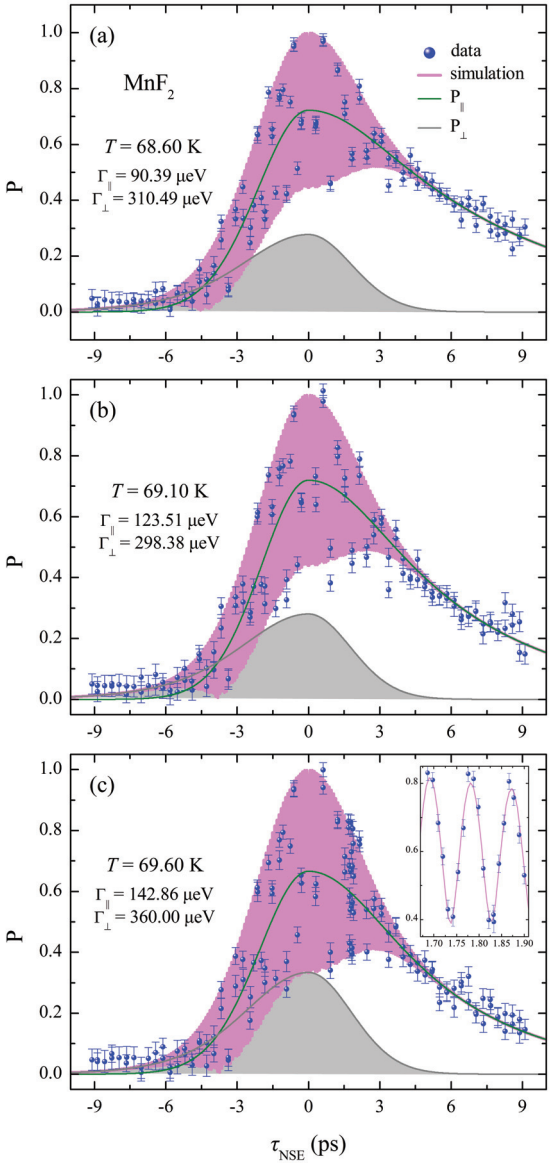

Fig. 4.9: Continued from Fig. 4.8. Representative NSE data of MnF_2 in the intermediate temperature range at (a) $T = 68.60\,\mathrm{K}$, (b) $T = 69.10\,\mathrm{K}$, and (c) $T = 69.60\,\mathrm{K}$.

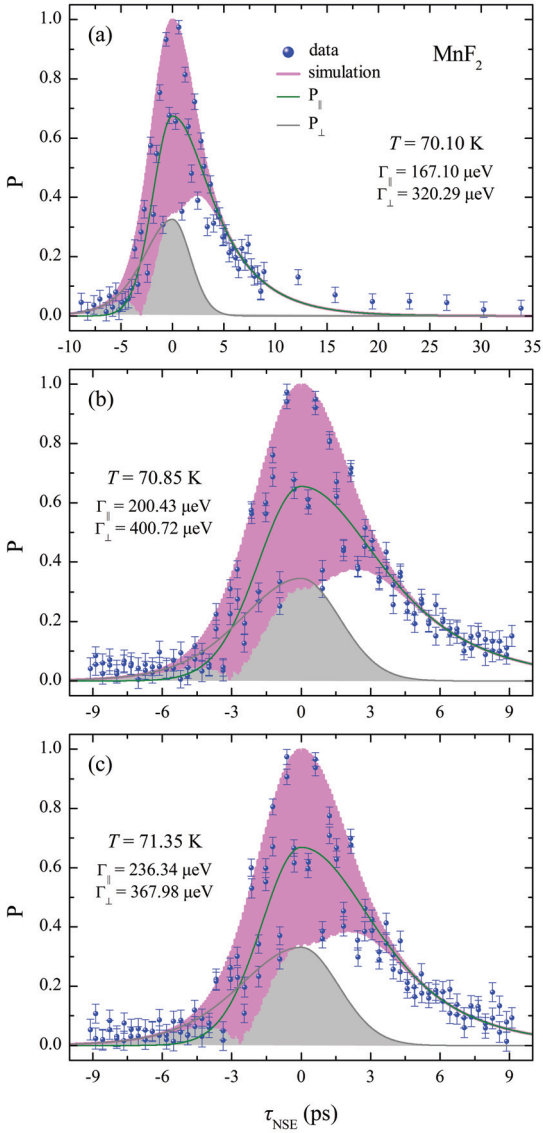

Fig. 4.10: Continued from Fig. 4.9. Representative NSE data of MnF_2 for $T \gg T_N$ at (a) $T = 70.10$ K, (b) $T = 70.85$ K, and (c) $T = 71.35$ K.

2D AFM Rb_2MnF_4

Representative NSE scans of P *vs.* τ_{NSE} for Rb_2MnF_4 at $\boldsymbol{Q} = (0.5\,0.5\,0)$ and fits with the model are shown from Fig 4.11 to Fig. 4.13. Here we use the same notation and symbols in the plots as in MnF_2. According to Sec. 4.3 for Rb_2MnF_4, $\boldsymbol{M}_\parallel$ ($\boldsymbol{M}_\perp$) is perpendicular (parallel) to the (HK0) scattering plane and fulfills the spin-echo condition for negative (positive) τ_{NSE} corresponding to $\uparrow\downarrow$ ($\uparrow\uparrow$) magnetic field configuration.

Fig. 4.11 shows the NSE data of Rb_2MnF_4 at (a) $T = 38\,K$, (b) $T = 39.5\,K$, and (c) $T = 41\,K$. Close to $T_N = 37.6\,K$, Fig. 4.11 (a) shows that the intensity of $\boldsymbol{M}_\parallel$ dominates and $\boldsymbol{M}_\perp$ has nearly no effect on the NSE signal. The obtained $\Gamma_\parallel$ is small, so that for $\tau_{NSE} < 0$ the polarization decays slowly. Upon heating, Fig. 4.11 (b) and (b) illustrate that $\Gamma_\parallel$ increases rapidly, leading to a faster decay of $P(\tau_{NSE} < 0)$. For $\tau_{NSE} > 0$, $\Gamma_\perp$ is rather large and evolves more smoothly upon heating. Experimentally, we used the *DC* mode for $\tau_{NSE} > 0$ and the *NRSE* mode for $\tau_{NSE} < 0$ in these experiments.

Fig. 4.12 illustrates the cases of Rb_2MnF_4 in the intermediate temperature range at (a) $T = 68.60\,K$, (b) $T = 69.10\,K$, and (c) $T = 69.60\,K$. In addition, Fig. 4.10 shows the NSE data in the *isotropic* limit at $T \gg T_N$, with (a) $T = 70.10\,K$, (b) $T = 70.85\,K$, and (c) $T = 71.35\,K$. The use of the *DC* mode at TRISP plays a prominent role to resolve the interference of $\boldsymbol{M}_\parallel$ and $\boldsymbol{M}_\perp$ especially in the low τ_{NSE} region. This oscillation behavior disappears when $\boldsymbol{M}_\parallel$ at positive τ_{NSE} and $\boldsymbol{M}_\perp$ at negative τ_{NSE} are fully depolarized. Beyond the oscillation region, $P(\tau_{NSE} < 0)$ ($P(\tau_{NSE} > 0)$) reflects the pure longitudinal (transverse) contribution $P_\parallel$ ($P_\perp$). Upon heating, the intensity ratio $I_\perp/I_\parallel$ approaches unity, as expected for the isotropic spin fluctuations. $\Gamma_\parallel$ increases rapidly, leading to a faster decay of $P(\tau_{NSE} < 0)$; $\Gamma_\perp$ is rather large at T_N and evolves more smoothly upon heating, so that $P(\tau_{NSE} > 0)$ shows less variation with temperature.

To summarize, we have separated the contribution of $\boldsymbol{M}_\parallel$ and $\boldsymbol{M}_\perp$ to the polarization of Rb_2MnF_4 in the whole experimental data range. Table 4.2 lists all the results extracted from our analysis model, containing the $\Gamma_\parallel$, $\Gamma_\perp$, and $I_\perp/I_\parallel$ at various T and the corresponding reduced temperature t.

T(K)	t	$\Gamma_{\parallel}(\mu\text{eV})$	$\Gamma_{\perp}(\mu\text{eV})$	$I_{\perp}/I_{\parallel}$
37.6	0	4.293 ± 0.029492	161.309 ± 16.784	0.067
38	0.011	6.8238 ± 0.044336	164.429 ± 11.319	0.108
38.5	0.024	14.095 ± 0.08394	191.42 ± 9.5577	0.176
39	0.037	19.525 ± 0.12778	173.943 ± 7.5595	0.221
39.5	0.051	29.673 ± 0.23424	166.908 ± 6.5486	0.262
40	0.064	37.123 ± 0.3808	191.031 ± 7.0526	0.333
40.5	0.077	49.633 ± 0.62686	176.37 ± 6.0363	0.376
41	0.090	59.028 ± 0.90203	191.601 ± 6.3016	0.444
41.5	0.10	72.848 ± 0.81461	188.792 ± 5.9159	0.462
42	0.12	83.193 ± 1.0572	194.354 ± 6.2666	0.502
42.5	0.13	94.851 ± 1.2663	215.019 ± 7.0532	0.564
43	0.14	104.477 ± 1.5763	216.841 ± 7.1653	0.602
43.25	0.15	118.265 ± 1.0293	240.486 ± 4.0574	0.600
43.5	0.16	125.381 ± 1.1177	240.964 ± 4.1129	0.614
43.75	0.16	129.154 ± 1.2088	250.135 ± 4.5314	0.631
44	0.17	136.106 ± 1.3028	247.423 ± 4.3504	0.658
44.25	0.18	142.136 ± 1.4096	254.068 ± 4.8136	0.649
44.5	0.18	149.148 ± 1.5144	251.919 ± 4.8278	0.649
45	0.20	161.019 ± 1.7542	264.691 ± 5.4781	0.685
45.75	0.22	174.665 ± 2.1804	291.702 ± 7.5155	0.765
46.5	0.24	187.177 ± 2.6704	292.966 ± 10.64	0.817
47.25	0.26	201.617 ± 3.042	314.072 ± 7.2452	0.916
48	0.28	225.053 ± 3.8175	347.225 ± 9.1766	0.926
48.75	0.30	233.898 ± 4.2806	349.417 ± 9.318	0.943
49.5	0.32	247.714 ± 5.0273	364.993 ± 11.504	0.942
50.25	0.34	261.649 ± 5.8977	389.707 ± 13.741	0.990

Table 4.2: Experimental results of critical scattering in Rb_2MnF_4 at $\boldsymbol{Q} = (0.5\,0.5\,0)$. $\Gamma_{\parallel}$, $\Gamma_{\perp}$, and the relative integrated intensities are extracted from the aforementioned analysis technique.

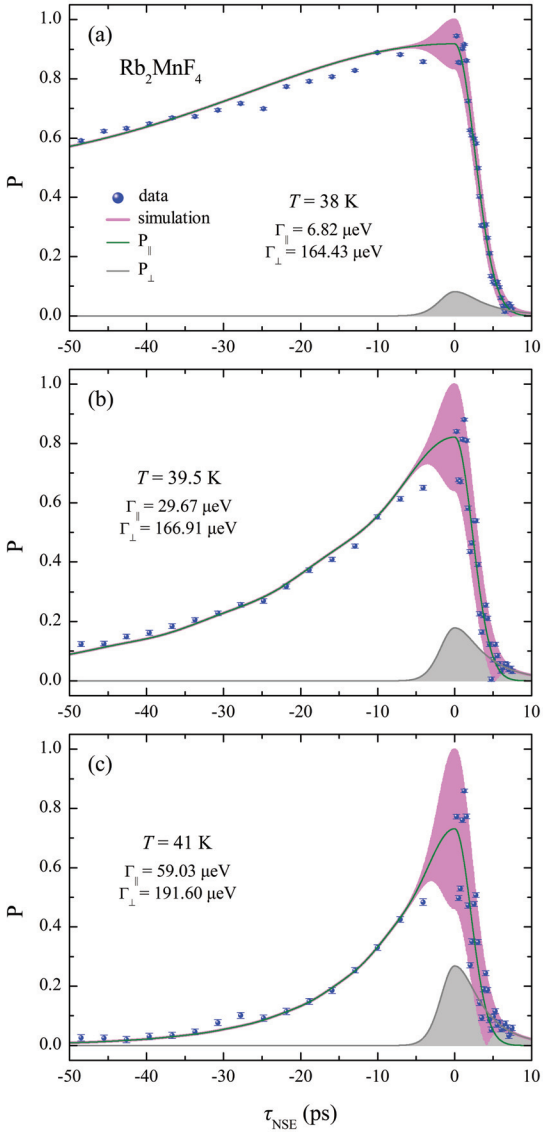

Fig. 4.11: Representative NSE data of critical scattering of Rb_2MnF_4 and fits with the model at $\boldsymbol{Q} = (0.5\,0.5\,0)$ at temperatures close to $T_N = 37.6\,K$: (a) $T = 38\,K$, (b) $T = 39.5\,K$, and (c) $T = 41\,K$.

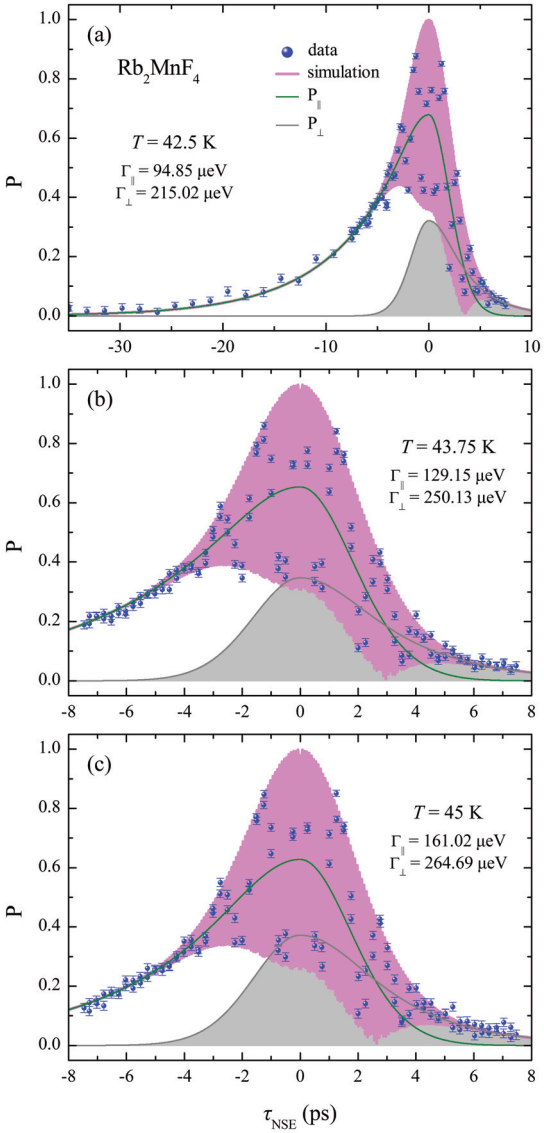

Fig. 4.12: Continued from Fig. 4.11. Representative NSE data of Rb_2MnF_4 in the intermediate temperature range at (a) $T = 42.50\,\mathrm{K}$, (b) $T = 43.75\,\mathrm{K}$, and (c) $T = 45\,\mathrm{K}$.

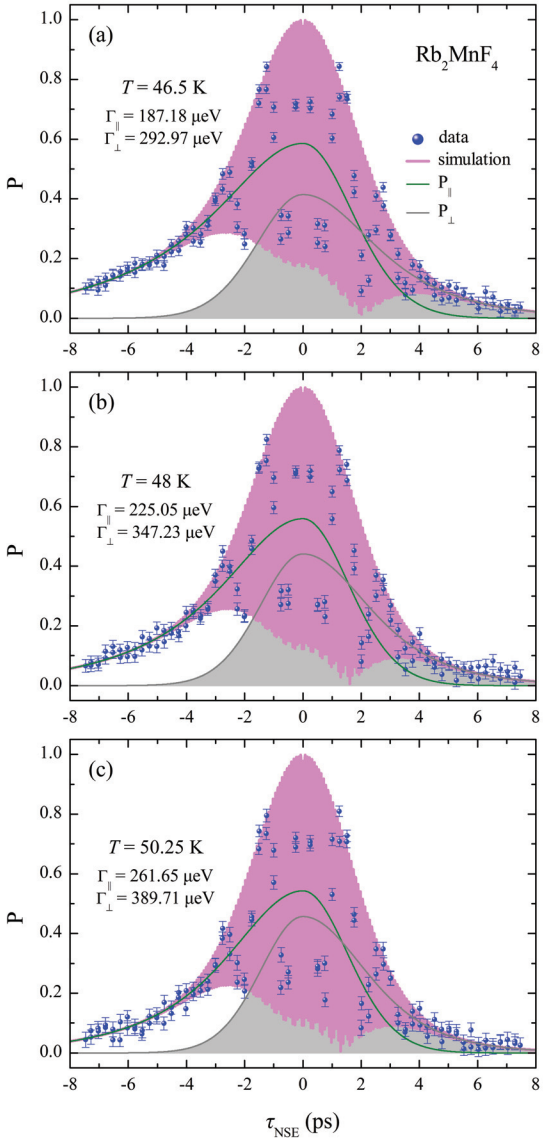

Fig. 4.13: Continued from Fig. 4.12. Representative NSE data of Rb_2MnF_4 for $T \gg T_N$ at (a) $T = 46.5$ K, (b) $T = 48$ K, and (c) $T = 50.25$ K.

5 Critical dynamics in classical antiferromagnets

5.1 3D AFM MnF_2

Fig. 5.1 (a) shows the longitudinal linewidths $\Gamma_\parallel(T)$ at $\boldsymbol{Q} = (300)$ extracted from the model calculations described in Chapter 4. The bare measured linewidth $\Gamma_\parallel(T = T_N) = 5\,\mu$eV is larger than the intrinsic spectrometer resolution ($< 1\mu$ eV) and agrees with the additional linewidth broadening Γ_0 calculated above by taking the finite $\boldsymbol{Q}$ resolution into account. According to the dynamical scaling prediction [6, 7], the resolution-corrected $\Gamma_\parallel$ follows a power law

$$\Gamma_\parallel(T) = A_\parallel t^{z\nu} \tag{5.1}$$

where $A_\parallel$ is a normalized amplitude, $t = T/T_N - 1$ is the reduced temperature, and $\kappa = \xi^{-1} \sim t^\nu$ is the inverse correlation length.

The $\Gamma_\parallel(T)$ data in Fig. 5.1 (a) clearly deviate from a single power law in the shaded region at around $T = 69$ K. After subtracting the residual linewidth Γ_R, we performed separate fits of Eq. (5.1) to the regions below and above 69 K. The blue dotted line fits the data in the range $T_N < T < 1.01\,T_N$, with a normalized amplitude $A_\parallel = 1.148 \times 10^4\,\mu$eV and an exponent $z\nu = 1.25(2)$. With the exponent $\nu_{3D\,IAFM} = 0.6301$ predicted for 3D Ising antiferromagnet (3D IAFM) scaling [53], we obtain $z = 1.98(3)$, which matches the $z_{3D\,IAFM} = 2$ expected for this universality class within the experimental error [7]. The 3D Heisenberg antiferromagnet (3D HAFM) scaling in this temperature range can be excluded: dividing $z\nu$ by $\nu_{3D\,HAFM} = 0.7112$ predicted for the 3D HAFM [54] results in $z = 1.77$, inconsistent with $z_{3D\,HAFM} = 1.5$ predicted for the 3D HAFM [7]. For $T > 1.04\,T_N$, the red dotted curve corresponds to a normalized amplitude $A_\parallel = 3.830 \times 10^3\,\mu$eV and an exponent $z\nu = 1.02(3)$. Dividing by $\nu_{3D\,HAFM}$ gives $z = 1.43(5)$, close to 3D HAFM scaling, whereas the $z = 1.62(4)$ obtained with $\nu_{3D\,IAFM}$ is inconsistent with the theoretical $z_{3D\,IAFM} = 2$. Thus the data $\Gamma_\parallel(T)$ show a crossover from 3D IAFM close to T_N to 3D HAFM scaling for $T \gg T_N$. The relative amplitude $A_{\parallel,3D\,IAFM}/A_{\parallel,3D\,HAFM} = 3.0$ resulting from the fits is in good agreement with the value 3.1 predicted by Riedel and Wegner [10, 11], who extended the dynamical scaling theory to anisotropic systems.

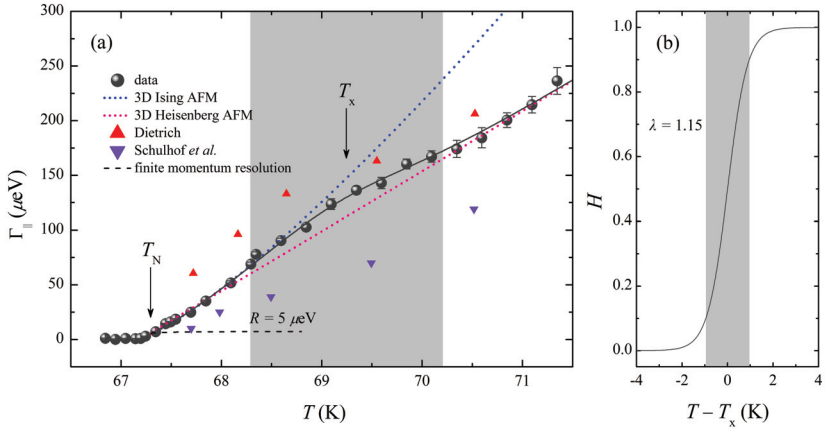

Fig. 5.1: (a) Temperature dependence of longitudinal linewidths $\Gamma_\parallel$ in MnF_2 at $\boldsymbol{Q} = (300)$. It shows a crossover from 3D Ising to 3D Heisenberg critical scaling, where the gray band indicates the crossover region centered at T_x. $R = 5\,\mu$eV is the broadening due to the finite momentum resolution. (b) The phenomenological expression for the crossover function H *vs.* $T - T_x$. The fitting parameter $\lambda = 1.15$ defines the transition temperature width ΔT of the crossover behavior, as described in the text. The gray band corresponds to the ΔT.

For a quantitative description of the crossover region of $\Gamma_\parallel(T)$, we use the phenomenological expression of a crossover function with the linewidths Γ_{Ising} below and $\Gamma_{\text{Heisenberg}}$ above the crossover region

$$\Gamma(T) = \left[1 - H(T - T_x)\right] \cdot \Gamma_{\text{Ising}} + H(T - T_x) \cdot \Gamma_{\text{Heisenberg}}, \tag{5.2}$$

$$H(T - T_x) = 1/2 + 1/2 \tanh\left[\lambda(T - T_x)\right]. \tag{5.3}$$

$H(T - T_x)$ is a slowly varying function symmetrically centered at a crossover temperature T_x. $H(T)$ defines a soft continuous transition from 0 to 1 and approaches the Heaviside step function for $\lambda \to \infty$. The transition width λ is defined as the region $0.1 < H < 0.9$ describing the crossover temperature range $\Delta T = |T - T_x|$. A fit of Eq. (5.2) to our data gives $\lambda = 1.15$ and $T_x = 69.2(1)\,\text{K}$ (or $t_x = 0.029(1)$). Thus $\Delta T = 0.96\,\text{K}$ can be deduced and it defines a crossover temperature region $1.01\,T_N < T < 1.04\,T_N$ centered at T_x. The crossover behavior of the dynamic fluctuations is not surprising as the uniaxial anisotropy is expected to be significant only close to T_N, whereas far above T_N isotropic 3D HAFM scaling should dominate.

Schulhof *et al.* [13] pointed out that their $\Gamma_\parallel$ result for MnF_2 favors the value $z = 1.5$, consistent with 3D HAFM scaling, whereas the static exponents ν and γ agree with

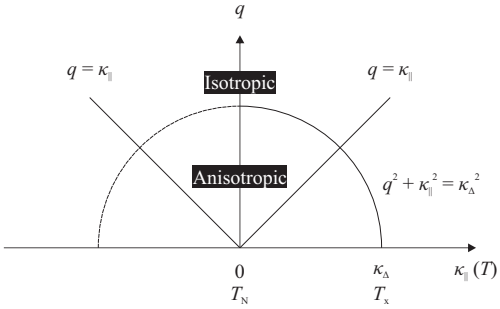

Fig. 5.2: A phase diagram of the critical phenomena of an anisotropic system. The corresponding anisotopic and isotropic phases in the $(q, \kappa_\parallel)$ space are separated by the boundary $\kappa_\parallel^2 + q^2 = \kappa_\Delta^2$.

the 3D IAFM model. They argued that the reason for this discrepancy might be the small range in momentum $\boldsymbol{q}$ where the crossover is visible in $\Gamma_\parallel$. Riedel and Wegner [10, 11] introduced a characteristic wave vector $\kappa_\Delta = \kappa_\parallel(t_x, q = 0)$ defining the crossover between isotropic and anisotropic regions in momentum space, with the boundary $\kappa_\parallel^2 + q^2 = \kappa_\Delta^2$ [see Fig. 5.2]. They estimate $\kappa_\Delta = 0.054 \text{Å}^{-1}$ for MnF_2, corresponding to $T_x \sim T_N + 2\,\text{K}$, close to the observation in the present work. In addition, Pfeuty *et al.* [12] predicted such a crossover from 3D IAFM to 3D HAFM scaling occurs at $t_x = \alpha_I^{0.8}$, where the reduced anisotropy $\alpha_I = H_A/H_E$ is the ratio of anisotropy and exchange fields in the spin Hamiltonian. Experimentally, $\alpha_I = 0.016$ from an antiferromagnetic resonance experiment of MnF_2 [88] gives $t_x = 0.036$, which is in good agreement with our experimental result. Frey and Schwabl calculated the critical dynamics by taking dipolar interactions into account [15]. From their formulas, we obtain a similar value of $\kappa_\Delta = 0.06\,\text{Å}^{-1}$. Since the linewidths $\Gamma_\parallel$ at $q \sim \kappa_\Delta$ were too narrow to be resolved by TAS, the crossover of the dynamical exponent z was missed. For the strongly anisotropic antiferromagnet FeF_2 [86], both $t_x = 0.45$ and $\kappa_\Delta = 0.29\,\text{Å}^{-1}$ are larger, such that the TAS experiment covered the 3D Ising region close to T_N without observing the crossover to Heisenberg dynamic scaling.

The energy width $\Gamma_\perp(T)$ of the transverse fluctuations is shown in Fig. 5.3 (a) in comparison with previous TAS data from [13, 14]. We observe a rapid increase of $\Gamma_\perp$ between T_N and the lower bound of the crossover region at $1.01\,T_N$, where $\Gamma_\perp$ saturates at $\sim 0.3\,\text{meV}$. Calculations predicted this saturation value, corresponding to $z_\perp = 0$ [11, 15, 16]. But $\Gamma_\perp$ is expected to stay constant in the broad range $T_N < T < T_x$, which contradicts both our data and the results of the early TAS experiments. $\Gamma_\perp$ increases beyond the crossover region ($T > 1.04\,T_N$), as expected for the

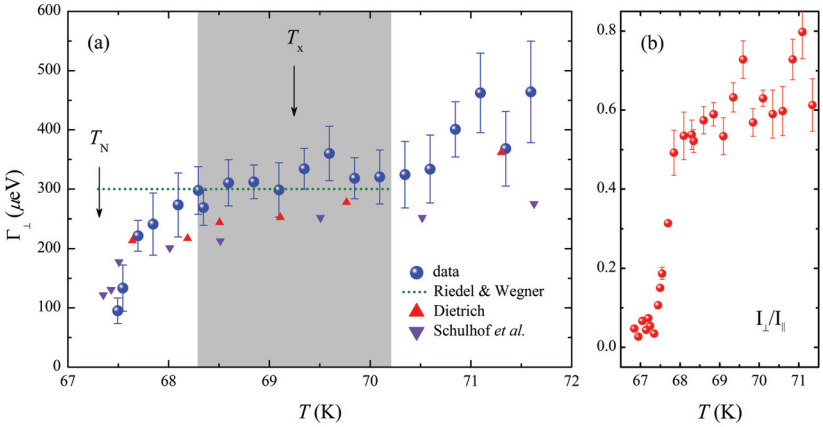

Fig. 5.3: (a) Temperature dependence of transverse linewidths $\Gamma_\perp$ in MnF_2 at $\boldsymbol{Q} = (300)$ and data from early TAS experiments [13, 14]. The crossover region (grey band) deduced from the longitudinal correlations is also included. The green dotted line shows the calculated $\Gamma_\perp$ by Riedel and Wegner [11]. (b) Ratio of integrated intensities $I_\perp/I_\parallel$. Close to T_N, $I_\parallel$ is much stronger. For $T > T_x$ in the 3D HAFM region, $I_\perp/I_\parallel$ is growing within the experimental temperature range and approaches unity for $T \gg T_N$.

3D HAFM scaling. The error bars increase at high temperature, because the wings of the Lorentzian line are cut by the transmission function $R(\omega)$ of the NRSE-TAS spectrometer (~ 0.8 meV FWHM). Hence the data quality does not allow fitting of a critical exponent and quantitative confirmation of 3D HAFM scaling of $\Gamma_\perp$ for $T \gg T_N$.

Fig. 5.3 (b) shows the ratio of integrated intensities $I_\perp/I_\parallel$ arising from $\boldsymbol{M}_\perp$ and $\boldsymbol{M}_\parallel$. Close to T_N, $\boldsymbol{M}_\parallel$ largely dominates the critical scattering due to the uniaxial anisotropy. As T increases, $I_\perp/I_\parallel$ is growing rapidly and then approaches 1 for $T \gg T_N$ indicating the system enters the 3D HAFM scaling.

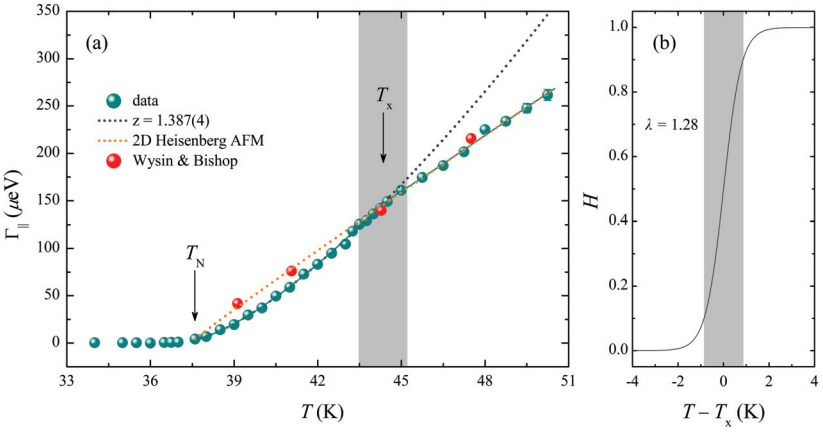

Fig. 5.4: (a) The longitudinal linewidths $\Gamma_\parallel$ *vs.* temperature of the critical fluctuations in Rb_4MnF_4 at $\boldsymbol{Q} = (0.5\,0.5\,0)$. $\Gamma_\parallel(T)$ shows a crossover in the critical scaling at $T_x = 44.3\,\mathrm{K}$, where the gray band indicates the crossover region centered at T_x. The orange dotted line shows the 2D HAFM scaling at $T \gg T_N$, in agreement with the calculated $\Gamma(T)$ by Wysin and Bishop in classical AFMs. (b) The crossover function H *vs.* $T - T_x$ for Rb_2MnF_4 is shown with $\lambda = 1.28$. The resulting crossover temperature region is $\Delta T = 1.7\,\mathrm{K}$, as depicted in the grey band.

5.2 2D AFM Rb_2MnF_4

Figure 5.4 (a) shows the linewidth $\Gamma_\parallel$ of the longitudinal fluctuations. The broadening of $\Gamma_\parallel$ sets in about 0.6 K below T_N and reaches 4.3 μeV at T_N. This value is larger than the calculated resolution of $\sim$ 1.6 μeV. Very close to T_N, where the fluctuations leading to the 3D order also must reflect 3D correlations, such that the finite Q_z resolution should become relevant. However, this temperature regime is very narrow, and the resolution correction should be insignificant in the range of reduced temperatures we are probing [19]. Nonetheless, we note that the observed width at T_N is very similar to the one in MnF_2 at T_N, where it most likely arises from the 3D spin correlations in conjunction with the poor vertical resolution. It is also similar to the residual linewidth of magnons at $T = 3$ K, deep in the Néel state of Rb_2MnF_4, which could be attributed to the effect of structural and/or magnetic domain boundaries. Further work is required to determine whether the small linewidth at T_N arises from an unidentified resolution effect or from intrinsic properties of the sample such as residual disorder. In the following analysis, we subtract this contribution from the temperature dependent $\Gamma_\parallel$ data.

The $\Gamma_\parallel(T)$ data in Fig. 5.4 (a) show a change in slope at around 44 K. From the dipo-

lar anisotropy, one expects a crossover from 2D Ising antiferromagnet (2D IAFM) scaling for $T \sim T_N$ to 2D Heisenberg antiferromagnet (2D HAFM) behavior for $T \gg T_N$. Such a crossover was observed by Lee *et al.* [17] for the correlation length $\xi_\parallel$ close to $T_x = 1.2\,T_N$. This value of T_x was calculated for an anisotropy parameter $\alpha_I = 0.0047$ extracted from the spin wave dynamics [126, 127, 128]. Fitting the power law $\Gamma_\parallel(t)$ of Eq. (5.1) in the range $T_N < T < 1.16\,T_N$ gives an exponent $z\nu = 1.387(4)$. This value depends only weakly on the choice of the fitting range; removing two data points at the upper or lower boundary changes the result within the error bar. Using the exponent $\nu_{2D\,IAFM} = 1$ predicted for 2D IAFM scaling [20], we obtain $z = 1.387(4)$, clearly different from the $z_{2D\,IAFM} = 1.75$ predicted for the 2D IAFM scaling [18]. Other simple models, such as the 3D IAFM scaling, also do not fit. With $\nu_{3D\,IAFM} = 0.6301$, we obtain $z = 2.201(6)$, different from the predicted $z_{3D\,IAFM} = 2$. This means that our linewidth data close to T_N are not consistent with the 2D IAFM behavior observed for the correlation length $\xi_\parallel$ [17]. In addition, such a deviation from 2D IAFM scaling with $\beta = 0.125$ [20] was also observed for the static exponent $\beta = 0.18$ deduced from the antiferromagnetic order parameter by Birgeneau *et al.* [19].

A possible reason for the unexpected scaling of $\Gamma_\parallel(T)$ is the the dipolar interaction, which is the major contributor to the magnon gap in the antiferromagnetically ordered state and can affect the universality class by virtue of its long spatial range. Based on theoretical considerations, Refs. [15, 82] argued that the long-range nature of the dipolar forces should have no effect on the correlation length in antiferromagnets, but that the critical dynamics are modified by additional damping processes, especially in the limit of small $\boldsymbol{q}$ and close to T_N. In 3D antiferromagnets such as MnF_2, the critical regime in which the long-range character of the dipolar interaction significantly affects the critical scaling is expected to be small [135]. Indeed, our investigation of MnF_2 did not uncover any evidence of such an effect. For the 2D case, a stronger influence of the long range character is expected [15], but to the best of our knowledge a calculation of the critical dynamics of a 2D antiferromagnets with dipolar interactions has not yet been reported. It is interesting to note that the critical exponent in a magnetic field H close to the bicritical point in the $H-T$ phase diagram of Rb_2MnF_4, $z = 1.35 \pm 0.02$ [8], is identical to ours within the experimental error. This suggests that the magnetic field does not close the damping channels actuated by the dipolar interaction.

For $T \gg T_N$ the impact of the anisotropy decreases, and the fluctuations are expected to follow the 2D HAFM model which exhibits magnetic long range order only for $T \to 0\,K$ [94]. It is not possible to obtain the critical exponent z from the relation of Eq. (5.1), as both t and ν are undefined in 2D HAFM scaling. The correlation length $\xi_{2D\,HAFM}$ for the pure $S = 5/2$ 2D HAFM has been calculated by Cuccoli *et al.* [42, 43] using a pure quantum self-consistent harmonic approximation (PQSCHA), and the influence of the

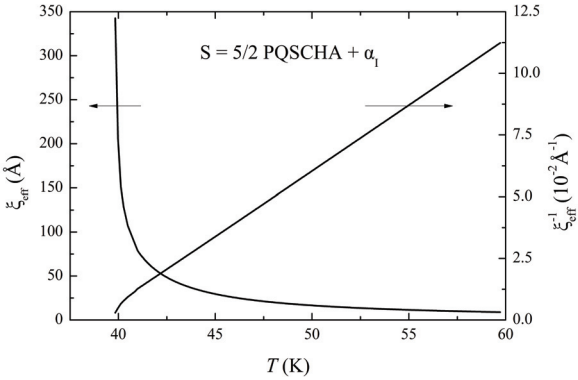

Fig. 5.5: Numerical results of the effective correlation length ξ_{eff} and its inverse $\kappa_{\text{eff}} = \xi_{\text{eff}}^{-1}$ *vs.* temperature. The latter terminates at $T = T_{\text{N}}$ and follows the 2D IAFM scaling.

small spin-space anisotropy can be described by the mean-field expression ξ_{eff} [35]:

$$\xi_{\text{eff}}(\alpha_{\text{I}}, T) = \frac{\xi_{\text{2D HAFM}}}{\sqrt{1 - \alpha_{\text{I}}\,\xi_{\text{2D HAFM}}^2(T)}}. \tag{5.4}$$

The effective (perturbed) correlation length ξ_{eff} is obtained by inserting $\alpha_{\text{I}} = 4.7 \times 10^{-3}$ [96, 127, 128] and the PQSCHA result. Fig. 5.5 shows the numerical results of ξ_{eff} and $\kappa_{\text{eff}} = \xi_{\text{eff}}^{-1}$ as a function of temperature. ξ_{eff}^{-1} vanishes at T_{N} due to the uniaxial anisotropy. Fitting the expression $\kappa = \kappa_0 t^{\nu}$ to the $\xi_{\text{eff}}^{-1}(T)$ data gives $\kappa_0 = 0.20581\,\text{Å}^{-1}$ and $\nu = 1.01$, in agreement with the static properties of 2D IAFM [20]. We employ the expression for describing $\Gamma(T)$ in 2D HAFM scaling

$$\Gamma(t) = A \times \xi_{\text{eff}}^{-z}(t), \tag{5.5}$$

where A is a normalized amplitude, t is the reduced temperature, and z is the dynamic critical exponent.

Fitting Eq. (5.5) to the data $\Gamma_{\parallel}$ at $T > 1.20\,T_{\text{N}}$ gives the normalized amplitude $A_{\parallel} = 3.362 \times 10^3\,\mu\text{eV}\cdot\text{Å}$ and the exponent $z_{\parallel} = 0.96(4)$. In contrast to $z = 1.35(2)$ by Christianson *et al.* [8], the obtained $z_{\parallel}$ is in agreement with the prediction $z = 1$ for the 2D HAFM [7]. This result also agrees with a numerical simulation of $\Gamma_{\parallel}$ by Wysin *et al.* [136], also shown in Fig. 5.4 (a), and with experimental results on a 2D HAFM model compound with $S = 1/2$ [40]. Finally we analyzed the entire data set $\Gamma_{\parallel}(T > T_{\text{N}})$ with the crossover function introduced in Eq. (5.2). The fitting results yield $\lambda = 1.28$ and $T_{\text{x}} = 44.3(4)$ (or $t_{\text{x}} = 0.179$). The resulting crossover temperature region reads

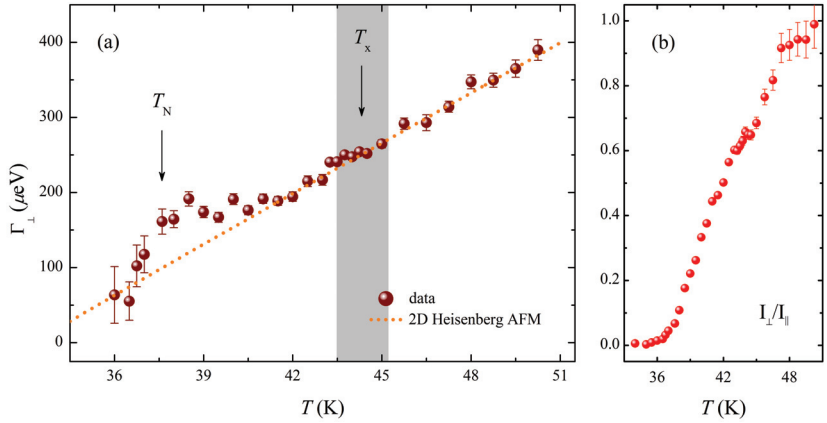

Fig. 5.6: (a) The transverse linewidths $\Gamma_\perp$ *vs.* temperature of the critical fluctuations in Rb_2MnF_4 at $\boldsymbol{Q} = (0.5\,0.5\,0)$. In the temperature range T_N and T_x, $\Gamma_\perp$ is finite and forms a plateau with $z_\perp = 0$. At $T \gg T_N$ 2D HAFM scaling is observed, as expected for the isotropic case. (b) Ratio of integrated intensities $I_\perp/I_\parallel$. Close to T_N, $\boldsymbol{M}_\parallel$ dominates the spin-echo signal. As T increases, $\boldsymbol{M}_\parallel$ and $\boldsymbol{M}_\perp$ become identical and thus enter the isotropic paramagnetic state with $I_\perp/I_\parallel = 1$.

$\Delta T = 1.7\,\mathrm{K}$, and T_x is slightly smaller than the predicted value. Fig. 5.4 (b) illustrates the crossover function $H(T - T_x)$ and the resulting temperature region.

The linewidth of the transverse fluctuations $\Gamma_\perp(T)$ is plotted in Fig. 5.6 (a). $\Gamma_\perp$ is nonzero at T_N, forms a plateau with $z_\perp \sim 0$ between T_N and T_x, and grows continuously for $T > T_x$. In the 2D HAFM regime observed for $\Gamma_\parallel(T > T_x)$, it is expected that $\Gamma_\perp(t) = \Gamma_\parallel(t)$ [10]. It was pointed out that the effective Néel temperatures for the longitudinal and transverse fluctuations $T_\parallel$ and $T_\perp$ are different in the anisotropic systems [137], such that the corresponding reduced temperature is $t = T/T_{\parallel,\perp} - 1$. T_N relevant for the magnetic ordering is the larger $T_\parallel$. We then fit $\Gamma_\perp = A_\perp \times \xi_{\mathrm{eff}}^{-z_\perp}$ to the data $\Gamma_\perp(T > T_x)$ assuming $A_\perp = A_\parallel$, where the latter is known from the scaling of $\Gamma_\parallel$. This fit gives $T_\perp = 33.3(14)\,\mathrm{K}$ and $z_\perp = 0.97(15)$ as expected for the 2D HAFM. This result is also supported by the intensity ratio $I_\perp/I_\parallel$ shown in Fig. 5.6 (b), which approaches 1 above T_x as expected for the identical behavior of $\boldsymbol{M}_\parallel$ and $\boldsymbol{M}_\perp$ in the 2D HAFM.

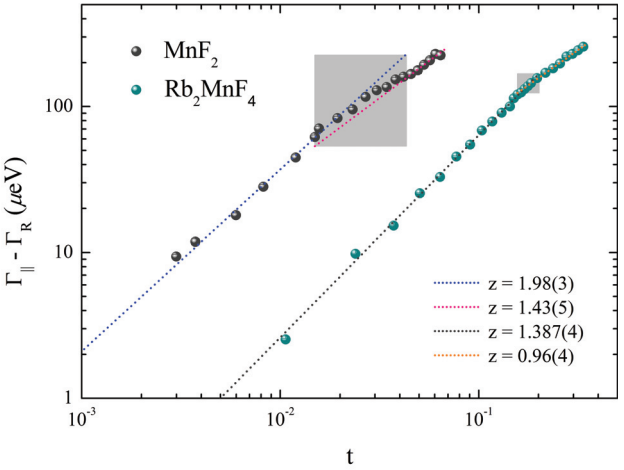

Fig. 5.7: Scaling plot of the linewidth of longitudinal spin fluctuations in MnF_2 and Rb_2MnF_4. The residual linewidths Γ_R at T_N for both materials are subtracted from the data. From [9].

5.3 Summary

We have investigated the dynamic critical exponents of the spin fluctuations in MnF_2 and Rb_2MnF_4, two canonical weakly anisotropic $S = 5/2$ antiferromagnets with 3D and 2D spin coupling, respectively. Fig. 5.7 summarizes the intrinsic linewidths of longitudinal spin fluctuations in MnF_2 and Rb_2MnF_4. Both compounds show a crossover in the scaling behavior resulting from the small uniaxial anisotropy induced by dipolar interactions. The dynamic critical exponent in MnF_2 changes from $z_\parallel = 1.43(5)$ at high T, consistent with 3D Heisenberg scaling, to $z_\parallel = 1.98(3)$ corresponding to a 3D Ising model close to T_N. This crossover occurs around $T_x = 1.03\,T_N$, consistent with predictions in the literature [11, 12]. The previous contradictory experimental results for the longitudinal fluctuations, with $z_\parallel$ ranging from 1.6 to 2.3, are mainly due to the insufficient energy resolution of conventional triple-axis spectroscopy. The transverse linewidths $\Gamma_\perp$ are consistent with the predicted value $z_\perp = 0$ around T_x, but $\Gamma_\perp$ decreases significantly upon cooling towards T_N. This behavior was also observed in earlier triple-axis spectroscopy experiments.

The dynamical critical exponent $z_\parallel$ measured in Rb_2MnF_4 changes around the crossover temperature $T_x = 1.18\,T_N$ from $z_\parallel = 0.96(4)$ for $T > T_x$, corresponding to the expected 2D Heisenberg scaling, to $z_\parallel = 1.387(4)$ for $T_N < T < T_x$. The latter value does not correspond to the expected $z = 1.75$ for the 2D Ising model. This scaling

behavior probably results from the long-range nature of the dipolar forces, which influence the dynamic scaling in antiferromagnets by opening additional damping channels, while the static exponents remain unaffected. The transverse spin fluctuations show constant linewidths ($z_\perp = 0$) close to T_N and are equal to the longitudinal fluctuations for $T \gg T_N$, where they show 2D Heisenberg scaling with $z_\perp = 0.97(15)$.

The high resolution three-axis spin-echo technique in combination with a ray tracing simulation of the spectrometer has thus provided detailed insight into the critical dynamics of antiferromagnets and helped resolve previous contradictory results. Our approach can straightforwardly be applied to a large class of questions on spin fluctuations and spin excitations, especially if a broad dynamic range with linewidths $< 1\,\mu$eV up to a few hundred μeV has to be covered.

6 Appendix: The dimerized spin system $TlCuCl_3$

The study of antiferromagnets in this thesis is aimed at establishing a firm experimental basis for the investigation of critical fluctuations by means of the high resolution spin-echo technique. The next step is to perform a similar study on quantum fluctuations in the vicinity of quantum phase transitions. We performed first steps in this direction and identified the dimerized spin system $TlCuCl_3$ as a good candidate for a spin-echo study. Quantum criticality occurs at a moderate pressure in zero magnetic field. In the present work, the crystal growth group at the MPI-FKF succeed in growing large crystals. First test experiments were performed using newly developed gas pressure cells from the sample environment group of the FRM II.

6.1 Introduction

Classical antiferromagnets usually show long-range magnetic order below the Néel temperature T_N, at which the strength of the thermal fluctuations is reduced and the magnetic moments can align in a well-defined structure. In quantum antiferromagnets, quantum fluctuations suppress long-range order and thus prevent the formation of such an ordered ground state even down to $T = 0\,K$, leaving the spin system remaining in a quantum disordered spin-liquid state. Fig. 6.1 shows a phase diagram of these quantum antiferromagnets. The ordered state may then be recovered above the critical value of a tuning parameter r, such as pressure, magnetic field, or chemical doping concentration [52, 138, 139]. These types of phase transition are known as quantum phase transitions (QPT), and are attracting much interest.

The dimerized spin system $TlCuCl_3$ provides a unique opportunity for experimental studies of QPT in that it undergoes a pressure-induced QPT to an ordered phase, occurring at the critical pressure $p_c = 1.07\,kbar$ [140, 141]. The applied pressure p is the inverse of the tuning parameter r. This ordered phase, which contains an unconventional longitudinal (Higgs) mode and two transverse (Goldstone) modes, has been studied by inelastic neutron scattering with continuous pressure control through the QPT [142]. Quantum and thermal fluctuations have qualitatively similar effects in melting the ordered phase and opening excitation gaps, but behave independently near a quantum critical point. In the quantum critical region, the dominant behavior is

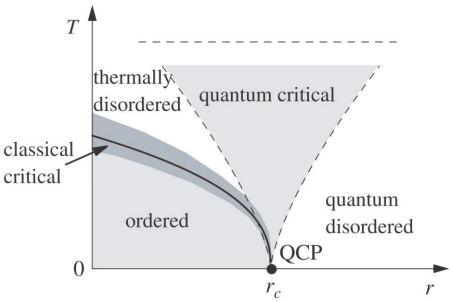

Fig. 6.1: A phase diagram of QPT for systems with a long-range ordered state at finite temperature. From [138].

quantum critical ω/T scaling of the energies and linewidths of critically damped excitations, whereas it crosses over to a narrow classical critical scaling region around $T_N(p)$.

We aim to study the critical fluctuations as a function of pressure and temperature through the QPT of $TlCuCl_3$ using TRISP, employing the NRSE technique. With the advantage of our new analysis technique, we are able to discriminate the longitudinal and transverse components of the critical fluctuations through the appropriate choice of magnetic field configurations at TRISP. A Helium gas pressure cell has been designed by the sample environment group at the FRM II and tested at TRISP.

6.2 Experimental methods

6.2.1 Crystal and magnetic structures of $TlCuCl_3$

$TlCuCl_3$ belongs to the $KClCu_3$ structure group with the monoclinic space group $P2_1/c$ at room temperature [144]. There is no structural change reported down to $T = 1.5$ K. At $T = 2$ K, the lattice parameters are $a = 3.9625(1)$ Å, $b = 13.7096(2)$ Å, and $c = 8.6594(2)$ Å with $\beta = 95.150(2)^\circ$, determined by neutron powder diffraction [145]. Fig. 6.2 (a) shows a schematic view of unit cell in $TlCuCl_3$ at room temperature, with projection along a axis in the b-c plane. Planar dimers of Cu_2Cl_6 with double chains of $S = 1/2$ Cu^{2+} ions are at the four corners and at the center of the b-c plane. These planar dimers, separated by Tl^+ cations, form a ladder-like structure along the a axis.

The pressure-induced antiferromagnetic order was found in $TlCuCl_3$ by Oosawa *et al.* [146], pointing out that the magnetic moments lie in the b-c plane. At the pressure $p = 14.8$ kbar, they found an additional spin reorientation at $T = 10$ K, leading to an inclination of $\boldsymbol{M}_s$ towards the b axis. In the range $p_c < p < 10$ kbar, the spin structure of $TlCuCl_3$ is depicted in Fig. 6.2 (b). As for the critical spin fluctuations, the components parallel to $\boldsymbol{M}_s$ are defined as the longitudinal (L) fluctuations and the other two

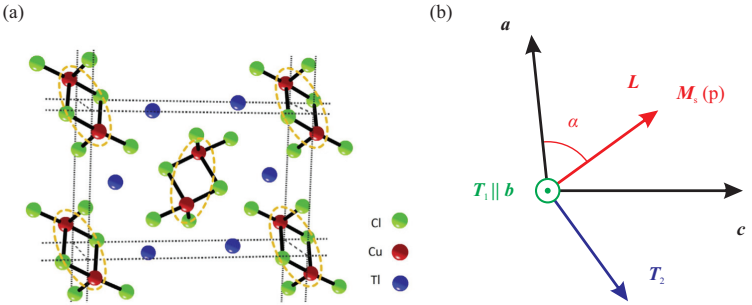

Fig. 6.2: (a) Crystal structure of $TlCuCl_3$ in the crystallographic *b*-*c* plane. The Cu-Cu spin dimers are marked as the yellow dashed ellipses. From [143]. (b) The spin structure of $TlCuCl_3$ at $p_c < p < 10\,\text{kbar}$. The magnetic moments $\boldsymbol{M}_s$ are aligned in the *a*-*c* plane with an angle $\alpha \sim 60\,^\circ$ with respect to *a* axis.

transverse components perpendicular to $\boldsymbol{M}_s$ are denoted as T_1 and T_2, respectively.

6.2.2 Neutron Larmor diffraction

The neutron Larmor diffraction technique, introduced by Rekveldt *et al.* [147], allows to measure the lattice spacing spread $\Delta d/d$ and the mosaicity of a single crystal. In the following we only concentrate on the measurement of $\Delta d/d$, while the measurement of mosaicity can be found elsewhere [148]. The basic idea is that the spin-echo field boundaries (C1-C4) are aligned parallel to the lattice planes of the sample and that the magnetic field configuration of both spin-echo regions is set to be parallel (↑↑). The latter is in contrast to the ordinary spin-echo setup [see Sec. 3.2]. This experimental setup is sensitive to Δd but insensitive to sample mosaicity and independent of beam divergence and monochromaticity. At TRISP, it allows to measure $\Delta d/d$ with a resolution $\Delta d/d \sim 10^{-6}$.

As explained in [147], the Larmor phase difference $\Delta\phi$ is proportional to the relative variation of the reciprocal lattice vector $\Delta\boldsymbol{G}$, which reads

$$\Delta\phi = \phi_{\text{tot}} \frac{\Delta G}{G} \quad \text{with} \quad G = \frac{2\pi}{d}. \tag{6.1}$$

ϕ_{tot} is the total Larmor phase angle arising from ↑↑ magnetic field configuration. Considering the Bragg law, $|\boldsymbol{G}| = 2k_i \sin\theta_B$, and the neutron velocity $v = \hbar k_i/m_n$, the total

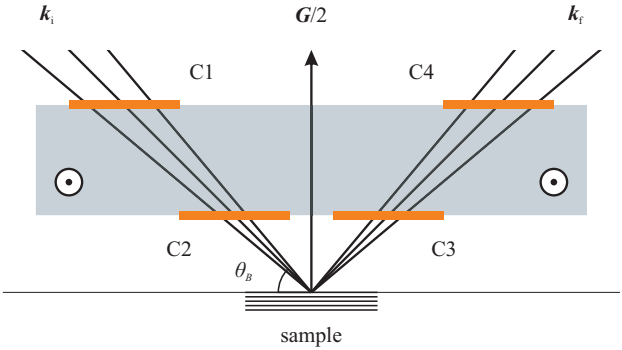

Fig. 6.3: A schematic view of the Larmor diffraction. The coil boundaries of the first (C1, C2) and second (C3, C4) spin-echo arms are parallel to the diffracting planes of the sample. The magnetic field configuration is parallel.

Larmor phase at the exit of the spectrometer can be expressed by

$$\phi_{\mathrm{tot}} = \omega_L \cdot 2L/v = \frac{2\omega_L Lm \sin\theta_{\mathrm{B}}}{\pi\hbar}\, d. \tag{6.2}$$

where ω_L is the same as the one used in *NRSE* mode at TRISP and defined previously in Sec. 3.3.

In general, a single-Gaussian distribution $f(\epsilon)$ with ($\epsilon = \Delta G/G = \Delta\phi/\phi_{\mathrm{tot}}$ describes the distribution of lattice spacing well. In a normalized Gaussian distribution with a FWHM ϵ_{FW},

$$f(\epsilon) = \sqrt{\frac{4\,ln\,2}{\pi}}\,\frac{1}{\epsilon_{\mathrm{FW}}}\exp\Big[-4\,ln\,2\,\frac{\epsilon^2}{\epsilon_{\mathrm{FW}}^2}\Big], \tag{6.3}$$

The polarization $\mathrm{P}(\phi_{\mathrm{tot}})$ is

$$\mathrm{P}(\phi_{\mathrm{tot}}) = \langle\cos\Big[\Delta\phi(\phi_{\mathrm{t}})\Big]\rangle = \int f(\epsilon)\cos\Big[\Delta\phi(\epsilon)\Big]d\epsilon \tag{6.4}$$

$$= \mathrm{P}_0\exp\Big(-\frac{\phi_{\mathrm{t}}^2}{16\,ln\,2}\epsilon_{\mathrm{FW}}^2\Big). \tag{6.5}$$

P_0 is a normalized constant that accounts for the non-perfect initial polarization.

However, in some cases the distribution of lattice spacing is more complicated. For example, if the peak splits as a consequence of a structural transition, such as in iron

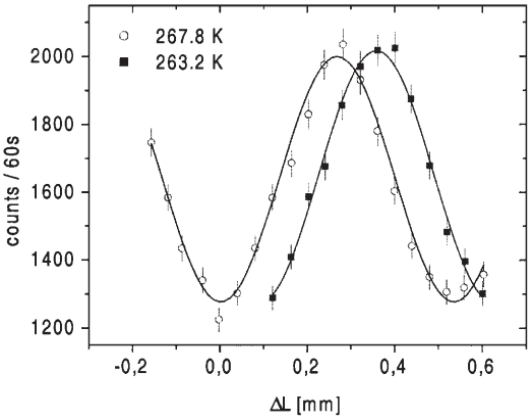

Fig. 6.4: An example of Lamor phase shift due to heating a polycrystalline Al sample. ΔL is the length of the second precession coil from its center. From [147].

pnictides [149]. To fit the data, we consider a multiple-Gaussian distribution $f(\epsilon)$, with the relatively integrated intensity w of the individual peaks.

$$\mathrm{P}(\phi_{\mathrm{tot}}) = \mathrm{P}_0 \sum w_i \exp\Big(- \frac{\phi_{\mathrm{t}}^2}{16\,ln\,2} \epsilon_{\mathrm{FW}}^2 \Big), \tag{6.6}$$

where

$$\sum w_i = 1. \tag{6.7}$$

Another key application of the Larmor diffraction technique is the so-called thermal expansion measurement [147]. This can be performed by measuring the Larmor phase shifts $\Delta\phi$ of the total Larmor phase ϕ_{tot} for a given ω_L while temperature changes. $\Delta\phi$ is measured by scanning the position of the last RF coil. Typically, we choose the Larmor phase at the lowest temperature as the reference point to obtain the Larmor phase shift and the corresponding $\Delta G/G$ [see Eq. (6.1)]. Fig. 6.4 shows $\Delta\phi$ observed in a polycrystalline Al sample due to heating from 263.2 K to 267.8 K, which corresponds to a shift in the lattice spacing $\Delta G/G$ [147].

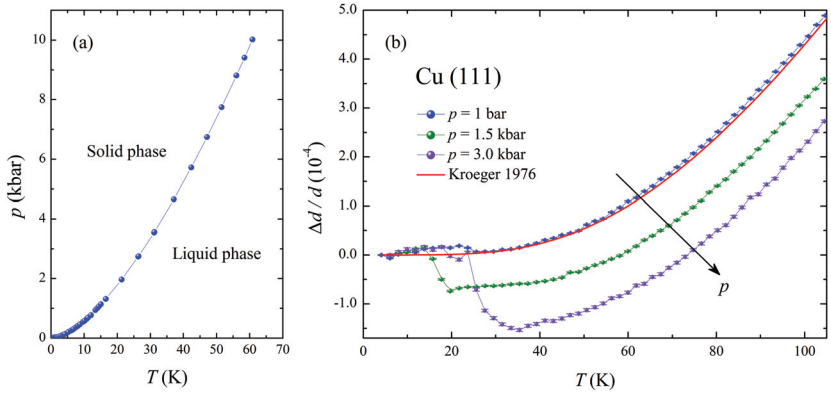

Fig. 6.5: (a) p-T phase diagram of He. Replotted from [150, 151, 152]. (b) Thermal expansion studies on the Cu (111) at various pressures, ranging from ambient to $p = 3.0$ kbar. Previous work by Kroeger [153] is also included for comparison. The sudden drops of $\Delta d/d$ under pressure result from the solid-liquid phase transition of He.

6.2.3 A Helium gas pressure cell

Usually, CuBe is used for pressure cells in neutron spectroscopy. The disadvantage of this material is the relatively high absorption rate of neutrons. Aluminum is nearly transparent for neutrons, but has a lower tensile strength than CuBe, such that aluminum cells with inner cell diameters of 6 mm are limited to pressures up to 7 kbar, whereas more than 20 kbar are reached with CuBe cells. As the critical pressure for $TlCuCl_3$ is well in the range of the aluminum cell, we decided to take advantage of this nearly transparent material. A more detailed description concerning the high-pressure neutron scattering techniques can be found in [154]. At the FRM II, a helium (He) gas pressure cell made of high-tensile aluminum alloy 7075 has been designed by the sample environment group. With an inner diameter of 10 mm, the pressure cell uses compressed He gas as the pressure medium, which allows to apply pressure up to $p = 4$ bar.

For the usage of a He gas pressure cell, one should consider the pressure-temperature (p-T) phase diagram of He [150, 151, 152], as shown in Fig. 6.5 (a). The boundary line represents the melting curve of He in the (p, T) space and thus separates the solid and liquid phases. Practically, we apply the pressure at a temperature above 40 K, where He is still in the gas state. Once the pressure is stable, we then cool down the system to the lowest temperature. At this stage, the applied pressure is not stable since temperature is decreasing until the system passes through the melting point of He. This means that if we want to change the pressure the whole system should be warmed up to the tem-

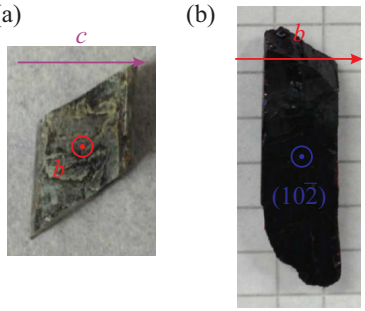

Fig. 6.6: Photograghs of (a) Sample I and (b) Sample II. In the high-pressure neutron experiments, Sample I was mounted in the (0KL) scattering plane. Sample II was firstly mounted in the scattering plane spanned by (010) and (10$\bar{2}$) planes.

perature well above the melting temperature associated with the initial applied pressure [see Fig. 6.5 (a)].

To test the pressure cell, we performed thermal expansion measurements on a Cu (111) crystal using the Larmor diffraction technique. Fig. 6.5 (b) shows these experimental results at ambient, p = 1.5 and 3.0 kbar. At ambient, our result agrees with Kroeger's work on the thermal expansion work of Cu [153], except that a small bump was found in the low temperature region. This anomaly is due to the magnetic contribution of a steel component used in the pressure cell. At p = 1.5 and 3.0 kbar, two sudden drops are found at the temperatures corresponding to the He melting temperatures, which are used to determine the actual pressure acting on the sample.

By using Larmor diffraction, we can estimate the pressure lost of the pressure cell while temperature passing through the melting point. Recalling from the bulk modulus B of a material, its relation associated with pressure p and volume V is given by

$$\Delta p = -B\frac{\Delta V}{V} \quad \text{with} \quad \frac{\Delta V}{V} \approx 3\frac{\Delta d}{d}. \tag{6.8}$$

Taking $B = 1.42 \times 10^{11}\,\mathrm{N}/m^2$ for Cu at low temperature [155] and the drop amplitudes of $\Delta d/d$ above and below the melting point, the pressure losses are 0.38 and 0.74 kar for p = 1.5 and 3.0 kbar, respectively. This fact offers an important information of the usage of He gas pressure cell during the experiments.

6.3 Results and discussion

In our studies of critical fluctuations through the QPT of $TlCuCl_3$, we used two single crystals: Sample I was provided by Prof. Ch. Rüegg at the Paul Scherrer Institute (PSI), Switzerland; Sample II was grown by Dr. C. T. Lin from the crystal growth

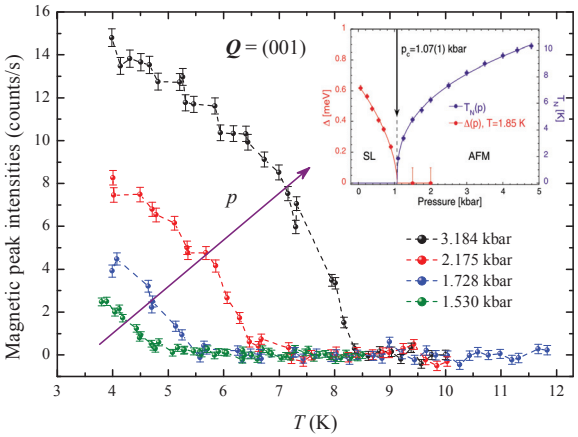

Fig. 6.7: Intensities of the antiferromagnetic Bragg peak at $\boldsymbol{Q} = (001)$ in $TlCuCl_3$ under various pressures. The inset shows the $T_N(p)$ and energy gap Δ as a function of pressure with $p_c = 1.07$ kbar. From [140].

group at the Max Planck Institute for Solid State Research (MPI-FKF), Germany. Both crystals were synthesized by the Bridgeman method. The $TlCuCl_3$ single crystals are shiny black and their surfaces can turn greenish if in the humid environment, with H_2O plus Cl probably forming HCl. They are soft and can easily be cut along the $[010]$ and $[10\bar{2}]$ directions with a razor blade and application of some small force. Fig. 6.6 (a) and (b) show the photographs of Sample I and II used in our investigations. The Sample I has already turn greenish and is degrading. The fresh Sample II shows a shiny surfaces corresponding to the natural cleavage planes.

6.3.1 Sample I

Sample I was available from previous high-pressure neutron scattering experiments by Rüegg *et al.* [140, 141]. The crystal was aligned and mounted in the pressure cell in the $(0KL)$ scattering plane. We performed a series of temperature scan on the intensity of the (001) Bragg peak of $TlCuCl_3$ to check of the pressure-induced antiferromagnetic order at different pressures larger than the critical pressure $p_c = 1.07$ kbar, as shown in Fig. 6.7. The wave vector $\boldsymbol{Q} = (001)$ is expected to be a pure antiferromagnetic Bragg peak. Note that relatively large background with ~ 5 counts/s was observed due to the degradation of Sample I. These background contributions were cut out from our data. T_N is enhanced while increasing applied pressure, in good agreement with the work from [140]. Experimentally, the relation between T_N [K] and p [kbar] follows a simple

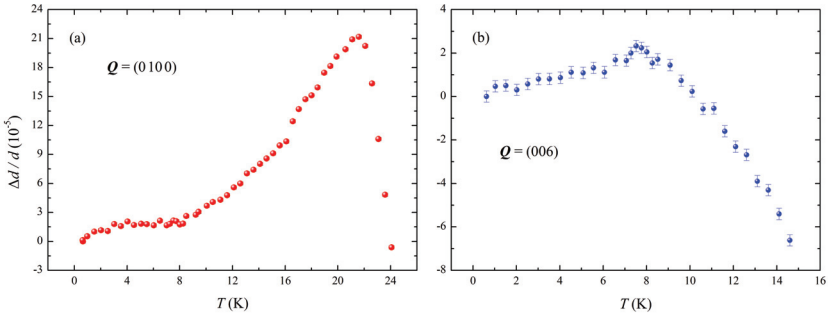

Fig. 6.8: Thermal expansion studies on the nuclear Bragg reflections at (a) $\boldsymbol{Q} = (0\,1\,0\,0)$ and (b) $\boldsymbol{Q} = (006)$. A sudden drop of (a) allows to determine the actual pressure applied to the sample.

power law [145],

$$T_{\mathrm{N}} = 6.348\,(p - 1.07)^{0.37}. \tag{6.9}$$

Accordingly, we tried to measure the linewidths of critical spin fluctuations below and above $T_{\mathrm{N}}(p)$ at $p > p_c$, using the NRSE technique at TRISP. However, we were not able to extract the linewidths from these experiments, for that the observed background (~ 5 counts/s) largely obscures the spin-echo signal.

We then turned to perform the thermal expansion experiments under pressure $p = 2$ kbar $> p_c$. Fig. 6.8 shows the $\Delta d/d$ data of nuclear Bragg peaks at (a) $\boldsymbol{Q} = (0\,1\,0\,0)$ and (b) $\boldsymbol{Q} = (006)$. In (a), a sudden drop appears in the $\boldsymbol{Q} = (0\,1\,0\,0)$ data at around 21 K, which corresponds to the melting point of He. The applied pressure 1.99 kbar can be derived from the solid-liquid phase diagram. Anomalies are found below T_{N} in both reflections, which may arise from the diverging Grüneisen parameter $\Gamma = \alpha/c_p$ in the quantum critical scaling region [156], where the thermal expansion α is more singular than the specific heat c_p. In the literature, there are several examples exhibiting a divergent Grüneisen parameter in the quantum criticality, such as heavy fermion metals $Pr_2Ir_2O_7$ [157] and $YbRh_2Si_2$ [158].

6.3.2 Sample II

The fresh Sample II crystal was mounted in a sealed Al can with a transparent window made of a Kapton film, preventing a H_2O contact with the crystal. We used an in-house X-ray Laue camera to probe the surface properties along $[010]$ and $[10\bar{2}]$ directions, as shown in Fig. 6.9. They are in good agreement with the expected patterns from Laue pattern simulations, whereas Fig. 6.9 (b) shows that the crystal is slightly misaligned along the $[10\bar{2}]$ direction. We then performed the single-crystal neutron diffraction of Sample II at the diffractometer RESI, FRM II in order to have a full knowledge of the crystal's orientation and quality. The obtained lattice parameters agree with the values in the literature [145]. Fig 6.9 (c) and (d) depict some selected diffraction patterns. The observed strong nuclear Bragg reflections confirm the crystal to be single domain. In addition, the FWHM angle from the rocking curve of the crystal is $\sim 0.3\,^{\circ}$, within the instrument resolution.

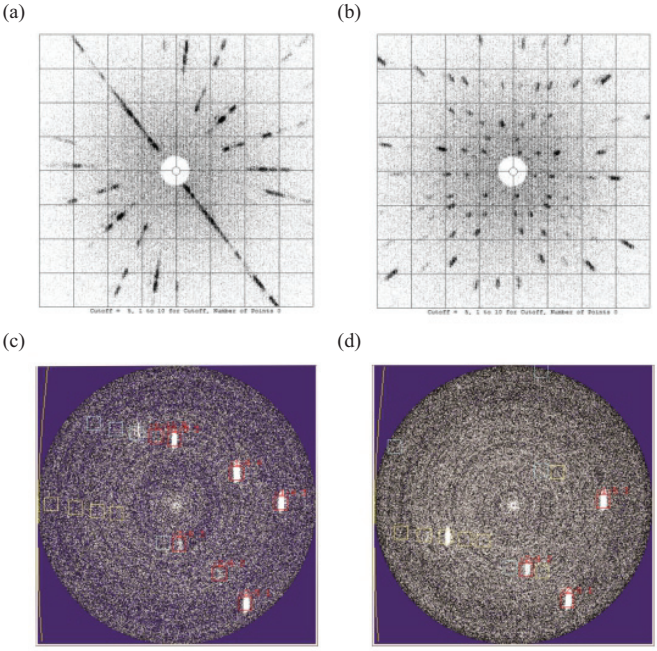

Fig. 6.9: (a,b) X-ray Laue and (c,d) neutron diffraction patterns of Sample II. The results in (a) and (b) were measured in backscattering configuration along the $[010]$ and $[10\bar{2}]$ directions. In (c,d), strong nuclear Bragg points were observed.

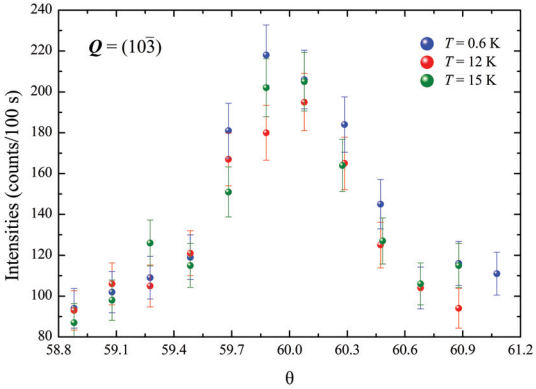

Fig. 6.10: A rocking scan of $\boldsymbol{Q} = (10\bar{3})$ at $p = 1.74$ kbar at $T = 0.6$, 12, and 15 K. No magnetic signals are observed.

Moving Sample II to the pressure cell, we firstly mounted the crystal in the scattering plane spanned by (010) and $(10\bar{2})$ reflections and checked the alignment. Secondly, we took the (010) reflection as a reference and then adjusted to new scattering plane spanned by the (010) and a purely magnetic reflection at $(10\bar{3})$. Since magnetic order in the $(10\bar{3})$ reflection only appears under extreme conditions, several in-plane nuclear Bragg peaks, such as at (040), $(14\bar{3})$ and $(15\bar{3})$, were checked at room temperature. This confirms the alignment of Sample II. At $p = 1.74$ kbar $> p_c$ and $T = 0.6$ K, unfortunately, there were no any pressure-induced magnetic signals that can be detected at $\boldsymbol{Q} = (10\bar{3})$. Fig. 6.10 shows a rocking scan of $\boldsymbol{Q} = (10\bar{3})$ at $p = 1.74$ kbar at different temperatures. A weak and temperature independent peak was observed, possibly due to the second order contamination of the nuclear Bragg peak $(20\bar{6})$.

6.4 Summary

In current studies on the single crystals of $TlCuCl_3$, we are incapable to obtain a conclusive result. Only Sample I shows pressure-induced magnetic order at $p > p_c = 1.07$ kbar, however, the existence of larger background (~ 5 counts/s), arising from the crystal degradation, makes the spin-echo signals difficult to obtain. Anomalies in $\Delta d/d$ are found from the thermal expansion experiments. This might be explained by the universally divergent property of the Grüneisen ratio in the quantum criticality region. However, we can't offer more evidences to support this argument so far.

From the technical aspects, we have tested the He gas pressure cell designed by the sample environment group at the FRM II. It proves that the pressure cell is reliable within its working temperature and pressure range, where a previous He gas leakage problem were reported. The pressure loss in the cell resulting from the He passing across the soild-liquid phase boundary can be estimated. This property is crucial for further applications in the future.

Bibliography

[1] Andrews, T. The Bakerian lecture: On the continuity of the gaseous and liquid states of matter. *Phil. Trans. R. Soc. Lond.* **159**, 575 (1869).

[2] Als-Nielsen, J. *Neutron scattering and spatial correlation near the critical point*, vol. 5a of *Phase transitions and critical phenomena* (Academic Press, 1976).

[3] Collins, M. F. *Magnetic critical scattering* (Oxford University Press, 1989).

[4] Levelt-Sengers, J. M. H. From van der waals' equation to the scaling laws. *Physica* **73**, 73 (1974).

[5] Hohenemser, C., Rosov, N. & Kleinhammes, A. Critical phenomena studied via nuclear techniques. *Hyperfine Interactions* **49**, 267 (1989).

[6] Halperin, B. I. & Hohenberg, P. C. Scaling laws for dynamic critical phenomena. *Phys. Rev.* **177**, 952 (1969).

[7] Hohenberg, P. C. & Halperin, B. I. Theory of dynamic critical phenomena. *Rev. Mod. Phys.* **49**, 435 (1977).

[8] Christianson, R. J., Leheny, R. L., Birgeneau, R. J. & Erwin, R. W. Critical dynamics of a spin-5/2 two-dimensional isotropic antiferromagnet. *Phys. Rev. B* **63**, 140401 (2001).

[9] Tseng, K. F., Keller, T., Walters, A. C., Birgeneau, R. J. & Keimer, B. Neutron spin-echo study of the critical dynamics of spin-5/2 antiferromagnets in two and three dimensions. *Phys. Rev. B* **94**, 014424 (2016).

[10] Riedel, E. & Wegner, F. Dynamic scaling theory for anisotropic magnetic systems. *Phys. Rev. Lett.* **24**, 730 (1970).

[11] Riedel, E. & Wegner, F. Crossover effects in dynamic critical phenomena in MnF_2 and FeF_2. *Phys. Lett. A* **32**, 273 (1970).

[12] Pfeuty, P., Jasnow, D. & Fisher, M. E. Crossover scaling functions for exchange anisotropy. *Phys. Rev. B* **10**, 2088 (1974).

[13] Schulhof, M. P., Nathans, R., Heller, P. & Linz, A. Inelastic neutron scattering from MnF_2 in the critical region. *Phys. Rev. B* **4**, 2254 (1971).

[14] Dietrich, O. W. Critical magnetic fluctuations in MnF_2. *J. Phys. C: Solid State Phys.* **2**, 2022 (1969).

[15] Frey, E. & Schwabl, F. Critical dynamics of magnets. *Advances in Physics* **43**, 577 (1994).

[16] Tsai, S.-H. & Landau, D. P. Critical dynamics of the simple-cubic Heisenberg antiferromagnet $RbMnF_3$: Extrapolation to $q = 0$. *Phys. Rev. B* **67**, 104411 (2003).

[17] Lee, Y. S., Greven, M., Wells, B. O., Birgeneau, R. J. & Shirane, G. Spin correlations in the two-dimensional spin-5/2 Heisenberg antiferromagnet. *Eur. Phys. J. B* **5**, 15 (1998).

[18] Mazenko, G. F. & Valls, O. T. Dynamic critical exponent z in some two-dimensional models. *Phys. Rev. B* **24**, 1419 (1981).

[19] Birgeneau, R. J., Guggenheim, H. J. & Shirane, G. Neutron scattering investigation of phase transitions and magnetic correlations in the two-dimensional antiferromagnets K_2NiF_4, Rb_2MnF_4, Rb_2FeF_4. *Phys. Rev. B* **1**, 2211 (1970).

[20] Onsager, L. Crystal statistics. I. A two-dimensional model with an order-disorder transition. *Phys. Rev.* **65**, 117 (1944).

[21] Squires, G. L. The scattering of slow neutrons by ferromagnetic crystals. *Proc. Phys. Soc. London, Sect. A* **67**, 248 (1954).

[22] Latham, R. & Cassels, J. M. The inelastic scattering of very slow neutrons by iron. *Proc. Phys. Soc. London, Sect. A* **65**, 241 (1952).

[23] Als-Nielsen, J. & Dietrich, O. W. Pair-correlation function in disordered β-brass as studied by neutron diffraction. *Phys. Rev.* **153**, 706 (1967).

[24] Dietrich, O. W. & Als-Nielsen, J. Temperature dependence of short-range order in β-brass. *Phys. Rev.* **153**, 711 (1967).

[25] Als-Nielsen, J. & Dietrich, O. W. Long-range order and critical scattering of neutrons below the transition temperature in β-brass. *Phys. Rev.* **153**, 717 (1967).

[26] Stanley, H. E. *Introduction to phase transitions and critical phenomena* (Oxford University Press, 1987).

[27] Hohenemser, C., Chow, L. & Suter, R. M. Dynamical critical behavior of isotropic ferromagnets. *Phys. Rev. B* **26**, 5056 (1982).

[28] Tucciarone, A., Lau, H. Y., Corliss, L. M., Delapalme, A. & Hastings, J. M. Quantitative analysis of inelastic scattering in two-crystal and three-crystal neutron spectrometry; critical scattering from $RbMnF_3$. *Phys. Rev. B* **4**, 3206 (1971).

[29] Coldea, R., Cowley, R. A., Perring, T. G., McMorrow, D. F. & Roessli, B. Critical behavior of the three-dimensional Heisenberg antiferromagnet $RbMnF_3$. *Phys. Rev. B* **57**, 5281 (1998).

[30] Heller, P. Nuclear resonance studies of magnetic critical fluctuations in MnF_2. *Natl. Bur. Standards Publication* **273**, 58 (1966).

[31] de Renzi, R. *et al.* Magnetic properties of MnF_2 and CoF_2 determined by implanted positive muons. II. Sublattice magnetization and phase transition. *Phys. Rev. B* **30**, 197 (1984).

[32] Bucci, C. & Guidi, G. Critical behaviour of a two-dimensional antiferromagnet : Nuclear magnetic resonance measurements. *J. Phys. Colloques* **32**, C1–887 (1971).

[33] Bucci, C. & Guidi, G. Magnetic phase transition in planar antiferromagnets: ^{19}F magnetic-resonance experiments in K_2MnF_4. *Phys. Rev. B* **9**, 3053 (1974).

[34] Van Hove, L. Correlations in space and time and Born approximation scattering in systems of interacting particles. *Phys. Rev.* **95**, 249 (1954).

[35] Keimer, B. *et al.* Magnetic excitations in pure, lightly doped, and weakly metallic La_2CuO_4. *Phys. Rev. B* **46**, 14034 (1992).

[36] Greven, M. *et al.* Spin correlations in the 2D Heisenberg antiferromagnet $Sr_2CuO_2Cl_2$: Neutron scattering, Monte Carlo simulation, and theory. *Phys. Rev. Lett.* **72**, 1096 (1994).

[37] Greven, M. *et al.* Neutron scattering study of the two-dimensional spin $S = 1/2$ square-lattice Heisenberg antiferromagnet $Sr_2CuO_2Cl_2$. *Z. Phys. B* **96**, 465 (1995).

[38] Birgeneau, R. J. Spin correlations in the two-dimensional $S = 1$ Heisenberg antiferromagnet. *Phys. Rev. B* **41**, 2514 (1990).

[39] Nakajima, K. *et al.* Spin dynamics and spin correlations in the spin $S = 1$ two-dimensional square-lattice Heisenberg antiferromagnet La_2NiO_4. *Z. Phys. B* **96**, 479 (1995).

[40] Kim, Y. J., Birgeneau, R. J., Chou, F. C., Erwin, R. W. & Kastner, M. A. Critical spin dynamics of the 2D quantum Heisenberg antiferromagnets $Sr_2CuO_2Cl_2$ and $Sr_2Cu_3O_4Cl_2$. *Phys. Rev. Lett.* **86**, 3144 (2001).

[41] Leheny, R. L., Christianson, R. J., Birgeneau, R. J. & Erwin, R. W. Spin correlations in an isotropic spin-$5/2$ two-dimensional antiferromagnet. *Phys. Rev. Lett.* **82**, 418 (1999).

[42] Cuccoli, A., Tognetti, V., Vaia, R. & Verrucchi, P. Temperature and spin dependent correlation length of the quantum Heisenberg antiferromagnet on the square lattice. *Phys. Rev. Lett.* **77**, 3439 (1996).

[43] Cuccoli, A., Tognetti, V., Vaia, R. & Verrucchi, P. Two-dimensional quantum Heisenberg antiferromagnet: Effective-Hamiltonian approach to the thermodynamics. *Phys. Rev. B* **56**, 14456 (1997).

[44] Chakravarty, S., Halperin, B. I. & Nelson, D. R. Low-temperature behavior of two-dimensional quantum antiferromagnets. *Phys. Rev. Lett.* **60**, 1057 (1988).

[45] Chakravarty, S., Halperin, B. I. & Nelson, D. R. Two-dimensional quantum Heisenberg antiferromagnet at low temperatures. *Phys. Rev. B* **39**, 2344 (1989).

[46] Hasenfratz, P. & Niedermayer, F. The exact correlation length of the antiferromagnetic $d = 2 + 1$ Heisenberg model at low temperatures. *Phys. Lett. B* **268**, 231 (1991).

[47] Mezei, F. Role of spin-nonconserving forces in the critical dynamics of Fe at the Curie point. *Phys. Rev. Lett.* **49**, 1096 (1982).

[48] Mezei, F. Critical dynamics in isotropic ferromagnets. *J. Mag. Mag. Mat.* **45**, 67 (1984).

[49] Mezei, F. *Neutron spin echo*, vol. 179 of *Lecture notes in physics* (Springer-Verlag, 1980).

[50] Golub, R. & Gähler, R. A neutron resonance spin echo spectrometer for quasielastic and inelastic scattering. *Phys. Lett. A* **123**, 43 (1987).

[51] Gähler, R. & Golub, R. Neutron resonance spin echo, bootstrap method for increasing the effective magnetic field. *J. Phys. France* **49**, 1195 (1988).

[52] Sachdev, S. & Keimer, B. Quantum criticality. *Physics Today* **64**, 29 (2011).

[53] Pelissetto, A. & Vicari, E. Critical phenomena and renormalization-group theory. *Phys. Rep.* **368**, 549 (2002).

[54] Campostrini, M., Hasenbusch, M., Pelissetto, A., Rossi, P. & Vicari, E. Critical exponents and equation of state of the three-dimensional Heisenberg universality class. *Phys. Rev. B* **65**, 144520 (2002).

[55] Wilson, K. G. Renormalization group and critical phenomena. I. Renormalization group and the Kadanoff scaling picture. *Phys. Rev. B* **4**, 3174 (1971).

[56] Wilson, K. G. & Kogut, J. The renormalization group and the ϵ expansion. *Phys. Rep.* **12**, 75 (1974).

[57] Kadanoff, L. P. *et al.* Static phenomena near critical points: Theory and experiment. *Rev. Mod. Phys.* **39**, 395 (1967).

[58] Fisher, M. E. Correlation functions and the critical region of simple fluids. *J. Math. Phys.* **5**, 944 (1964).

[59] Ornstein, L. S. & Zernike, F. The linear dimension of density variations. *Z. Phys.* **19**, 134 (1918).

[60] Ahlers, G. & Kornblit, A. Universality of the specific heat of Heisenberg magnets near the critical temperature. *Phys. Rev. B* **12**, 1938 (1975).

[61] Reno, R. C. & Hohenemser, C. Perturbed angular correlation measurement on ^{100}Rh in a Ni host: Critical exponent β for Ni. *Phys. Rev. Lett.* **25**, 1007 (1970).

[62] Kachnowski, T. A., Suter, R. M., Gottlieb, A. M. & Hohenemser, C. Critical exponent γ for Ni, as measured by perturbed angular correlations in Ni^{100}Rh. *Phys. Rev. B* **14**, 5022 (1976).

[63] Kobeissi, M. A. Mössbauer study of static and dynamic critical behavior in Fe. *Phys. Rev. B* **24**, 2380 (1981).

[64] Arrott, A. S., Heinrich, B. & Noakes, J. E. The role of dipole-dipole interactions in the critical behavior of ferromagnetic materials. *AIP Conf. Proc.* **10**, 822 (1973).

[65] Salamon, M. B. Dipolar-dominated critical behavior of EuO. *Solid State Communications* **13**, 1741 (1973).

[66] Huang, C.-C. & Ho, J. T. Faraday rotation near the Curie point of EuO. *Phys. Rev. B* **12**, 5255 (1975).

[67] Belanger, D. *et al.* Critical behavior in anisotropic antiferromagnets. *J. Magn. Magn. Mat.* **31**, 1095 (1983).

[68] Kulpa, S. M. Precision measurements of the F^{19} NMR in FeF_2 from 4.2°K to the critical region. *J. Appl. Phys.* **40**, 2274 (1969).

[69] Belanger, D. P. & Yoshizawa, H. Neutron scattering and the critical behavior of the three-dimensional Ising antiferromagnet FeF_2. *Phys. Rev. B* **35**, 4823 (1987).

[70] Bucci, C., Guidi, G. & Vignali, C. Two-dimensional antiferromagnets: Rb^{87} NMR in Rb_2CoF_4. *Solid State Communications* **10**, 803 (1972).

[71] Hutchings, M. T., Ikeda, H. & Janke, E. Dynamic critical neutron scattering from a two-dimensional Ising system Rb_2CoF_4. *Phys. Rev. Lett.* **49**, 386 (1982).

[72] Minkiewicz, V. J., Collins, M. F., Nathans, R. & Shirane, G. Critical and spin-wave fluctuations in nickel by neutron scattering. *Phys. Rev.* **182**, 624 (1969).

[73] Minkiewicz, V. J. Critical and spin-wave fluctuations in ferromagnets by neutron scattering. *Int. J. Magn.* **1**, 149 (1971).

[74] Dietrich, O. W., Als-Nielsen, J. & Passell, L. Neutron scattering from the Heisenberg ferromagnets EuO and EuS. III. Spin dynamics of EuO. *Phys. Rev. B* **14**, 4923 (1976).

[75] Chow, L., Hohenemser, C. & Suter, R. M. Observation of crossover in the dynamic exponent z in Fe and Ni. *Phys. Rev. Lett.* **45**, 908 (1980).

[76] Mezei, F. Neutron scattering critical dynamics in EuO at the ferromagnetic Curie point. *Physica B* **136**, 417 (1986).

[77] Dunlap, R. A. & Gottlieb, A. M. Critical spin fluctuations in EuO. *Phys. Rev. B* **22**, 3422 (1980).

[78] Böni, P. & Shirane, G. Paramagnetic neutron scattering from the Heisenberg ferromagnet EuO. *Phys. Rev. B* **33**, 3012 (1986).

[79] Böni, P., Chen, M. E. & Shirane, G. Comparison of the critical magnetic scattering from the Heisenberg system Euo with renormalization-group theory. *Phys. Rev. B* **35**, 8449 (1987).

[80] Frey, E. & Schwabl, F. Critical dynamics of dipolar ferromagnets. *Phys. Lett. A* **123**, 49 (1987).

[81] Kötzler, J. Dipolar interactions in the critical dynamics of Heisenberg ferromagnets. *Phys. Rev. Lett.* **51**, 833 (1983).

[82] Aharony, A. & Fisher, M. E. Critical behavior of magnets with dipolar interactions. I. Renormalization group near four dimensions. *Phys. Rev. B* **8**, 3323 (1973).

[83] Teaney, D. T., Freiser, M. J. & Stevenson, R. W. H. Discovery of a simple cubic antiferromagnet: Antiferromagnetic resonance in $RbMnF_3$. *Phys. Rev. Lett.* **9**, 212 (1962).

[84] Freiser, M. J., Seiden, P. E. & Teaney, D. T. Field-independent longitudinal antiferromagnetic resonance. *Phys. Rev. Lett.* **10**, 293 (1963).

[85] Gottlieb, A. M. & Heller, P. Nuclear-resonance studies of critical fluctuations in FeF_2 above T_N. *Phys. Rev. B* **3**, 3615 (1971).

[86] Hutchings, M. T., Schulhof, M. P. & Guggenheim, H. J. Critical magnetic neutron scattering from ferrous fluoride. *Phys. Rev. B* **5**, 154 (1972).

[87] Schulhof, M. P., Heller, P., Nathans, R. & Linz, A. Critical magnetic scattering in manganese fluoride. *Phys. Rev. B* **1**, 2304 (1970).

[88] Johnson, F. M. & Nethercot, A. H. Antiferromagnetic resonance in MnF_2. *Phys. Rev.* **114**, 705 (1959).

[89] Ohlmann, R. C. & Tinkham, M. Antiferromagnetic resonance in FeF_2 at far-infrared frequencies. *Phys. Rev.* **123**, 425 (1961).

[90] Ikeda, H. & Hirakawa, K. Neutron scattering study of two-dimensional Ising nature of K_2CoF_4. *Solid State Commun.* **14**, 529 (1974).

[91] Samuelsen, E. J. Experimental study of the two-dimensional Ising antiferromagnet Rb_2CoF_4. *Phys. Rev. Lett.* **31**, 936 (1973).

[92] Slivka, J., Keller, H., Kündig, W. & Wanklyn, B. M. Critical spin fluctuations in the two-dimensional antiferromagnet $KFeF_4$: A Mössbauer study. *Phys. Rev. B* **30**, 3649 (1984).

[93] Bradford, E. & Marshall, W. Mössbauer absorption in the presence of electron spin relaxation. *Proc. Phys. Soc. London* **87**, 731 (1966).

[94] Mermin, N. D. & Wagner, H. Absence of ferromagnetism or antiferromagnetism in one- or two-dimensional isotropic Heisenberg models. *Phys. Rev. Lett.* **17**, 1133 (1966).

[95] Bednorz, J. G. & Müller, K. A. Possible high T_c superconductivity in the Ba-La-Cu-O system. *Z. Phys. Cond. Matt.* **64**, 189 (1986).

[96] Igarashi, J.-i. $1/S$ expansion for thermodynamic quantities in a two-dimensional Heisenberg antiferromagnet at zero temperature. *Phys. Rev. B* **46**, 10763 (1992).

[97] Tyč, S., Halperin, B. I. & Chakravarty, S. Dynamic properties of a two-dimensional Heisenberg antiferromagnet at low temperatures. *Phys. Rev. Lett.* **62**, 835 (1989).

[98] Elstner, N., Sokol, A., Singh, R. R. P., Greven, M. & Birgeneau, R. J. Spin dependence of correlations in two-dimensional square-lattice quantum Heisenberg antiferromagnets. *Phys. Rev. Lett.* **75**, 938 (1995).

[99] Fulton, S., Cowley, R. A., Desert, A. & Mason, T. The static and dynamic critical behaviour of the two-dimensional Heisenberg antiferromagnet $KFeF_4$. *J. Phys.: Condens. Matter* **6**, 6679 (1994).

[100] Cuccoli, A., Tognetti, V., Verrucchi, P. & Vaia, R. Heisenberg antiferromagnet on the square lattice for $S \geq 1$. *Phys. Rev. B* **58**, 14151 (1998).

[101] Cowley, R. A. *et al.* The bicritical phase diagram of two-dimensional antiferromagnets with and without random fields. *Z. Phys. B* **93**, 5 (1993).

[102] Sokol, A., Elstner, N. & Singh, R. R. P. Crossover phase diagram of 2D Heisenberg ferro-and antiferromagnets. arXiv:cond-mat/9505148 (1995).

[103] Dohm, V. & Janssen, H.-K. Dynamic scaling near bicritical points. *Phys. Rev. Lett.* **39**, 946 (1977).

[104] Mezei, F. Neutron spin echo: A new concept in polarized thermal neutron techniques. *Z. Physik* **255**, 146 (1972).

[105] Mezei, F. *Neutron inelastic scattering* (IAEA, Vienna, 1978).

[106] Pynn, R. Neutron spin-echo and three-axis spectrometers. *J. Phys. E* **11**, 1133 (1978).

[107] Keller, T., Golub, R., Mezei, F. & Gähler, R. A neutron resonance spin-echo spectrometer (NRSE) with tiltable fields. *Physica B* **241**, 101 (1997).

[108] Klimko, S. *et al.* Implementation of a zero-field spin-echo option at the three-axis spectrometer IN3 (ILL, Grenoble) and first application for measurements of phonon line widths in superfluid ^{4}He. *Physica B* **335**, 188 (2003).

[109] Habicht, K., Golub, R., Mezei, F., Keimer, B. & Keller, T. Temperature-dependent phonon lifetimes in lead investigated with neutron-resonance spin-echo spectroscopy. *Phys. Rev. B* **69**, 104301 (2004).

[110] Aynajian, P. *Electron-phonon interaction in conventional and unconventional superconductors*. Ph.D. thesis, Universität Stuttgart (2009).

[111] Munnikes, N. *High resolution neutron spectroscopy of excitations in superconductors*. Ph.D. thesis, Universität Stuttgart (2013).

[112] Lovesey, S. W. *Theory of neutron scattering from condensed matter* (Clarendon Press, 1984).

[113] Shirane, G., Shapiro, S. M. & Tranquada, J. M. *Neutron Scattering with a Triple-Axis Spectrometer* (Cambridge University Press, 2002).

[114] Squires, G. L. *Introduction to the Theory of Thermal Neutron Scattering* (Cambridge University Press, 2012).

[115] Keller, T. *et al.* The NRSE-TAS spectrometer at the FRM-2. *Appl. Phys. A* **74**, s332 (2002).

[116] Keller, T. & Keimer, B. Trisp: Three axes spin echo spectrometer. *Journal of large-scale research facilities* **1**, A37 (2016).

[117] Moon, R. M., Riste, T. & Koehler, W. C. Polarization analysis of thermal-neutron scattering. *Phys. Rev.* **181**, 920 (1969).

[118] Habicht, K., Keller, T. & Golub, R. The resolution function in neutron spin-echo spectroscopy with three-axis spectrometers. *J. Appl. Crystallogr.* **36**, 1307 (2003).

[119] Cooper, M. J. & Nathans, R. The resolution function in neutron diffractometry. I. The resolution function of a neutron diffractometer and its application to phonon measurements. *Acta Crystallogr.* **23**, 357 (1967).

[120] James, F. *MINUIT: Function Minimization and Error Analysis, Version 94.1* (CERN Program Library Long Writeup D506, 1994).

[121] Erickson, R. A. Neutron diffraction studies of antiferromagnetism in manganous fluoride and some isomorphous compounds. *Phys. Rev.* **90**, 779 (1953).

[122] Okazaki, A., Turberfield, K. C. & Stevenson, R. W. H. Neutron inelastic scattering measurements of antiferromagnetic excitations in MnF_2 at 4.2 K and at temperatures up to the Neel point. *Phys. Lett.* **8**, 9 (1964).

[123] Keffer, F. Anisotropy in the antiferromagnetic MnF_2. *Phys. Rev.* **87**, 608 (1952).

[124] Birgeneau, R. J., Skalyo, J. & Shirane, G. Critical magnetic scattering in K_2NiF_4. *Phys. Rev. B* **3**, 1736 (1971).

[125] Breed, D. J. Experimental investigation of two two-dimensional antiferromagnets with small anisotropy. *Physica* **37**, 35 (1967).

[126] de Wijn, H. W., Walker, L. R. & Walstedt, R. E. Spin-wave analysis of the quadratic-layer antiferromagnets K_2NiF_4, K_2MnF_4, and Rb_2MnF_4. *Phys. Rev. B* **8**, 285 (1973).

[127] Cowley, R. A., Shirane, G., Birgeneau, R. J. & Guggenheim, H. J. Spin fluctuations in random magnetic-nonmagnetic two-dimensional antiferromagnets. I. Dynamics. *Phys. Rev. B* **15**, 4292 (1977).

[128] Hamer, C. J., Weihong, Z. & Oitmaa, J. Spin-wave stiffness of the Heisenberg antiferromagnet at zero temperature. *Phys. Rev. B* **50**, 6877 (1994).

[129] Bayrakci, S. P. *et al.* Lifetimes of antiferromagnetic magnons in two and three dimensions: Experiment, theory, and numerics. *Phys. Rev. Lett.* **111**, 017204 (2013).

[130] Bruce, A. D. The theory of superlattice critical scattering. *J. Phys. C: Solid State Phys.* **14**, 193 (1981).

[131] Ikeda, H., Tamura, T. & Nakashima, S. Staircases of magnetic structure along the axial direction in the layered magnet Rb_2MnF_4. *J. Phys. C: Solid State Phys.* **20**, L641 (1987).

[132] Popovici, M. On the resolution of slow-neutron spectrometers. IV. The triple-axis spectrometer resolution function, spatial effects included. *Acta Crystallogr.* **31**, 507 (1975).

[133] Habicht, K. SERESCAL version 1.0. , distributed by K. Habicht: habicht@hmi.de (2003). NRSE-TAS resolution matrix calculations based on the SERESCAL code for Matlab by D. A. Tennant and D. McMorrow.

[134] Bloch, F. & Siegert, A. Magnetic resonance for nonrotating fields. *Phys. Rev.* **57**, 522 (1940).

[135] Fischer, T. M., Frey, E. & Schwabl, F. Critical dynamics of isotropic dipolar antiferromagnets. *Physics Lett. A* **146**, 457 (1990).

[136] Wysin, G. M. & Bishop, A. R. Dynamic correlations in a classical two-dimensional Heisenberg antiferromagnet. *Phys. Rev. B* **42**, 810 (1990).

[137] Moriya, T. Nuclear magnetic relaxation near the Curie temperature. *Prog. Theor. Phys.* **28**, 371 (1962).

[138] Vojta, M. Quantum phase transitions. *Rep. Prog. Phys.* **66**, 2069 (2003).

[139] Sachdev, S. *Quantum phase transitions* (Cambridge University Press, 2011).

[140] Rüegg, C. *et al.* Pressure-induced quantum phase transition in the spin-liquid $TlCuCl_3$. *Phys. Rev. Lett.* **93**, 257201 (2004).

[141] Rüegg, C. *et al.* Quantum magnets under pressure: Controlling elementary excitations in $TlCuCl_3$. *Phys. Rev. Lett.* **100**, 205701 (2008).

[142] Merchant, P. *et al.* Quantum and classical criticality in a dimerized quantum antiferromagnet. *Nat. Phys.* **10**, 373 (2014).

[143] Fernandez-Alonso, F. & Price, D. L. *Neutron scattering - magnetic and quantum phenomena*, vol. 48 of *Experimental Methods in the Physical Sciences* (Elsevier, 2015).

[144] Takatsu, K. I., Shiramura, W. & Tanaka, H. Ground states of double spin chain systems $TlCuCl_3$, NH_4CuCl_3 and $KCuBr_3$. *J. Phys. Soc. Jpn.* **66**, 1611 (1997).

[145] Rüegg, C. *Neutron scattering Investigation of quantum phase transitions in the dimer spin systems $TlCuCl_3$ and NH_4CuCl_3*. Ph.D. thesis, Eidgenössischen Technischen Hochschule Zürich (2005).

[146] Oosawa, A. *et al.* Pressure-induced successive magnetic phase transitions in the spin gap system $TlCuCl_3$. *J. Phys. Soc. Jpn.* **73**, 1446 (2004).

[147] Rekveldt, M. T., Keller, T. & Golub, R. Larmor precession, a technique for high-sensitivity neutron diffraction. *Europhys. Lett.* **54**, 342 (2001).

[148] Mezei, F., Pappas, C. & Gutberlet, T. *Neutron spin echo spectroscopy: Basics, trends and applications*, vol. 601 of *Lecture notes in physics* (Springer-Verlag Berlin, 2003).

[149] Lu, X. *et al.* Impact of uniaxial pressure on structural and magnetic phase transitions in electron-doped iron pnictides. *Phys. Rev. B* **93**, 134519 (2016).

[150] Swenson, C. A. The liquid-solid transformation in Helium near absolute zero. *Phys. Rev.* **79**, 626 (1950).

[151] Dugdale, J. S. & Simon, F. E. Thermodynamic properties and melting of solid Helium. *Proc. R. Soc. London, Ser. A* **218**, 291 (1953).

[152] Crawford, R. K. & Daniels, W. B. Experimental determination of the P-T melting curves of Kr, Ne, and He. *J. Chem. Phys.* **55**, 5651 (1971).

[153] Kroeger, F. R. & Swenson, C. A. Absolute linear thermal-expansion measurements on copper and aluminum from 5 to 320 K. *J. Appl. Phys.* **48**, 853 (1977).

[154] Klotz, S. *Techniques in high pressure neutron scattering* (CRC press, 2012).

[155] Ledbetter, H. M. & Naimon, E. R. Elastic properties of metals and alloys. II. Copper. *J. Phys. Chem. Ref. Data* **3**, 897 (1974).

[156] Zhu, L., Garst, M., Rosch, A. & Si, Q. Universally diverging Grüneisen parameter and the magnetocaloric effect close to quantum critical points. *Phys. Rev. Lett.* **91**, 066404 (2003).

[157] Tokiwa, Y., Ishikawa, J. J., Nakatsuji, S. & Gegenwart, P. Quantum criticality in a metallic spin liquid. *Nat. Mater.* **13**, 356 (2014).

[158] Tokiwa, Y., Radu, T., Geibel, C., Steglich, F. & Gegenwart, P. Divergence of the magnetic Grüneisen ratio at the field-induced quantum critical point in $YbRh_2Si_2$. *Phys. Rev. Lett.* **102**, 066401 (2009).

Kuo Feng Tseng
Curriculum Vitae

PERSONAL DETAILS

Birth	March 06, 1985
Nationality	Taiwan
Mail	kuofeng.tseng@gmail.com

EDUCATION

Ph. D. Degree in Physics 03.2012 - 11.2016
Max Planck Institute for Solid State Research, Germany within the International Max Planck Research School for Condensed Matter Science
Critical Dynamics in Classical Antiferromagnets with Prof. Dr. Bernhard Keimer

Military Service 08.2010 - 07.2011
Military Police Center at Tainan, Taiwan

M. Sc. Degree in Physics 09.2007 - 06.2010
National Sun Yat-sen University, Taiwan
Magnetic Field and Pressure Effects on the Spin Frustrated System NaV_2O_4 and Cu_2OSeO_3 with Prof. Dr. Hung-Duen Yang

B. Sc. Degree in Physics 09.2003 - 06.2007
National Chung Hsing University, Taiwan
Semiconductor physics and devices with Prof. Dr. Yuen-Wuu Suen

RESEARCH INTEREST

Unconventional superconductors: cuprates and iron pnictides
Exotic magnetic phenomena: quantum magnets and spin frustrated systems
Instrument development

SKILL AND EXPERIENCE

Neutron resonance spin-echo triple-axis spectroscopy (NRSE-TAS)
Neutron ray-tracing simulation implemented by MATLAB programing
Magnetic and transport measurements under extreme conditions

PUBLICATIONS

1. Neutron spin-echo study of the critical dynamics of spin-5/2 antiferromagnets in two and three dimensions. K. F. Tseng, T. Keller, A. C. Walters, R. J. Birgeneau, and B. Keimer, *Phys. Rev. B* **94**, 014424 (2016)

2. Impact of uniaxial pressure on structural and magnetic phase transitions in electron-doped iron pnictides. Xingye Lu, K. F. Tseng, T. Keller, Wenliang Zhang, Ding Hu, Yu Song, HaoranMan, J. T. Park, Huiqian Luo, Shiliang Li, Andriy H. Nevidomskyy, and Pengchen Dai, *Phys. Rev. B* **93**, 134519 (2016)

3. Magnetic phase diagram of the antiferromagnetic cobalt tellurate Co3TeO6. J. L. Her, C. C. Chou, Y. H. Matsuda, K. Kindo, H. Berger, K. F. Tseng, C. W. Wang, W. H. Li, and H. D. Yang, *Phys. Rev. B* **84**, 235123 (2011)

4. Observation of a second metastable spin-ordered state in ferrimagnet Cu2OSeO3. C. L. Huang, K. F. Tseng, C. C. Chou, S. Mukherjee, J. L. Her, Y. H. Matsuda, K. Kindo, H. Berger, and H. D. Yang, *Phys. Rev. B* **83**, 052402 (2011)

5. Signature of ferroelectricity in magnetically ordered Mo-doped $CoFe_2O_4$. G. D. Dwivedi, K. F. Tseng, C. L. Chan, P. Shahi, J. Lourembam, B. Chatterjee, A. K. Ghosh, H. D. Yang, Sandip Chatterjee, *Phys. Rev. B* **82**, 134428 (2010)

6. Colossal dielectric and magnetodielectric effect in Er_2O_3 nanoparticles embedded in a SiO_2 glass matrix. S. Mukherjee, C. H. Chen, C. C. Chou. K. F. Tseng, B. K. Chaudhuri, and H. D. Yang, *Phys. Rev. B* **82**, 104107 (2010)

7. Low loss high dielectric permittivity of polyvinylidene fluoride and $K_xTi_yNi_{1-x-y}O$ (x = 0.05, y = 0.02) composites. D. Bhadra, A. Biswas. S. Sarkar, B. K. Chaudhuri, K. F. Tseng, and H. D. Yang, *J. Appl. Phys.* **107**, 124115 (2010)

8. Pressure effect on magnetization of quasi-1D double-chain material NaV_2O_4. K. F. Tseng, C. J. Ho, C. C. Chou, C. L. Huang, H. Sakurai, and H. D. Yang, *J. Phys.: Conf. Ser.* **200**, 012211 (2010)

9. Simultaneous presence of ferroelectricity and magnetism in Mn-doped $CoFe_2O_4$. G. D. Dwivedi, K. F. Tseng, C. L. Chan, P. Shahi, B. Chatterjee, A. K. Ghosh, H. D. Yang, Sandip Chatterjee, *AIP Conf. Proc.* **1313**, 162 (2010)

10. Pressure effects on superconductivity and magnetism in $FeSe_{1-x}Te_x$. C. L. Huang, C. C. Chou, K. F. Tseng, Y. L. Huang, F. C. Hsu, K. W. Yeh, M. K. Wu, and H. D. Yang, *J. Phys. Soc. Jpn.* **78**, 084710 (2009)

Acknowledgements

I would like to express my gratitude to Prof. Bernhard Keimer, who gave me the opportunity to perform my research at the Max-Planck-Institut für Festkörperforschung (MPI-FKF) and at the Forschungs-Neutronenquelle Heinz-Maier-Leibnitz (FRM II). I am highly indebted for his persistent support and the time he spent with me for discussions, which were invaluable and highly motivated me.

I am grateful to my day-to-day supervisor, Dr. Thomas Keller, who leads me into the field of neutron resonance spin-echo spectroscopy. With his dedicated surpervision throughout my entire PhD work, I learned the key spirit of neutron spin-echo technique beyond textbooks and the necessary skills in the scientific field. The experimental beam time with him during my PhD is without doubt the most valuable. I am also thankful for all the discussions we made during my writing of this thesis and his great help in proofreading my thesis and translating the Zusammenfassung in German.

I am highly thankful for Prof. Gert Denninger who takes over the Mitberichter duty for my thesis and Prof. Hans Peter Büchler who chairs my PhD committee from the Universität Stuttgart. Thanks also to Dr. Christian Ast, who served as my external PhD committee member at the MPI-FKF.

As for the materials studied in my PhD period, I want to thank Dr. Sibel Bayrakci, Prof. Alan Tennant, and Prof. Robert J. Birgeneau for providing the MnF_2 and Rb_2MnF_4 single crystals, Prof. Christian Rüegg for providing the $TlCuCl_3$ single crystal, Dr. Oliver Stockert for providing the $CeCu_6$ single crystal. I am grateful to the people from the crystal growth group at MPI-FKF, Dr. Zhiwei Li, Dr. Gihun Ryu, and Dr. Chengtian Lin for synthesizing the $TlCuCl_3$ crystal. I also appreciate collaborations with Dr. Xingye Lu and Prof. Pengcheng Dai in studying the pressure effects on iron pnictides $BaFe_{2-x}Ni_xAs_2$, $SrFe_{1.97}Ni_{0.03}As_2$ and $BaFe_2(As_{0.7}P_{0.3})_2$ using TRISP.

I would like to acknowledge the instrumental support at the neutron beam lines. Dr. Bjørn Pedersen and Dr. Zsolt Revay PGAA helped me at the diffractometer RESI and the prompt gamma-ray activation analysis PGAA at the FRM II, respectively. Dr. Marton Marco provides timely assistant during my stay at the diffractometer MORPHEUS, PSI for $TlCuCl_3$ alignment. Without their helps, no neutron scattering experiments would have been successfully gone well.

During my stay at the MPI-FKF, I am thankful for Dr. Andrew Walters with whom I performed experiments at TRISP, FRM II and at the MORPHEUS, PSI. I learned a great deal of experimental tricks and basic knowledge for the neutron spin-echo spectroscopy in the early stage of my PhD. At the FRM II, I am thankful for Dr. Yuri Khaydukov and Dr. Olaf Soltwedel, who are my tea and coffee fellows. Special thanks are addressed to Franz Tralmer and Manfred Ohl, for their technical support.

I am grateful for all the administration help from Dr. Hans-Georg Libuda at the International Max Planck Research School for Condensed Matter Science (IMPRS-CMS), Stuttgart. I really enjoyed all the activities including international workshops, annual retreats, and introductory courses, mainly organized by him and the other PhD fellows. Thanks all of you from the large family of IMPRS-CMS.

I am grateful to all the colleagues in Keimer's department during my stay at MPI-FKF. For experienced scientists, I am thankful for Dr. Mathieu LeTacon, Dr. Dmytro S. Inosov, Dr. B. J. Kim, Dr. Hoyoung Jang, Dr. Yuan Li, Dr. Darren Peets, Dr. Santiago Blanco-Canosa, Dr. Nakheon Sung, Dr. Balint Nafradi, Dr. Jungwha Kim, Dr. Eva Benckiser, Dr. Giniyat Khaliullin, Dr. George Jackeli, and Dr. Alireza Akbari. For PhD/Master student, I want to acknowledge Dr. Gerd Friemel, Dr. Jitae Park, Dr. Michaela Souliou, Dr. Alex Charnukha, Dr. Daniel Pröpper, Dr. Nathalie Munnikes, Dr. Meng Wu, Toshinao Loew, Dr. Friederike Wrobel, Yi Lu, Dr. Timofei Larkin, Juan Pablo Porras, Christopher Dietl, Martin Bluschke, Maximilian Krautloher, Gideok Kim, Matthias Hepting, Hun-ho Kim, Robert Dawson, Jorge Sauceda Flores. I am highly appreciate for Ms. Sonja Balkema's great help in dealing with my administration work.

I am also grateful to all the colleagues at the FRM II, namely Dr. Jitae Park, Dr. Yixi Su, Dr. Zhendong Fu, Dr. Oleg Sobolev, Dr. Markus Hölzel, Dr. Anatoliy Senyshyn, Dr. Christine Kortenbruck, Dr. Ina Lommatzsch. Also, I am highly thankful for the people from the sample environment group, Dr. Jürgen Peters, Heiner Kolb, and Andreas Buchner in developing the He gas pressure cell.

This thesis was supported by the German Science Foundation (DFG) for financial support under Grant No. SFB/TRR 80.

Finally, I want to thank my beloved wife Xiruo Wang, my parents and my younger brother. They encouraged me and gave me confidence to complete this thesis.